The Astrophysical Journal, 985:14 (28pp), 2025 May 20 https://doi.org/10.3847/1538-4357/adbcab

Cloud-scale Gas Properties, Depletion Times, and Star Formation Efficiency per Freefall Time in PHANGS–ALMA

Adam K. Leroy[1,2], Jiayi Sun (孙嘉懿)[3,31], Sharon Meidt[4], Oscar Agertz[5], I-Da Chiang (江宜達)[6], Jindra Gensior[7,8], Simon C. O. Glover[9], Oleg Y. Gnedin[10], Annie Hughes[11], Eva Schinnerer[12], Ashley T. Barnes[13], Frank Bigiel[14], Alberto D. Bolatto[15], Dario Colombo[14], Jakob den Brok[16], Mélanie Chevance[9,17], Ryan Chown[1], Cosima Eibensteiner[18,32], Damian R. Gleis[12], Kathryn Grasha[19,33], Jonathan D. Henshaw[12,20], Ralf S. Klessen[9,16,21,22], Eric W. Koch[16], Elias K. Oakes[23], Hsi-An Pan[24], Miguel Querejeta[25], Erik Rosolowsky[26], Toshiki Saito[27], Karin Sandstrom[28], Sumit K. Sarbadhicary[1,2,29], Yu-Hsuan Teng[15], Antonio Usero[25], Dyas Utomo[1,18], and Thomas G. Williams[30]

[1] Department of Astronomy, The Ohio State University, 140 West 18th Avenue, Columbus, OH 43210, USA; leroy.42@osu.edu
[2] Center for Cosmology and Astroparticle Physics (CCAPP), 191 West Woodruff Avenue, Columbus, OH 43210, USA
[3] Department of Astrophysical Sciences, Princeton University, 4 Ivy Lane, Princeton, NJ 08544, USA
[4] Sterrenkundig Observatorium, Universiteit Gent, Krijgslaan 281 S9, B-9000 Gent, Belgium
[5] Lund Observatory, Division of Astrophysics, Department of Physics, Lund University, Box 43, SE-221 00 Lund, Sweden
[6] Institute of Astronomy and Astrophysics, Academia Sinica, No. 1, Sec. 4, Roosevelt Road, Taipei 106319, Taiwan
[7] Institute for Astronomy, University of Edinburgh, Royal Observatory, Blackford Hill, Edinburgh EH9 3HJ, UK
[8] Department of Astrophysics, University of Zürich, Winterthurerstrasse 190, 8057 Zürich, Switzerland
[9] Universität Heidelberg, Zentrum für Astronomie, Institut für Theoretische Astrophysik, Albert-Ueberle-Str 2, D-69120 Heidelberg, Germany
[10] Department of Astronomy, University of Michigan, Ann Arbor, MI 48109, USA
[11] CNRS, IRAP, 9 Av. du Colonel Roche, BP 44346, F-31028 Toulouse cedex 4, France
[12] Max-Planck-Institut für Astronomie, Königstuhl 17, D-69117, Heidelberg, Germany
[13] European Southern Observatory, Karl-Schwarzschild Straße 2, D-85748 Garching bei München, Germany
[14] Argelander-Institut für Astronomie, Universität Bonn, Auf dem Hügel 71, 53121 Bonn, Germany
[15] Department of Astronomy and Joint Space-Science Institute, University of Maryland, 4296 Stadium Drive, College Park, MD 20742, USA
[16] Center for Astrophysics | Harvard & Smithsonian, 60 Garden Street, Cambridge, MA 02138, USA
[17] Cosmic Origins Of Life (COOL) Research DAO, Germany
[18] National Radio Astronomy Observatory, 520 Edgemont Road, Charlottesville, VA 22903, USA
[19] Research School of Astronomy and Astrophysics, Australian National University, Canberra, ACT 2611, Australia
[20] Astrophysics Research Institute, Liverpool John Moores University, IC2, Liverpool Science Park, 146 Brownlow Hill, Liverpool L3 5RF, UK
[21] Universität Heidelberg, Interdisziplinäres Zentrum für Wissenschaftliches Rechnen, Im Neuenheimer Feld 205, D-69120 Heidelberg, Germany
[22] Radcliffe Institute for Advanced Studies at Harvard University, 10 Garden Street, Cambridge, MA 02138, USA
[23] Department of Physics, University of Connecticut, 196A Auditorium Road, Storrs, CT 06269, USA
[24] Department of Physics, Tamkang University, No.151, Yingzhuan Road, Tamsui Dist., New Taipei City 251301, Taiwan
[25] Observatorio Astronómico Nacional (IGN), C/Alfonso XII, 3, E-28014 Madrid, Spain
[26] Department of Physics, University of Alberta, Edmonton, AB T6G 2E1, Canada
[27] Faculty of Global Interdisciplinary Science and Innovation, Shizuoka University, 836 Ohya, Suruga-ku, Shizuoka 422-8529, Japan
[28] Center for Astrophysics and Space Sciences, Department of Physics, University of California, San Diego, 9500 Gilman Drive, La Jolla, CA 92093, USA
[29] Department of Physics, The Ohio State University, Columbus, Ohio 43210, USA
[30] Sub-department of Astrophysics, Department of Physics, University of Oxford, Keble Road, Oxford OX1 3RH, UK
Received 2024 November 16; revised 2025 January 22; accepted 2025 February 3; published 2025 May 12

Abstract

We compare measurements of star formation efficiency to cloud-scale gas properties across the PHANGS– ALMA sample. Dividing 67 galaxies into 1.5 kpc scale regions, we calculate the molecular gas depletion time $\tau_{\rm dep}^{\rm mol} = \Sigma_{\rm mol}/\Sigma_{\rm SFR}$ and the star formation efficiency per freefall time $\epsilon_{\rm ff}^{\rm mol} = \tau_{\rm ff}/\tau_{\rm dep}^{\rm mol}$ for each region. Then we test how $\tau_{\rm dep}^{\rm mol}$ and $\epsilon_{\rm ff}^{\rm mol}$ vary as functions of the regional mass-weighted mean molecular gas properties on cloud scales (60–150 pc): gas surface density, $\langle\Sigma_{\rm mol}^{\rm cloud}\rangle$, velocity dispersion, $\langle\sigma_{\rm mol}^{\rm cloud}\rangle$, virial parameter, $\langle\alpha_{\rm vir}^{\rm cloud}\rangle$, and gravitational freefall time, $\langle\tau_{\rm ff}^{\rm cloud}\rangle$. $\langle\tau_{\rm ff}^{\rm cloud}\rangle$ and $\tau_{\rm dep}^{\rm mol}$ correlate positively, consistent with the expectation that gas density plays a key role in setting the rate of star formation. Our fiducial measurements suggest $\tau_{\rm dep}^{\rm mol} \propto \langle\tau_{\rm ff}^{\rm cloud}\rangle^{0.5}$ and $\epsilon_{\rm ff}^{\rm mol} \approx 0.34\%$, though the exact numbers depend on the adopted fitting methods. We also observe anticorrelations between $\tau_{\rm dep}^{\rm mol}$ and $\langle\Sigma_{\rm mol}^{\rm cloud}\rangle$ and between $\tau_{\rm dep}^{\rm mol}$ and $\langle\sigma_{\rm mol}^{\rm cloud}\rangle$. All three correlations may reflect the same underlying link between density and star formation efficiency combined with systematic variations in the degree to which self-gravity binds molecular gas in galaxies. We highlight the $\tau_{\rm dep}^{\rm mol}$–$\langle\sigma_{\rm mol}^{\rm cloud}\rangle$ relation because of the lower degree of

[31] NASA Hubble Fellow.
[32] Jansky Fellow of the National Radio Astronomy Observatory.
[33] ARC DECRA Fellow.

correlation between the axes. Contrary to theoretical expectations, we observe an anticorrelation between $\tau_{\rm dep}^{\rm mol}$ and $\langle\alpha_{\rm vir}^{\rm cloud}\rangle$ and no significant correlation between $\epsilon_{\rm ff}^{\rm mol}$ and $\langle\alpha_{\rm vir}^{\rm cloud}\rangle$. Our results depend sensitively on the adopted CO-to-H_2 conversion factor, with corrections for excitation and emissivity effects in inner galaxies playing an important role. We emphasize that our simple methodology and clean selection allow for easy comparison to numerical simulations and highlight this as a logical next direction.

Unified Astronomy Thesaurus concepts: Star formation (1569); Disk galaxies (391); Interstellar medium (847); Molecular gas (1073)

Materials only available in the online version of record: machine-readable tables

1. Introduction

Stars form from clouds of molecular gas, with star formation and molecular gas well-correlated across nearby galaxies (e.g., T. Wong & L. Blitz 2002; F. Bigiel et al. 2008; A. K. Leroy et al. 2008; A. Schruba et al. 2011; R. C. Kennicutt & N. J. Evans 2012). Thanks to new surveys by the Atacama Large Millimeter/submillimeter Array (ALMA), we now know that the ≈100 pc "cloud-scale" properties of molecular gas—including surface density, velocity dispersion, and dynamical state—vary systematically, responding to and reflecting their galactic environment (e.g., J. Sun et al. 2018; A. Schruba et al. 2019; J. Sun et al. 2022; E. Schinnerer & A. K. Leroy 2024). So far, observations only weakly constrain how these variations in cloud-scale gas properties affect the process of star formation. In other words, a major open question in the field of star formation remains: "How do the properties of the parent molecular clouds affect the efficiency and rate of star formation?"

The initial properties of a cloud of gas should affect the rate at which stars form. In a given environment and at fixed mass, denser clouds will be more tightly bound by self-gravity. A cloud with a higher mean density, $\rho_{\rm mol}^{\rm cloud}$, will also have a shorter corresponding cloud-scale gravitational freefall time, $\tau_{\rm ff}^{\rm cloud} = \sqrt{3\pi/(32G\rho_{\rm mol}^{\rm cloud})}$ and might be expected to collapse to form stars faster, all other things being equal. For motions dominated by supersonic, isothermal turbulence, the cloud-scale velocity dispersion (which reflects the Mach number via $\mathcal{M} \propto \sigma_{\rm mol}^{\rm cloud}$) relates to the width of the density distribution (e.g., E. Vazquez-Semadeni 1994; P. Padoan & Å. Nordlund 2002). Meanwhile, the density distribution sets the fraction of high-density, gravitationally bound gas (e.g., M. R. Krumholz & C. F. McKee 2005). The densest molecular gas is observed to be the immediate site for star formation and to correlate with tracers of star formation in the Milky Way and other galaxies (Y. Gao & P. M. Solomon 2004; C. J. Lada et al. 2010; S. Garcìa-Burillo et al. 2012; N. J. I. Evans et al. 2014; M. J. Jiménez-Donaire et al. 2019). The balance between kinetic and gravitational energy, often expressed as the virial parameter, $\alpha_{\rm vir} \equiv 2K/U$, will also affect the ability of gas to collapse and form stars. In both analytic theory and numerical simulations, $\alpha_{\rm vir}$ plays a main role in setting $\epsilon_{\rm ff}$ when all other factors are equal (M. R. Krumholz & C. F. McKee 2005; P. Padoan et al. 2012; C. Federrath & R. S. Klessen 2013; J.-G. Kim et al. 2021), though models in which star formation is dynamically triggered (e.g., Y. Fukui et al. 2021) or in which clouds exist in a state of approximate freefall (e.g., E. Vázquez-Semadeni et al. 2024) also remain viable.

Observationally, this picture is less clear. Despite decades of studies of molecular cloud properties, there are relatively few quantitative, large-scale comparisons between the efficiency of star formation and the cloud-scale properties of molecular gas. The studies that do exist mainly concentrate on a single region or galaxy, and often focus on a few specific prototype spiral galaxies (e.g., M51, M83, IC 342; S. E. Meidt et al. 2013; A. K. Leroy et al. 2017a; A. Hirota et al. 2018; M. Querejeta et al. 2023) with A. Schruba et al. (2019) and J. Sun et al. (2022) almost the only two studies that compare cloud properties, $\tau_{\rm dep}^{\rm mol} \equiv M_{\rm mol}/{\rm SFR}$, and $\epsilon_{\rm ff} \equiv \tau_{\rm ff}/\tau_{\rm dep}^{\rm mol}$ across significant samples of galaxies and environments. Overall, these works find mixed or weak evidence for any general correlation between $\epsilon_{\rm ff}$ and $\alpha_{\rm vir}$ (A. K. Leroy et al. 2017a; A. Schruba et al. 2019). Even the relationship of $\tau_{\rm dep}^{\rm mol}$ to cloud-scale mean density, expressed as $\tau_{\rm ff}$, often appears weaker than the theoretically expected $\tau_{\rm dep}^{\rm mol} \propto \tau_{\rm ff}$ or even nonexistent (A. K. Leroy et al. 2017a; M. Querejeta et al. 2023; J. Sun et al. 2023).

Milky Way studies of local clouds demonstrate a clear connection between the distribution of gas density in a cloud and star formation activity (J. Kainulainen et al. 2009; C. J. Lada et al. 2010, 2012; N. J. I. Evans et al. 2014). However, most of these studies target a narrow range of environments with limited statistical power, partially because of the difficulty of accessing the spatially or time-averaged efficiency of star formation from our position within the Milky Way. In one of the most general studies to date, N. J. Evans et al. (2022) considered clouds across the whole Milky Way disk and found evidence of a correlation between $\alpha_{\rm vir}$ and $\epsilon_{\rm ff}$. They also showed that this conclusion depends on methodology, particularly the approach used to estimate molecular gas mass.

In this paper, we attempt to take a next logical step addressing this question by comparing star formation activity to cloud-scale gas properties using the largest homogeneous cloud-scale data set on molecular gas in galaxies, PHANGS–ALMA (A. K. Leroy et al. 2021). Specifically, we compare the molecular gas depletion time ($\tau_{\rm dep}^{\rm mol} \equiv M_{\rm mol}/{\rm SFR}$), and the star formation efficiency per freefall time ($\epsilon_{\rm ff} \equiv \tau_{\rm ff}/\tau_{\rm dep}^{\rm mol}$) to the mass-weighted mean molecular gas properties on cloud scales. This paper builds on previous work using PHANGS–ALMA and acts as a direct follow-up to J. Sun et al. (2022), but represents the first systematic attempt to correlate the cloud-scale gas properties with $\tau_{\rm dep}^{\rm mol}$ and $\epsilon_{\rm ff}$ across the whole data set.

We adopt the cross-scale methodology developed in A. K. Leroy et al. (2016), A. K. Leroy et al. (2017a), A. Schruba et al. (2019), J. Sun et al. (2020a), and J. Sun et al. (2022). This approach, described in Section 2, breaks galaxies into ∼kiloparsec-sized regions and summarizes the smaller-scale molecular gas properties via mass-weighted averages. These properties include mass surface density ($\langle\Sigma_{\rm mol}^{\rm cloud}\rangle$), velocity dispersion ($\langle\sigma_{\rm mol}^{\rm cloud}\rangle$), and the dynamical state of the gas expressed via the virial parameter ($\langle\alpha_{\rm vir}^{\rm cloud}\rangle$). We compare these gas properties to the regional mean molecular gas depletion time ($\tau_{\rm dep}^{\rm mol}$) and star formation efficiency per gravitational freefall time ($\epsilon_{\rm ff}^{\rm mol}$). By working with these kiloparsec-sized regions, we average out the time evolution of

individual star-forming regions, which causes systematic changes in their apparent $\tau_{\rm dep}^{\rm mol}$ and $\epsilon_{\rm ff}^{\rm mol}$ (see A. Schruba et al. 2010; A. K. Leroy et al. 2013; V. A. Semenov et al. 2018, 2021; J. M. D. Kruijssen et al. 2019; M. Chevance et al. 2020; J. Kim et al. 2022). In practice, estimating $\Sigma_{\rm SFR}$ at this resolution also allows us to reduce stochasticity and utilize infrared (IR) data with limited $\approx 15''$ angular resolution. This approach should be simple to reproduce in numerical simulations and easy to apply to other data sets.

We present our core results in Section 3. We find that the estimated gravitational freefall time and molecular gas depletion time show the expected correlation, but the details depend sensitively on the adopted CO-to-H_2 conversion factor. This same relationship manifests as anticorrelations between $\tau_{\rm dep}^{\rm mol}$ and the cloud-scale surface density and velocity dispersion. On the other hand, our results comparing the virial parameter to $\tau_{\rm dep}^{\rm mol}$ and the star formation efficiency per freefall time seem to suggest that star formation becomes more efficient when the virial parameter is higher. This is opposite to theoretical expectations for turbulent gas clouds, which predict more efficient star formation for lower virial parameter.

In discussing the results, we suggest a path forward on this topic. We highlight rigorous comparison between observations and numerical simulations as an immediately possible, highly promising next step. In this regard, we emphasize that our measurements are easy to reproduce in simulations of galaxies, and we give a concrete checklist to do so in Appendix A. On intermediate timescales, we also discuss the need for next-generation data sets that cover diverse environments with much higher physical resolution, high completeness, and reliable cloud-scale indicators of star formation activity.

2. Data and Methods

We measure how star formation efficiency correlates with diagnostics that trace the physical state of molecular gas across local galaxies. To do this, we compare cloud-scale ($\ell = 150$ pc FWHM resolution) gas properties to the mean molecular gas depletion time over 1.5 kpc diameter hexagonal regions, which collectively cover the area mapped by the PHANGS–ALMA survey (A. K. Leroy et al. 2021). PHANGS–ALMA targeted nearby ($d \lesssim 20$ Mpc), low to moderately inclined ($i \lesssim 75°$), relatively massive ($\log_{10} M_\star/M_\odot \gtrsim 9.75$, star-forming ($\log_{10} M_\star/{\rm SFR} > -11\,{\rm yr}^{-1}$) galaxies and offers a representative view of massive galaxies on or near the star-forming main sequence.

We conduct our analysis using the high-level data products ("the PHANGS mega-tables") assembled by J. Sun et al. (2022, 2023). They break galaxies into individual subgalactic regions and then measure a rich set of galaxy structural, stellar, and ISM properties in each region. Here we consider their main data product, which breaks 80 massive, star-forming disk galaxies from PHANGS–ALMA into individual 1.5 kpc hexagonal regions. Within each region, the "mega-tables" record star formation activity, the total molecular gas mass, and the mass-weighted mean averages of cloud-scale gas properties. We summarize the quantities relevant to our analysis below and in Table 1 and refer to J. Sun et al. (2022) and J. Sun et al. (2023) for detailed descriptions of how all other quantities are calculated. Appendix A gives a step-by-step guide to reproduce our measurements, e.g., to compare numerical simulations to PHANGS–ALMA.

The core data sets aggregated by J. Sun et al. (2022) that contribute to our measurements are: the PHANGS–ALMA CO (2–1) maps (A. K. Leroy et al. 2021); ground-based narrowband Hα maps (A. Razza et al. 2025, in preparation; see E. Schinnerer et al. 2019; H.-A. Pan et al. 2022; M. Querejeta et al. 2024); GALEX (D. C. Martin et al. 2005) ultraviolet images compiled by A. K. Leroy et al. (2019); the

Table 1
Experiment Summary

	Mass-weighted Region-averaged Cloud-scale Gas Properties (Mass-weighted Averages Estimated in Each 1.5 kpc Diameter Region Based on CO (2–1) Emission)
$\langle \Sigma_{\rm mol}^{\rm cloud} \rangle$	Cloud-scale molecular gas mass surface density in $M_\odot\,{\rm pc}^{-2}$. Estimated from CO (2–1) line intensity using $\alpha_{\rm CO}^{2-1}$ from E. Schinnerer & A. K. Leroy (2024). Corrected for completeness and inclination following J. Sun et al. (2022).
$\langle \tau_{\rm ff}^{\rm cloud} \rangle$	Gravitational freefall time in years. Calculated via $\tau_{\rm ff} = \sqrt{3\pi/(32 G \rho_{\rm mol}^{\rm cloud})}$ and $\rho = 3 M_{\rm mol}^{\rm beam}/(4\pi R_{\rm pix}^3)$. $R_{\rm pix} = \min\,[\ell/2, (\ell^2 H_{\rm mol}/(8\cos i))^{1/3}]$ following J. Sun et al. (2022).
$\langle \sigma_{\rm mol}^{\rm cloud} \rangle$	Cloud-scale velocity dispersion in kilometers per second. Calculated via the CO (2–1) line effective width and corrected for inclination and completeness.
$\langle \alpha_{\rm vir}^{\rm cloud} \rangle$	Dimensionless virial parameter $\alpha_{\rm vir} = 2K/U$ considering only gas self-gravity. Calculated via $\alpha_{\rm vir}^{\rm cloud} = 5\sigma_{\rm mol}^2 R_{\rm pix}/(fGM_{\rm mol}^{\rm beam})$.
	Region-averaged Quantities Related to Star Formation Efficiency (calculated by averaging all emission in each large 1.5 kpc diameter region)
$\Sigma_{\rm mol}^{\rm kpc}$	Mean molecular gas surface density over each 1.5 kpc region in $M_\odot\,{\rm pc}^{-2}$.
$\Sigma_{\rm SFR}^{\rm kpc}$	Mean star formation rate surface density over each 1.5 kpc region in $M_\odot\,{\rm yr}^{-1}\,{\rm kpc}^{-2}$.
$\tau_{\rm dep}^{\rm mol}$	Molecular gas depletion time in years, defined as $\tau_{\rm dep}^{\rm mol} = \Sigma_{\rm mol}^{\rm kpc}/\Sigma_{\rm SFR}^{\rm kpc}$.
$\epsilon_{\rm ff}^{\rm mol}$	Dimensionless star formation efficiency per freefall time, defined as $\epsilon_{\rm ff}^{\rm mol} = \langle \tau_{\rm ff}^{\rm cloud} \rangle / \tau_{\rm dep}^{\rm mol}$[a].
	CO-to-H_2 Conversion Factor (following E. Schinnerer & A. K. Leroy 2024 and based on references given in the text)
$\alpha_{\rm CO}^{2-1}$	Calculated via $\alpha_{\rm CO,MW}^{1-0} \times f(Z) \times g(\Sigma_\star) \times R_{21}(\Sigma_{\rm SFR})^{-1}$
$\alpha_{\rm CO,MW}^{1-0}$	$=4.35\ M_\odot\,{\rm pc}^{-2}\,({\rm K\,km\,s^{-1}})^{-1}$; Milky Way CO (1-0) conversion factor (A. D. Bolatto et al. 2013)
$f(Z)$	$=(Z/Z_\odot)^{-1.5}$; metallicity-dependent "CO-dark" term
$g(\Sigma_\star)$	$=(\max\,(\Sigma_\star, 100\ M_\odot\,{\rm pc}^{-2})/100\ M_\odot\,{\rm pc}^{-2})^{-0.25}$; "starburst" emissivity term following I.-D. Chiang et al. (2024)
$R_{21}(\Sigma_{\rm SFR})$	$=0.65(\Sigma_{\rm SFR}/0.018\ M_\odot\,{\rm yr}^{-1}\,{\rm kpc}^{-2})^{0.125}$ with min 0.35, max 1.0; CO line excitation term
	Data Selection (requiring cloud-scale CO flux completeness $f_{\rm comp} > 0.5$, and $\langle \Sigma_{\rm mol}^{\rm cloud} \rangle > 20\ M_\odot\,{\rm pc}^{-2}$) At $\ell = 150$ pc, this selection scheme yields 841 independent, 1.5 kpc hexagonal regions in 67 galaxies

Notes. Calculations and database described in detail in J. Sun et al. (2022) and J. Sun et al. (2023). Conversion factor treatment described in E. Schinnerer & A. K. Leroy (2024). i refers to galaxy inclination, ℓ to cloud-scale data resolution (beam FWHM), $H_{\rm mol}$ to the assumed FWHM vertical thickness of the molecular layer, $M_{\rm mol}^{\rm beam} = \Sigma_{\rm mol}^{\rm cloud} A_{\rm beam}$ with $A_{\rm beam} = \pi\theta^2/(4\ln 2)$.
[a] $\epsilon_{\rm ff}^{\rm mol}$ combines region-averaged properties and mass-weighted cloud-scale properties. See Section 3.6 for discussion.

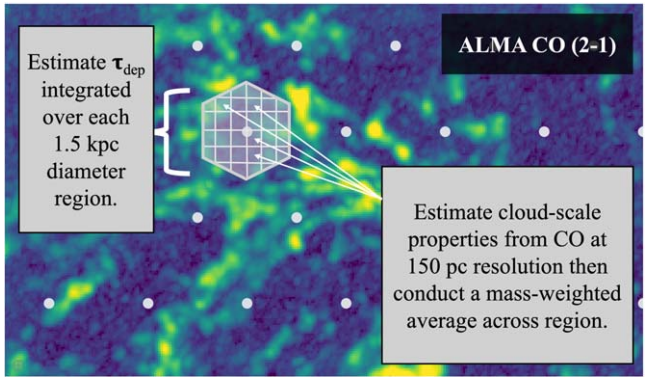

Figure 1. Illustration of our experiment over a region in a CO (2–1) peak intensity map from PHANGS–ALMA. We cover each galaxy with 1.5 kpc diameter hexes. Within each region, we measure the average τ_{dep}^{mol}. We also measure the surface density, line width, gravitational freefall time, and virial parameter at higher 150 pc resolution. Then within each region, we weight these by mass and calculate the mass-weighted average 150 pc value for each property, which we write $\langle X^{cloud} \rangle$. See Table 1 and J. Sun et al. (2022, 2023).

Wide-field Infrared Survey Explorer (WISE; E. L. Wright et al. 2010) 3.4–22 μm images compiled by A. K. Leroy et al. (2019); and IRAC 3.6 μm images (K. Sheth et al. 2010; M. Querejeta et al. 2021). We adopt distances and orientation parameters for all PHANGS–ALMA targets as measured and compiled by P. Lang et al. (2020), G. S. Anand et al. (2021), and A. K. Leroy et al. (2021).

2.1. Cloud-scale Gas Properties

To assess the physical state of molecular gas, we use cloud-scale (physical beam size $\ell = 150$ pc) imaging[34] of the CO (2–1) line, which traces the bulk of the molecular gas. Within each region of each galaxy, we measure four gas properties for each individual line of sight where CO is detected. Then, we weight each line of sight by the local gas surface density to derive mass-weighted, region-averaged molecular gas properties. This mass-weighting scheme, illustrated in Figure 1, is intended to yield estimates of the physical conditions that set the star formation rate per unit gas, i.e., τ_{dep}^{mol}, in the region. It has been described in detail by A. K. Leroy et al. (2016, 2017a), D. Utomo et al. (2018), and J. Sun et al. (2022). We refer to quantities computed via this cross-scale averaging as $\langle X^{cloud} \rangle$, indicating original measurements on cloud scales followed by weighted averaging over the 1.5 kpc hexagonal regions.

We focus on four gas properties, summarized in Table 1, that should be relevant to the efficiency of star formation:

1. Cloud-scale molecular gas surface density (Σ_{mol}^{cloud}). The molecular gas mass per unit area relates to the density of the gas, its gravitational potential, and its shielding from external radiation.
2. Gravitational freefall time (τ_{ff}^{cloud}). Based on Σ_{mol}^{cloud} and an estimated line-of-sight depth for the gas (see discussion of R_{pix} below), J. Sun et al. (2022) estimated the mass volume density, ρ_{mol}^{cloud}, and the corresponding gravitational freefall time τ_{ff}^{cloud}. Note that the region averaging for τ_{ff}^{cloud} follows a weighting scheme that ensures $\tau_{dep}^{mol} \propto \langle \tau_{ff}^{cloud} \rangle$ for a fixed ϵ_{ff}^{mol} (see J. Sun et al. 2022).
3. Cloud-scale molecular gas velocity dispersion (σ_{mol}^{cloud}). Within individual clouds, turbulence is expected to make a significant contribution to the CO line width (although at these scales, we may also worry about blending of multiple distinct components, bulk motions due to the galactic potential, or collapse of clouds; e.g., J. C. Ibáñez-Mejìa et al. 2016; S. E. Meidt et al. 2018; J. D. Henshaw et al. 2020). In cases where the line width is dominated by supersonic, isothermal turbulence, the gas velocity dispersion (reflected by the line width) should be proportional to the Mach number of the turbulence (e.g., see M.-M. Mac Low & R. S. Klessen 2004). This, in turn, relates to the expected width of the gas density distribution (e.g., P. Padoan & Å. Nordlund 2002). All other things being equal, a broader density distribution should lead to more dense, potentially star-forming gas.
4. The virial parameter is α_{vir}^{cloud}. The virial parameter $\alpha_{vir} = 2K/U \propto \sigma_{mol}^2/(\Sigma_{mol} \ R_{cloud})$ expresses the ratio of kinetic energy to potential energy associated with self-gravity in the gas (see F. Bertoldi & C. F. McKee 1992; C. F. McKee & E. G. Zweibel 1992, though see discussion for alternate interpretations in J. Ballesteros-Paredes 2006). Gas with a lower virial parameter should be prone to collapse and therefore more susceptible to star formation. Many theories of turbulence-regulated star formation predict an anticorrelation between α_{vir}^{cloud} and ϵ_{ff}^{mol} (e.g., P. Padoan & Å. Nordlund 2011; C. Federrath & R. S. Klessen 2012), and a similar relationship is also seen in simulations (P. Padoan et al. 2012; J.-G. Kim et al. 2021). As with τ_{ff}^{cloud}, α_{vir}^{cloud} requires adopting a relevant size scale, R_{pix}.

For both τ_{ff}^{cloud} and α_{vir}^{cloud}, we require an adopted size scale (see Table 1). Following J. Sun et al. (2022), we take the relevant scale to be $R_{pix} \equiv (\ell^2 H_{mol}/(8 \cos i))^{1/3}$ at the fiducial $\ell = 150$ pc resolution, with $H_{mol} = 100$ pc. This assumes that the mass measured in each beam is spread over the entire beam and over a line-of-sight depth of $H_{mol}/\cos i$, with $H_{mol} = 100$ pc being the adopted molecular gas disk scale height (e.g., M. Heyer & T. M. Dame 2015). In a similar analysis targeting M51, A. K. Leroy et al. (2017a) explored the difference between fixed and dynamical estimates of H and found qualitatively consistent results between the two approaches. Moreover, J. Sun et al. (2022) showed a good overall match between results for an object oriented analysis, where size is measured from morphological analysis, and this sight line based approach. For more information on R_{pix}, as well as the definition, calculation, and physical meaning of these and other quantities, see discussions in J. Sun et al. (2020b), J. Sun et al. (2022), E. Rosolowsky et al. (2021), and E. Schinnerer & A. K. Leroy (2024).

The main difference here compared to J. Sun et al. (2022) or E. Rosolowsky et al. (2021) is that we adopt the new CO-to-H_2 conversion factor α_{CO}^{2-1} recommended by E. Schinnerer & A. K. Leroy (2024).[35] This prescription, which we reproduce in Table 1, attempts to account for excitation variations, emissivity variations, and metallicity effects based on

[34] Following, e.g., E. Schinnerer & A. K. Leroy (2024), we refer to observations that match the beam to the size of a massive molecular cloud as "cloud-scale" imaging, in contrast to "resolved cloud" imaging or "resolved galaxy" imaging.

[35] Our α_{CO} estimates are calculated region-by-region, so when we conduct region averages, we assume a fixed α_{CO} within each region.

synthesizing work by A. D. Bolatto et al. (2013), G. Accurso et al. (2017), M. Gong et al. (2020), C.-Y. Hu et al. (2022), J. Sun et al. (2020a), J. Sun et al. (2022), J. S. den Brok et al. (2021), A. K. Leroy et al. (2022), Y.-H. Teng et al. (2023), and I.-D. Chiang et al. (2024). In practice, it resembles a refined version of the α_{CO} recommended by A. D. Bolatto et al. (2013). To assess the impact of this choice, we also run our analysis using a fixed Galactic α_{CO}. We discuss that the choice of α_{CO} exerts a large impact on our results in Section 3.5.

2.2. Star Formation Rate per Unit Gas

We compare region-averaged cloud-scale gas properties to two measures of the efficiency with which molecular gas forms stars. The molecular gas depletion time,

$$\tau_{dep}^{mol} = \frac{\Sigma_{mol}^{kpc}}{\Sigma_{SFR}^{kpc}}, \quad (1)$$

expresses the time needed for current star formation to consume the molecular gas reservoir without replenishment. Here Σ_{mol}^{kpc} and Σ_{SFR}^{kpc} are the mean molecular gas and star formation rate surface densities over the whole large 1.5 kpc averaging aperture.[36] Although τ_{dep}^{mol} is formally a timescale, the physical meaning here is that it expresses the star formation rate per unit molecular gas mass. That is, $(\tau_{dep}^{mol})^{-1}$ is the "specific" star formation rate of molecular gas, so that a short τ_{dep}^{mol} indicates a high rate of star formation per unit molecular gas.

We also compute the star formation efficiency per freefall time,

$$\epsilon_{ff}^{mol} = \frac{\langle \tau_{ff}^{cloud} \rangle}{\tau_{dep}^{mol}}, \quad (2)$$

which contrasts τ_{dep}^{mol} with the gravitational freefall time, τ_{ff}^{cloud}, estimated from the cloud-scale CO imaging. ϵ_{ff}^{mol} expresses the efficiency of star formation relative to uninhibited gravitational collapse. This is viewed as a theoretically important quantity (e.g., C. F. McKee & E. C. Ostriker 2007; C. Federrath & R. S. Klessen 2012, 2013; M. R. Krumholz 2014) and is often implemented as a controlling parameter in subgrid models for star formation in numerical simulations (e.g., N. Katz 1992; P. F. Hopkins et al. 2011; J.-h. Kim et al. 2014; O. Agertz et al. 2021; V. A. Semenov et al. 2021). Nonetheless, we caution that comparing ϵ_{ff}^{mol} to cloud-scale gas properties unavoidably involves plotting highly correlated quantities against one another, because they all depend on the same cloud-scale CO imaging data.

As with the cloud-scale gas properties, we estimate Σ_{mol} from PHANGS–ALMA CO (2–1) imaging using our adopted CO-to-H_2 conversion factor. At the 1.5 kpc resolution where we calculate Σ_{mol} and τ_{dep}^{mol}, PHANGS–ALMA yields high significance CO detection for almost every region, and CO flux completeness at low resolution plays little role in our data selection. By default, we estimate Σ_{SFR} combining Hα narrowband measurements and WISE 22 μm mid-infrared emission. These measurements follow F. Belfiore et al. (2023) as implemented by J. Sun et al. (2023) using narrowband Hα maps from A. Razza et al. (2025, in preparation) and 22 μm WISE4 maps from A. K. Leroy et al. (2019). When Hα maps are not available, we instead combine GALEX FUV emission and WISE 22 μm emission, and in a handful of cases, we use only WISE 22μm emission. Both J. Sun et al. (2023) and M. Querejeta et al. (2024) have both considered star formation scaling relations in this data set and have shown that using narrowband Hα and/or Hα+22 μm matches the results using the "gold standard" Very Large Telescope (VLT)/MUSE maps to ≈0.1 dex accuracy (though see discussion about next steps in Section 4.6).

2.3. Data Selection and Completeness

Measuring Σ_{mol}^{cloud}, σ_{mol}^{cloud}, and α_{vir}^{cloud} requires detecting and characterizing CO (2–1) emission over individual high-resolution lines of sight. In particular, robust detections are required to estimate the velocity dispersion, σ_{mol}, and virial parameter, α_{vir}. PHANGS–ALMA has sensitivity to detect individual $\sim 10^5$ $M_\odot$ GMCs in each 60–150 pc beam (see details in A. K. Leroy et al. 2021). However, over many regions, much of the CO flux appears associated with lines of sight that have lower surface brightness. This means only a fraction of the total CO flux in each 1.5 kpc region will enter our high-resolution cloud-scale gas property measurements. J. Sun et al. (2022) calculated this CO flux "completeness,"

$$f_{comp}^{CO} \equiv \frac{\sum_{\text{high S/N mask}} I_{CO}^{cloud}}{\sum_{\text{full region}} I_{CO}^{cloud}}, \quad (3)$$

by comparing the flux associated with individually detected high signal-to-noise sight lines (the numerator) to the total CO (2–1) flux[37] (the denominator). A high f_{comp}^{CO} means that our cloud-scale measurements capture the physical conditions of the *bulk* molecular gas, which is relevant to the overall τ_{dep}^{mol} in the region. Conversely, a low f_{comp}^{CO} indicates that we merely sample the "tip of the iceberg" and that our cloud-scale measurements are not representative and may have little relevance to region-averaged star formation activity.

J. Sun et al. (2022) corrected the measured cloud-scale surface density and $\langle \tau_{ff}^{cloud} \rangle$ in each hexagonal region to account for the effects of completeness by assuming a lognormal probability distribution function for the surface density, in good agreement with observations (see that paper). However, this implies that in regions with very low f_{comp}, the measured cloud properties will represent a rather aggressive extrapolation. With this in mind, we consider a region appropriate for the current analysis if the cloud-scale CO (2–1) completeness $f_{comp}^{CO} > 50\%$.

Figure 2 shows f_{comp}^{CO} in PHANGS–ALMA as a function of $\langle \Sigma_{mol}^{cloud} \rangle$. Based on this figure, we impose a $\langle \Sigma_{mol}^{cloud} \rangle$ cut at 20 $M_\odot$ pc^{-2} in addition to requiring $f_{comp}^{CO} > 50\%$. This yields a uniform data set and avoids the case where a few high completeness galaxies dominate low $\langle \Sigma_{mol}^{cloud} \rangle$ bins and drive our results on their own. Table 1 reports the number of hexagonal regions and galaxies that survive these cuts. Applying this

[36] Specifically, as in J. Sun et al. (2023), we convolve both Σ_{mol} and Σ_{SFR} to share a matched Gaussian kernel with FWHM equal to the hex diameter and then sample the value of those convolved maps at the hex center.

[37] This total flux is well-measured by summing the PHANGS–ALMA data, which include short- and zero-spacing data, without any aggressive high-resolution masking.

Table 2
Measurements for Individual Regions at $\ell = 150$ pc in 1.5 kpc Diameter Regions

Galaxy	Radius	$\tau_{\rm dep}^{\rm mol}$	$\frac{\tau_{\rm dep}^{\rm mol}}{\langle\tau_{\rm dep}^{\rm mol}\rangle_{\rm gal}}$	$\alpha_{\rm CO}^{2-1}$	i	$\log_{10} M_\star$	$\log_{10}$SFR	$\langle\Sigma_{mol}^{\rm cloud}\rangle$	$\langle\tau_{ff}^{\rm cloud}\rangle$	$\langle\sigma_{mol}^{\rm cloud}\rangle$	$\langle\alpha_{vir}^{\rm cloud}\rangle$	$\epsilon_{\rm ff}^{\rm mol}$	$\frac{\epsilon_{\rm ff}^{\rm mol}}{\langle\epsilon_{\rm ff}^{\rm mol}\rangle_{\rm gal}}$
	(kpc)	(Gyr)	(norm.)	($\frac{M_\odot\ {\rm pc}^{-2}}{{\rm K\ km\ s}^{-1}}$)	(°)	($M_\odot$)	($M_\odot\ {\rm yr}^{-1}$)	($M_\odot\ {\rm pc}^{-2}$)	(Myr)	(km s^{-1})			(norm.)
ESO097-013	0.0	0.11	0.35	1.73	64.3	10.5	0.6	182.0	3.57	24.5	7.38	0.0339	1.23
ESO097-013	1.54	0.42	1.42	3.26	64.3	10.5	0.6	25.0	9.4	8.1	4.93	0.0223	0.81
ESO097-013	3.36	0.99	3.32	6.65	64.3	10.5	0.6	54.0	6.69	6.0	1.04	0.0068	0.25
IC1954	0.0	0.92	0.66	5.26	57.1	9.7	−0.4	32.0	7.32	7.1	5.44	0.008	1.28
IC1954	1.82	1.71	1.23	8.29	57.1	9.7	−0.4	25.0	8.57	4.7	3.17	0.005	0.8
IC1954	1.82	1.41	1.02	8.14	57.1	9.7	−0.4	22.0	9.13	4.6	3.67	0.0065	1.04
IC1954	1.97	1.52	1.1	8.29	57.1	9.7	−0.4	29.0	7.98	5.2	3.65	0.0052	0.84
IC1954	1.97	1.54	1.11	8.42	57.1	9.7	−0.4	25.0	8.66	5.1	3.87	0.0056	0.9
IC1954	2.76	1.44	1.04	9.43	57.1	9.7	−0.4	21.0	9.31	4.6	3.56	0.0065	1.03

Note. This is a stub. The full table is available as a machine-readable table. Columns: (1) galaxy name, (2) galactocentric radius, (3) molecular gas depletion time, (4) molecular gas depletion time normalized to galaxy average, (5) CO (2–1) to H_2 conversion factor, (6) galaxy inclination, (7) galaxy integrated stellar mass, (8) galaxy integrated star formation rate, region-averaged mass-weighted molecular gas: (9) surface density, (10) gravitational freefall time, (11) line width, and (12) virial parameter, (13) star formation efficiency per freefall time, (14) star formation efficiency per freefall time normalized to galaxy average.

(This table is available in its entirety in machine-readable form in the online article.)

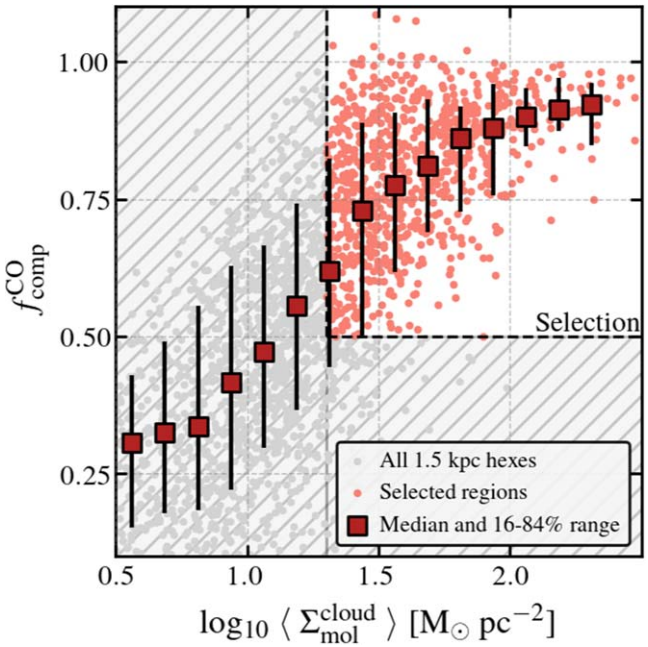

Figure 2. The fraction of total CO (2–1) emission detected at high signal to noise in each aperture, $f_{\rm comp}^{\rm CO}$, as a function of the mass-weighted mean cloud-scale surface density, $\langle\Sigma_{\rm mol}^{\rm cloud}\rangle$. The binned data show the median and 16th–84th percentile range in $f_{\rm comp}^{\rm CO}$ considering all regions. Completeness rises as a function of the mass-weighted mean cloud-scale surface density, with scatter reflecting variation in distance to the target and data quality. We analyze regions with $f_{\rm comp}^{\rm CO} > 0.5$ and $\langle\Sigma_{\rm mol}^{\rm cloud}\rangle > 20\ M_\odot\ {\rm pc}^{-2}$.

criteria to the $\ell = 150$ pc resolution PHANGS–ALMA data set in J. Sun et al. (2022), we select 841 regions in 67 galaxies.

2.4. Correlation Analysis, Binning, Fitting, and Uncertainties

While parameterized fitting and correlation analyses provide useful insights, we would like to first emphasize the region-by-region measurements as our key products. These represent our best estimates of $\tau_{\rm dep}^{\rm mol}$, $\epsilon_{\rm ff}^{\rm mol}$, and gas properties with a well-understood selection function for a representative set of nearby galaxies. We present the full measurement set in Table 2. Appendix A summarizes this section in a simple, step-by-step guide that can be used to reproduce matched measurements from simulations or other data sets.

We treat the cloud-scale gas properties as independent variables and measure how $\tau_{\rm dep}^{\rm mol}$ and $\epsilon_{\rm ff}^{\rm mol}$ (the y-axis) vary as a function of these mass-weighted average gas properties (the x-axis). We measure Spearman's rank correlation relating $\tau_{\rm dep}^{\rm mol}$ and $\epsilon_{\rm ff}^{\rm mol}$ to each property and fit y as a function of x for each gas property using the functional form

$$y = m(x - x_0) + b \tag{4}$$

where y refers to either $\log_{10}\tau_{\rm dep}^{\rm mol}$ or $\log_{10}\epsilon_{\rm ff}^{\rm mol}$, x to the $\log_{10}$ of one of the gas properties that we consider. We calculate x_0 as the median of the x data, then maximize the log-likelihood to infer m and b. We also include an intrinsic scatter term in the fit, but this tends to be very small given our adopted uncertainty estimates (see below). We therefore report σ, the robustly estimated rms residual of the data about each fit.

Because we average over large regions selected to have high $\langle\Sigma_{\rm mol}^{\rm cloud}\rangle$, the formal statistical uncertainty associated with any individual measurement is small. Instead, systematic effects dominate our uncertainties. In deriving the calibrations that we use for $\Sigma_{\rm SFR}$, F. Belfiore et al. (2023) found ≈0.15 dex point-to-point scatter between the estimators that we use and "gold standard" extinction corrected Hα estimates from MUSE (A. K. Leroy et al. 2019 found similar scatter comparing to S. Salim et al. 2016). Our $\alpha_{\rm CO}$ estimate heavily leverages the work of I.-D. Chiang et al. (2024), who found ≈0.2 dex scatter between their dust-based $\alpha_{\rm CO}^{2-1}$ and the fit to local conditions that we employ. Combining the uncertainties, we consider any individual $\tau_{\rm dep}^{\rm mol}$ estimate to be uncertain by ≈0.3 dex due to uncertainties in our ability to estimate star formation rates and molecular gas masses. We consider molecular gas surface densities to be uncertain by 0.2 dex at any scale, and $\tau_{\rm ff} \propto \Sigma_{\rm mol}^{-0.5}$ to be uncertain by 0.1 dex. The main systematic uncertainty on the mass-weighted line width, $\langle\sigma_{\rm mol}^{\rm cloud}\rangle$, is related to measurement technique and correction for sensitivity biases (see J. D. Henshaw et al. 2016; E. Koch et al. 2018; E. Rosolowsky et al. 2021); we consider these $\langle\sigma_{\rm mol}^{\rm cloud}\rangle$ values to be uncertain by ≈0.15 dex. When we include these uncertainty estimates in the fitting described above, we find little or no need for an intrinsic scatter term. This may imply

that the estimates are slightly conservative, i.e., too large, but they do appear grounded in the current literature.

We observe significant galaxy-to-galaxy scatter in our data, meaning that individual galaxies trace out offset relationships in the $\tau_{\rm dep}^{\rm mol}$ versus gas properties parameter space. This situation is common in resolved studies of star formation scaling relations (e.g., see A. K. Leroy et al. 2013) and likely reflects a mixture of physical scatter due to unplotted additional parameters and/or systematic uncertainties that operate galaxy by galaxy (e.g., calibration uncertainties, uncertainties in the adopted $\alpha_{\rm CO}$, SFR calibration uncertainties, etc.). We account for this in two ways. First we estimate uncertainties on our fits using a "per galaxy" bootstrapping approach, where we repeatedly re-draw N galaxies from the parent sample and refit the relation between $\tau_{\rm dep}^{\rm mol}$ and gas properties. Second, we construct a version of our plots in which we first normalize the $\tau_{\rm dep}^{\rm mol}$ or $\epsilon_{\rm ff}^{\rm mol}$ for each region by the mean $\tau_{\rm dep}^{\rm mol}$ or $\epsilon_{\rm ff}^{\rm mol}$ for the galaxy in which that region resides and then analyze the normalized results. We calculate the mean $\tau_{\rm dep}^{\rm mol}$ or $\epsilon_{\rm ff}^{\rm mol}$ used for normalization by a molecular mass ($\Sigma_{\rm mol}^{\rm kpc}$) weighted average over the selected regions for that galaxy.

For each variable pair (x, y), we distill the median and 16th–84th percentiles in y as a function of x. To do this, we apply two-dimensional Gaussian kernel density estimation (KDE) to the data, allowing the bandwidth to be chosen using the default "Scott's rule" implement in `scipy` (this typically yields bandwidths of $\lesssim$0.3 dex). We evaluate the density on a regularly spaced grid spanning the full range of the data in x and y. Then, we calculate the median and 16th–84th percentile range in y for each value of x in this grid. The results visually match the spine and span of the data well. We fit lines to the median trends, but found them to be similar to those found fitting the data and only report the fits to the data.

We emphasize that the choice to fit y (i.e., $\tau_{\rm dep}^{\rm mol}$ or $\epsilon_{\rm ff}^{\rm mol}$) while treating x (cloud-scale gas properties) as an independent variable has a significant impact on our results. Our data show significant scatter compared to the dynamic range in both x and y, and many of the correlations that we examine are relatively weak. Fitting x as a function of y or conducting a bivariate fit would yield different results. Our adopted scheme is motivated by the desire to address the question "Given some cloud-scale gas properties, how well can we predict $\tau_{\rm dep}^{\rm mol}$?" (see Section 1). Our selection (Section 2.3) also imposes a strong selection in x, which would need to be carefully accounted for in any bivariate fit (see, e.g., A. K. Leroy et al. 2013) but does not affect our adopted approach. The key point for the reader is that rigorous comparison to our fitting results should consider the same formulation of dependent and independent variable.

Finally, note that we examine many cases with correlated axes. In some cases, this correlation is explicit, e.g., $\epsilon_{\rm ff}^{\rm mol} \propto \langle(\Sigma_{\rm mol}^{\rm cloud})^{-0.5}\rangle$. In other cases, e.g., $\tau_{\rm dep}^{\rm mol}$ versus $\langle\Sigma_{\rm mol}^{\rm cloud}\rangle$, the correlation depends on a cross-scale relationship between $\Sigma_{\rm mol}$ and $\langle\Sigma_{\rm mol}^{\rm cloud}\rangle$. In many cases, our adopted $\alpha_{\rm CO}$ affects both axes. We indicate our expectations for covariance with a vector in each plot along with the typical uncertainties.

3. Results

Our selection yields gas properties, molecular gas depletion times, and estimates of the star formation efficiency per freefall time for 841 independent 1.5 kpc-sized regions in 67 galaxies with properties measured at $\ell = 150$ pc resolution (we also make measurements using higher-resolution CO data, though for fewer galaxies, and provide these in Appendix B). Table 1 summarizes the selection and other details of the experiment. Our core results are the measurements of and relationships between $\tau_{\rm dep}^{\rm mol}$, $\epsilon_{\rm ff}^{\rm mol}$, and cloud-scale gas properties. We present the measurements in Table 2, summarize the correlation analyses in Tables 3, 4, and 5, and illustrate the results in Sections 3.1–3.6, but first we show the properties of our selected regions in Figure 3.

The left panel in Figure 3 shows the region-averaged $\Sigma_{\rm SFR}$ as a function of $\Sigma_{\rm mol}$ for our working data set. These measurements do not involve cloud-scale information but simply show the resolved molecular Kennicutt–Schmidt relation at 1.5 kpc scales. Our selected regions span more than an order of magnitude in $\Sigma_{\rm SFR}$ and $\Sigma_{\rm mol}$. The selected data agree well with the power-law fit by J. Sun et al. (2023), shown by the dashed line,[38] in which $\Sigma_{\rm SFR} \propto \Sigma_{\rm mol}^{1.2}$. This slope reflects

Table 3
$\tau_{\rm dep}^{\rm mol}$ and Cloud-scale Gas Properties

x	Rank. Corr.	m	x_0	b	σ
…	…	…	…	9.33	0.3
$\log_{10}\langle\tau_{\rm ff}^{\rm cloud}\rangle$	0.3	0.49	6.85	9.31	0.26
(normalized)	0.38	0.4	…	…	0.18
$\log_{10}\langle\Sigma_{\rm mol}^{\rm cloud}\rangle$	−0.34	−0.28	1.66	9.32	0.25
(normalized)	−0.41	−0.22	…	…	0.17
$\log_{10}\langle\sigma_{\rm mol}^{\rm cloud}\rangle$	−0.3	−0.46	0.74	9.32	0.26
(normalized)	−0.31	−0.28	…	…	0.18
$\log_{10}\langle\alpha_{\rm vir}^{\rm cloud}\rangle$	−0.29	−0.2	0.52	9.32	0.26
(normalized)	−0.29	−0.12	…	…	0.19

Note. Results correlating $\tau_{\rm dep}^{\rm mol}$ with cloud-scale gas properties for our fiducial sample of regions with high gas surface density. Cloud-scale properties measured at 150 pc resolution, and our best estimate $\alpha_{\rm CO}$. Fit has form $y = m(x - x_0) + b$. Quantities defined in Table 1. Normalized results first normalize $\tau_{\rm dep}^{\rm mol}$ by the galaxy-average value.

Table 4
$\tau_{\rm dep}^{\rm mol}$ and Cloud-scale Gas Properties for Fixed $\alpha_{\rm CO}$

x	Rank. Corr.	m	x_0	b	σ
…	…	…	…	9.4	0.28
$\log_{10}\langle\tau_{\rm ff}^{\rm cloud}\rangle$	−0.17	−0.19	6.85	9.38	0.27
(normalized)	−0.03	−0.02	…	…	0.16
$\log_{10}\langle\Sigma_{\rm mol}^{\rm cloud}\rangle$	0.13	0.08	1.66	9.38	0.27
(normalized)	−0.03	−0.01	…	…	0.16
$\log_{10}\langle\sigma_{\rm mol}^{\rm cloud}\rangle$	0.14	0.2	0.74	9.37	0.27
(normalized)	0.09	0.07	…	…	0.16
$\log_{10}\langle\alpha_{\rm vir}^{\rm cloud}\rangle$	0.18	0.08	0.52	9.37	0.26
(normalized)	0.21	0.05	…	…	0.16

Note. Results correlating $\tau_{\rm dep}^{\rm mol}$ with cloud-scale gas properties for our fiducial sample of regions with high gas surface density. Cloud-scale properties measured at 150 pc resolution, and a fixed, Milky Way $\alpha_{\rm CO}$. Fit has the form $y = m(x - x_0) + b$. Quantities defined in Table 1. Normalized results first normalize $\tau_{\rm dep}^{\rm mol}$ by the galaxy-average value.

[38] Our CO-to-H_2 conversion factor follows the prescription in E. Schinnerer & A. K. Leroy (2024) while J. Sun et al. (2023) adopts the prescription by A. D. Bolatto et al. (2013) among others. Figure 3 shows that the two yield comparable results here.

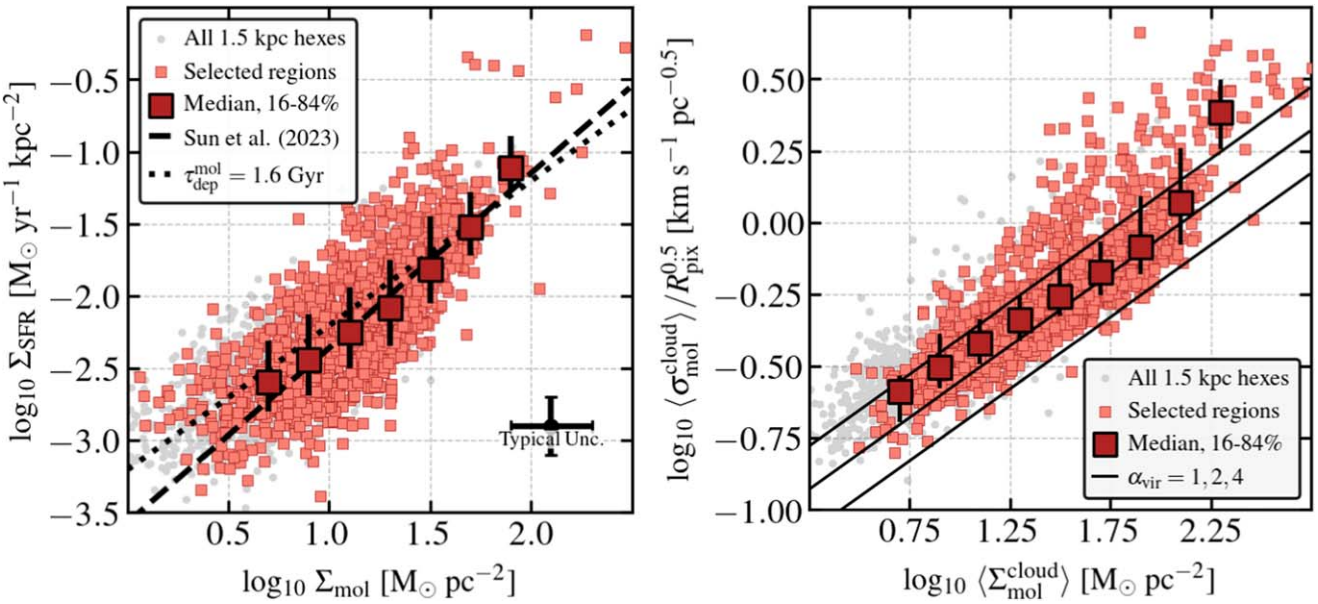

Figure 3. Analyzed region in key parameter spaces. Left panel: $\Sigma_{SFR} - \Sigma_{mol}$ space, i.e., the resolved molecular Kennicutt–Schmidt relation. Gray points show all 1.5 kpc hexes in the J. Sun et al. (2022) database. Red points show regions selected for our analysis based on their completeness and cloud-scale surface density (Section 2.3, Figure 2, Table 1). Dark points with error bars show the median and 16th–84th range Σ_{SFR} in bins of Σ_{mol}. Our selection imposes a bias toward molecular-gas rich regions, but within the covered part of parameter space, our analyzed regions reflect the overall $\Sigma_{SFR} - \Sigma_{mol}$ scaling seen in local galaxies (J. Sun et al. 2023). Right panel: cloud-scale mean $\langle\sigma_{mol}^{cloud}\rangle / R_{pix}^{0.5}$ as a function of $\langle\Sigma_{mol}^{cloud}\rangle$ (the "Heyer–Keto relation" capturing the mean dynamical state of molecular clouds) for the same regions, using the same symbols as the left panel. Selected data show ≈1 dex dynamic range in region-averaged gas and SFR surface density, >1.5 dex range in $\langle\Sigma_{mol}^{cloud}\rangle$, and ≈1 dex span in $\langle\sigma_{mol}^{cloud}\rangle / R_{pix}^{0.5}$, and they reflect the overall set of high surface density regions found in nearby, star-forming galaxies well.

Table 5
ϵ_{ff}^{mol} and Cloud-scale Gas Properties

x	Rank. Corr.	m	x_0	b	σ
…	…	…	…	−2.47	0.29
$\log_{10}\langle\tau_{ff}^{cloud}\rangle$	0.11	0.15	6.85	−2.43	0.28
(normalized)	−0.06	−0.03	…	…	0.18
$\log_{10}\langle\Sigma_{mol}^{cloud}\rangle$	0.0	0.0	1.66	−2.44	0.28
(normalized)	0.05	0.01	…	…	0.19
$\log_{10}\langle\sigma_{mol}^{cloud}\rangle$	0.02	0.01	0.74	−2.44	0.28
(normalized)	0.01	−0.01	…	…	0.19
$\log_{10}\langle\alpha_{vir}^{cloud}\rangle$	0.14	0.1	0.52	−2.45	0.27
(normalized)	0.17	0.05	…	…	0.18

Note. Results correlating ϵ_{ff}^{mol} with cloud-scale gas properties for our fiducial sample of regions with high gas surface density. Cloud-scale properties measured at 150 pc resolution, and our best estimate α_{CO}. Fit has the form $y = m(x - x_0) + b$. Quantities defined in Table 1. Normalized results first normalize ϵ_{ff}^{mol} by the galaxy-average value.

that the highest surface density regions in our targets also have the shortest τ_{dep}^{mol}.

The right panel in Figure 3 presents a complementary view, now with cloud-scale information. It shows mass-weighted, region-averaged, cloud-scale velocity dispersion normalized by the adopted size scale, $\langle\sigma_{mol}^{cloud}\rangle / R_{pix}^{0.5}$, as a function of the cloud-scale surface density, $\langle\Sigma_{mol}^{cloud}\rangle$. Our selection also samples >1.5 dex in $\langle\Sigma_{mol}^{cloud}\rangle$, and ≈1 dex in $\langle\sigma_{mol}^{cloud}\rangle$. On average, our target regions follow the "Heyer–Keto" relation of $\sigma_{mol}^{cloud} / R_{pix}^{0.5} \propto (\Sigma_{mol}^{cloud})^{0.5}$. This is expected among gas structures with similar dynamical state, i.e., similar α_{vir} values (illustrated by the solid black lines; see M. Heyer et al. 2009; M. Heyer & T. M. Dame 2015; J. Sun et al. 2018, 2020b; E. Schinnerer & A. K. Leroy 2024). As a result of this, $\langle\Sigma_{mol}^{cloud}\rangle$ and $\langle\sigma_{mol}^{cloud}\rangle$ are significantly correlated, and we will see similar relationships between τ_{dep}^{mol} and these two quantities.

While $\langle\Sigma_{mol}^{cloud}\rangle$ and $\langle\sigma_{mol}^{cloud}\rangle$ show a strong correlation, there is still substantial scatter and significant deviations from the fiducial Heyer–Keto relation. In particular, a subset of regions show enhanced $\langle\sigma_{mol}^{cloud}\rangle$ at fixed $\langle\Sigma_{mol}^{cloud}\rangle$. The gas in these regions has high $\langle\alpha_{vir}^{cloud}\rangle \propto (\sigma_{mol}^{cloud})^2 / (R_{pix}\,\Sigma_{mol}^{cloud})$ and thus appears less bound by self-gravity. These high $\langle\alpha_{vir}^{cloud}\rangle$ data often come from the inner parts of galaxies and show high $\langle\Sigma_{mol}^{cloud}\rangle$. There, stellar gravity can more strongly affect the molecular gas dynamical state, and unresolved streaming motions and shadowing of multiple components may also contribute to the observed broad CO line width (S. E. Meidt et al. 2013, 2018; J. Sun et al. 2018, 2020b; J. Henshaw et al. 2025, in preparation). We return to this point in more detail in Section 3.4.

3.1. Molecular Gas Depletion Time as a Function of Gravitational Freefall Time

Figure 4 plots τ_{dep}^{mol} as a function of the region-averaged cloud-scale gravitational freefall time, $\langle\tau_{ff}^{cloud}\rangle$. All other things being equal, higher-density gas should form stars faster, and the characteristic time for the gas to collapse under its own gravity, $\tau_{ff} \propto \rho^{-0.5} \propto (\Sigma_{mol}^{cloud})^{-0.5}$, has been considered a key timescale in this context.

Figure 4 does show a correlation between τ_{dep}^{mol} and $\langle\tau_{ff}^{cloud}\rangle$, with Spearman rank correlation coefficient 0.3 and p-value ≪0.001. Gas with higher density (low $\langle\tau_{ff}^{cloud}\rangle$) coincides with regions that show higher star formation rate per unit gas (low τ_{dep}^{mol}). The blue line showing fixed ϵ_{ff}^{mol} shows that a single ϵ_{ff}^{mol} can reasonably describe the bulk of the measurements. Most of

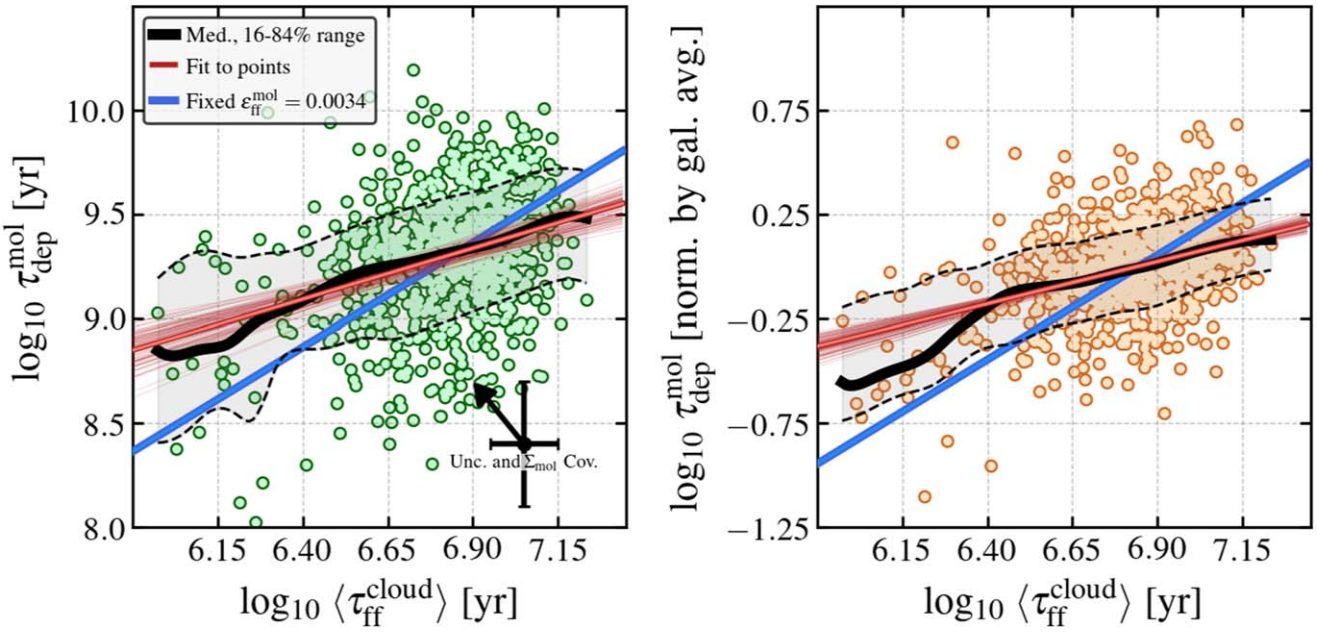

Figure 4. Region-averaged molecular gas depletion time, $\tau_{\rm dep}^{\rm mol}$, as a function of cloud-scale mean freefall time, $\langle \tau_{\rm ff}^{\rm cloud} \rangle$. Points show measurements for individual 1.5 kpc regions, and the black lines show the median and 16th–84th percentile range estimated as described in Section 2.4. The red line shows the best fit to the data (Table 3), with thin traces showing fits to versions of the data set that bootstrap resample the set of included galaxies. For comparison, the blue line shows the expectation for a fixed $\epsilon_{\rm ff}^{\rm mol}$ (i.e., $\tau_{\rm dep}^{\rm mol} \propto \langle \tau_{\rm ff}^{\rm cloud} \rangle$), and the black error bar indicates typical uncertainties with an arrow showing the sense of correlation between the axes (see Section 2). The left panel shows results for $\tau_{\rm dep}^{\rm mol}$ as measured directly from the data. The right panel shows the same data set, but first normalizes each $\tau_{\rm dep}^{\rm mol}$ measurement by the mean $\tau_{\rm dep}^{\rm mol}$ for that galaxy, thus removing the galaxy-to-galaxy scatter from the left plot. $\tau_{\rm dep}^{\rm mol}$ and $\langle \tau_{\rm ff}^{\rm cloud} \rangle$ correlate with each other, but the slope is shallower than that predicted for fixed $\epsilon_{\rm ff}^{\rm mol}$.

the data lie within ± 0.3 dex (i.e., a factor of 2) of the blue line (consistent with results using the same data set in J. Sun et al. 2023). A fixed $\epsilon_{\rm ff}^{\rm mol}$ thus provides a reasonable approximate description of the data. But in detail, $\epsilon_{\rm ff}^{\rm mol}$ tends to be somewhat higher (i.e., the points lie below the blue line) at high $\langle \tau_{\rm ff}^{\rm cloud} \rangle$, corresponding to low density. This manifests as a best-fit $\tau_{\rm dep}^{\rm mol}$–$\langle \tau_{\rm ff}^{\rm cloud} \rangle$ relation with slope $m = 0.49$ (the red line, Table 3). This is shallower than the $\tau_{\rm dep}^{\rm mol} \propto \langle \tau_{\rm ff}^{\rm cloud} \rangle$ expected for fixed $\epsilon_{\rm ff}^{\rm mol}$, though we reiterate that this specific slope depends on the choice to fit $\tau_{\rm dep}^{\rm mol}$ while treating $\langle \tau_{\rm ff}^{\rm cloud} \rangle$ as the independent variable (see Section 2.4).

The right panel in Figure 4 also shows $\tau_{\rm dep}^{\rm mol}$ as a function of $\langle \tau_{\rm ff}^{\rm cloud} \rangle$ but first normalizes $\tau_{\rm dep}^{\rm mol}$ by the galaxy-average value. Normalizing leads to an even sharper correlation (Table 3), with the rank correlation coefficient increasing to 0.38 after normalization. This indicates that $\tau_{\rm dep}^{\rm mol}$ correlates well with $\tau_{\rm dep}^{\rm mol}$ within individual galaxies. The best-fit $\tau_{\rm dep}^{\rm mol} - \langle \tau_{\rm ff}^{\rm cloud} \rangle$ slope becomes slightly shallower after normalization (Table 3), $m = 0.4$, but the overall picture appears similar as in the left panel.

Figure 5 shows why normalizing by galaxy-average $\tau_{\rm dep}^{\rm mol}$ sharpens the $\tau_{\rm dep}^{\rm mol} - \langle \tau_{\rm ff}^{\rm cloud} \rangle$ relation. We plot binned results for individual galaxies before any normalization in the left panel. To a large extent, galaxies trace offset relations in the $\tau_{\rm dep}^{\rm mol}$–$\langle \tau_{\rm ff}^{\rm cloud} \rangle$ space. This reflects some overall correlation of $\tau_{\rm dep}^{\rm mol}$ with host galaxy properties, with a general sense that lower-mass galaxies show shorter $\tau_{\rm dep}^{\rm mol}$ (i.e., darker lines tend to appear lower in Figure 5). This might reflect real physics, or might reflect that the metallicity dependence in our $\alpha_{\rm CO}$ prescription remains too weak (because metallicity correlates with $M_\star$; R. Maiolino & F. Mannucci 2019). Global variation of $\tau_{\rm dep}^{\rm mol}$ as a function of $M_\star$ has been considered extensively (see, e.g., A. Saintonge et al. 2011, 2017; A. Saintonge & B. Catinella 2022; A. Schruba et al. 2012; A. K. Leroy et al. 2013; L. J. Tacconi et al. 2020). For our purposes, the key points are that (1) $\langle \tau_{\rm ff}^{\rm cloud} \rangle$ variations do not appear to explain all of the observed galaxy-to-galaxy scatter (nor do $\langle \Sigma_{\rm mol}^{\rm cloud} \rangle$, $\langle \sigma_{\rm mol}^{\rm cloud} \rangle$, or $\alpha_{\rm vir}$ variations), and (2) $\tau_{\rm dep}^{\rm mol}$ correlates with $\langle \tau_{\rm ff}^{\rm cloud} \rangle$ more strongly within individual galaxies.

In the right panels in Figures 4 and 5, after normalization, most galaxies lie together along a common relation, with individual regions showing rms scatter ≈ 0.2 dex about the median trend. This represents $\sim\sqrt{2}$ times lower scatter than we find before normalizing, implying that about half the total scatter in $\tau_{\rm dep}^{\rm mol}$ can be attributed to galaxy-to-galaxy scatter, while the rest represents scatter within individual galaxies. This resembles results from previous work on $\tau_{\rm dep}^{\rm mol}$ and kiloparsec-scale star formation scaling relations by A. K. Leroy et al. (2013) and M. J. Jiménez-Donaire et al. (2019).

3.2. Molecular Gas Depletion Time as a Function of Cloud-scale Surface Density and Line Width

Figure 6 shows $\tau_{\rm dep}^{\rm mol}$ as a function of cloud-scale gas surface density, $\langle \Sigma_{\rm mol}^{\rm cloud} \rangle$, and velocity dispersion, $\langle \sigma_{\rm mol}^{\rm cloud} \rangle$. Table 3 reports results for the corresponding correlation analysis. $\tau_{\rm dep}^{\rm mol}$ anticorrelates with both quantities. Surface density and velocity dispersion represent more direct observables than $\langle \tau_{\rm ff}^{\rm cloud} \rangle$, and we therefore view these as our most fundamental results. They should be easy to reproduce by applying our methodology to simulations or other data sets (following Appendix A).

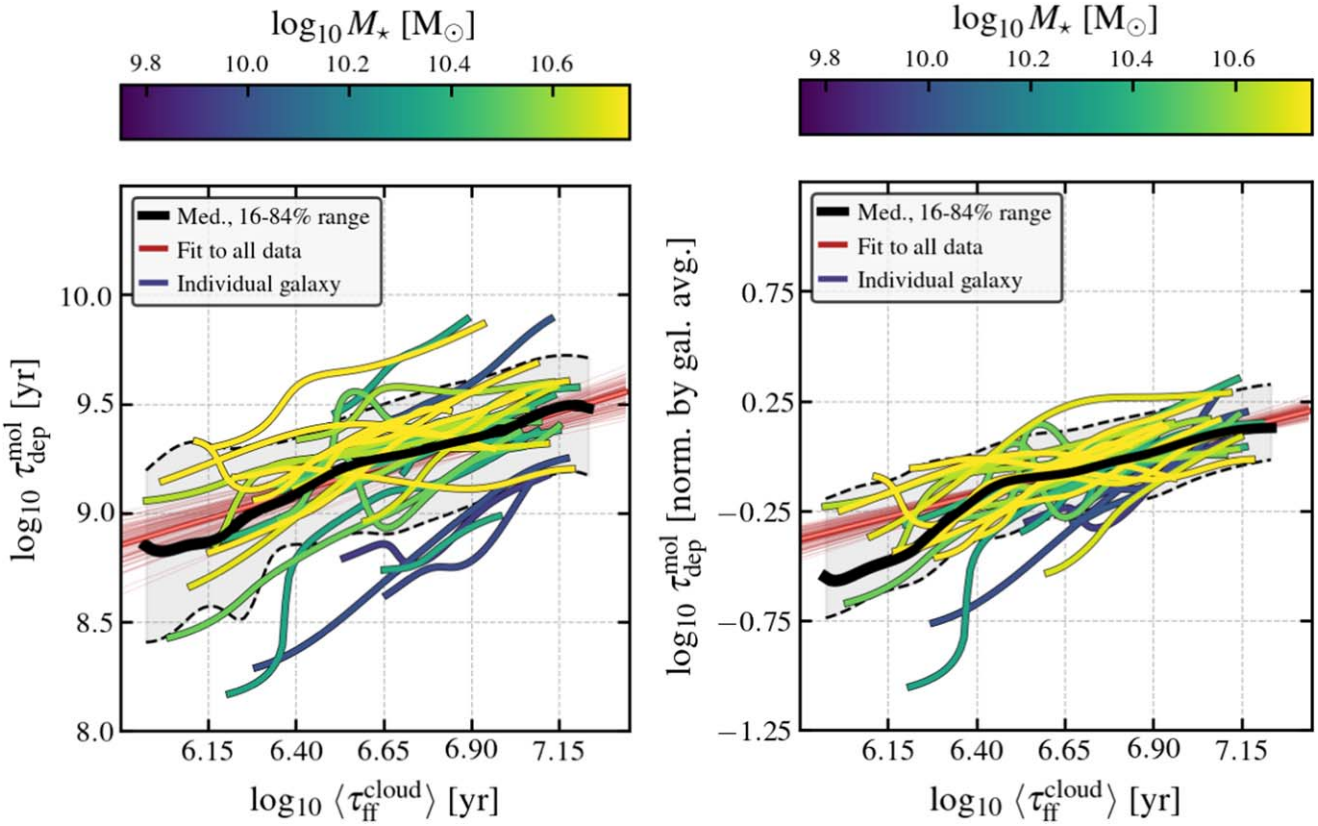

Figure 5. Traces of individual galaxies in the same $\tau_{\rm dep}^{\rm mol} - \langle \tau_{\rm ff} \rangle$ space shown in Figure 4. Each colored line shows the median trend for an individual galaxy, with color indicating the total stellar mass of that galaxy ($M_\star$). The left panel shows these traces in the $\tau_{\rm dep}^{\rm mol}$ vs. $\langle \tau_{\rm ff}^{\rm cloud} \rangle$ space. In the right panel, we first normalize $\tau_{\rm dep}^{\rm mol}$ by the mean value for each galaxy, thus removing overall galaxy-to-galaxy scatter in $\tau_{\rm dep}^{\rm mol}$. Individual galaxies show trends with a similar positive correlation to the overall median but significant galaxy-to-galaxy scatter in the slope, the range of $\langle \tau_{\rm ff}^{\rm cloud} \rangle$ covered, and their mean $\tau_{\rm dep}^{\rm mol}$.

To first order, Figures 4 and 6 could be viewed as three different manifestations of the same underlying relationship between gas density and star formation efficiency. Because[39]

$$\tau_{\rm dep}^{\rm mol} = \frac{\tau_{\rm ff}^{\rm cloud}}{\epsilon_{\rm ff}^{\rm mol}}$$
$$\tau_{\rm ff}^{\rm cloud} = \sqrt{\pi / (8 G \Sigma_{\rm mol}^{\rm cloud} / R_{\rm cloud})} \quad (5)$$

so that for a fixed $\epsilon_{\rm ff}^{\rm mol}$ and size scale,

$$\tau_{\rm dep}^{\rm mol} \propto \langle \Sigma_{\rm mol}^{\rm cloud} \rangle^{-0.5}. \quad (6)$$

The expected anticorrelation with $\langle \sigma_{\rm mol}^{\rm cloud} \rangle$ emerges because for fixed dynamical state, $\alpha_{\rm vir}$ ("the Heyer–Keto relation"; see M. Heyer et al. 2009; J. Sun et al. 2018; E. Rosolowsky et al. 2021; E. Schinnerer & A. K. Leroy 2024), $\Sigma_{\rm mol}$ and $\sigma_{\rm mol}$ are related as

$$\sigma_{\rm mol} = \sqrt{\alpha_{\rm vir} R \frac{f G \pi \Sigma_{\rm mol}}{5}} \quad (7)$$

where f is a geometrical factor related to the cloud density distribution (Table 1). Since $\sigma_{\rm mol} \propto \sqrt{\Sigma_{\rm mol}}$ at given $\alpha_{\rm vir}$ and size scale, we expect

$$\tau_{\rm mol}^{\rm dep} \propto \langle \sigma_{\rm mol}^{\rm cloud} \rangle^{-1}. \quad (8)$$

[39] Here we discuss general scalings among cloud properties, not our specific observables, and so omit the averaging notation.

The expected scaling between $\langle \sigma_{\rm mol}^{\rm cloud} \rangle$ and $\langle \Sigma_{\rm mol}^{\rm cloud} \rangle$ appears in our data (see Figure 3 and J. Sun et al. 2018, 2020b; E. Rosolowsky et al. 2021). We indicate power laws with the fiducial slopes (Equations (6) and (8)) as blue lines in Figure 6.

As in Figure 4, most of the data lie within ±0.3 dex of the fiducial relationships, though our fit relations again have shallower slopes compared to the expectations for fixed $\epsilon_{\rm ff}^{\rm mol}$, fixed dynamical state clouds: $m = -0.28$ for $\tau_{\rm dep}^{\rm mol} - \langle \Sigma_{\rm mol}^{\rm cloud} \rangle$ (compared to -0.5 expected) and $m = -0.46$ for $\tau_{\rm dep}^{\rm mol} - \langle \sigma_{\rm mol}^{\rm cloud} \rangle$ (compared to -1 expected). Again, we caution that the adopted methodology affects the precise value of the fit slopes.

Our results for the $\tau_{\rm dep}^{\rm mol} - \langle \Sigma_{\rm mol}^{\rm cloud} \rangle$ relationship match limited previous measurements. In M51, A. K. Leroy et al. (2017a) found $\tau_{\rm dep}^{\rm mol} \propto \langle \Sigma_{\rm mol}^{\rm cloud} \rangle^{-0.14}$ (using fixed $\alpha_{\rm CO}$). Adopting the A. D. Bolatto et al. (2013) CO-to-H_2 prescription, similar to what we use here, the J. Sun et al. (2023) fit to the "freefall time regulated star formation" relation yields $\Sigma_{\rm SFR}^{\rm kpc} \propto (\Sigma_{\rm mol}^{\rm kpc} / \langle \tau_{\rm ff}^{\rm cloud} \rangle)^{0.75}$, which implies $\tau_{\rm dep}^{\rm mol} \propto \langle \Sigma_{\rm mol}^{\rm cloud} \rangle^{-0.125}$ to $\tau_{\rm dep}^{\rm mol} \propto \langle \Sigma_{\rm mol}^{\rm cloud} \rangle^{-0.375}$ depending on the precise dependence of $\langle \tau_{\rm ff}^{\rm cloud} \rangle$ on $\Sigma_{\rm mol}^{\rm kpc}$. Our fit value lies intermediate in this regime. They also used the PHANGS–ALMA data set, so this does not represent an independent measurement, but they did use a different selection and fitting methodology.

We emphasize the $\tau_{\rm dep}^{\rm mol}$ versus $\langle \sigma_{\rm mol}^{\rm cloud} \rangle$ anticorrelation as a useful and new way to approach this topic. This anticorrelation is physically expected for fixed $\epsilon_{\rm ff}^{\rm mol}$, fixed dynamical state

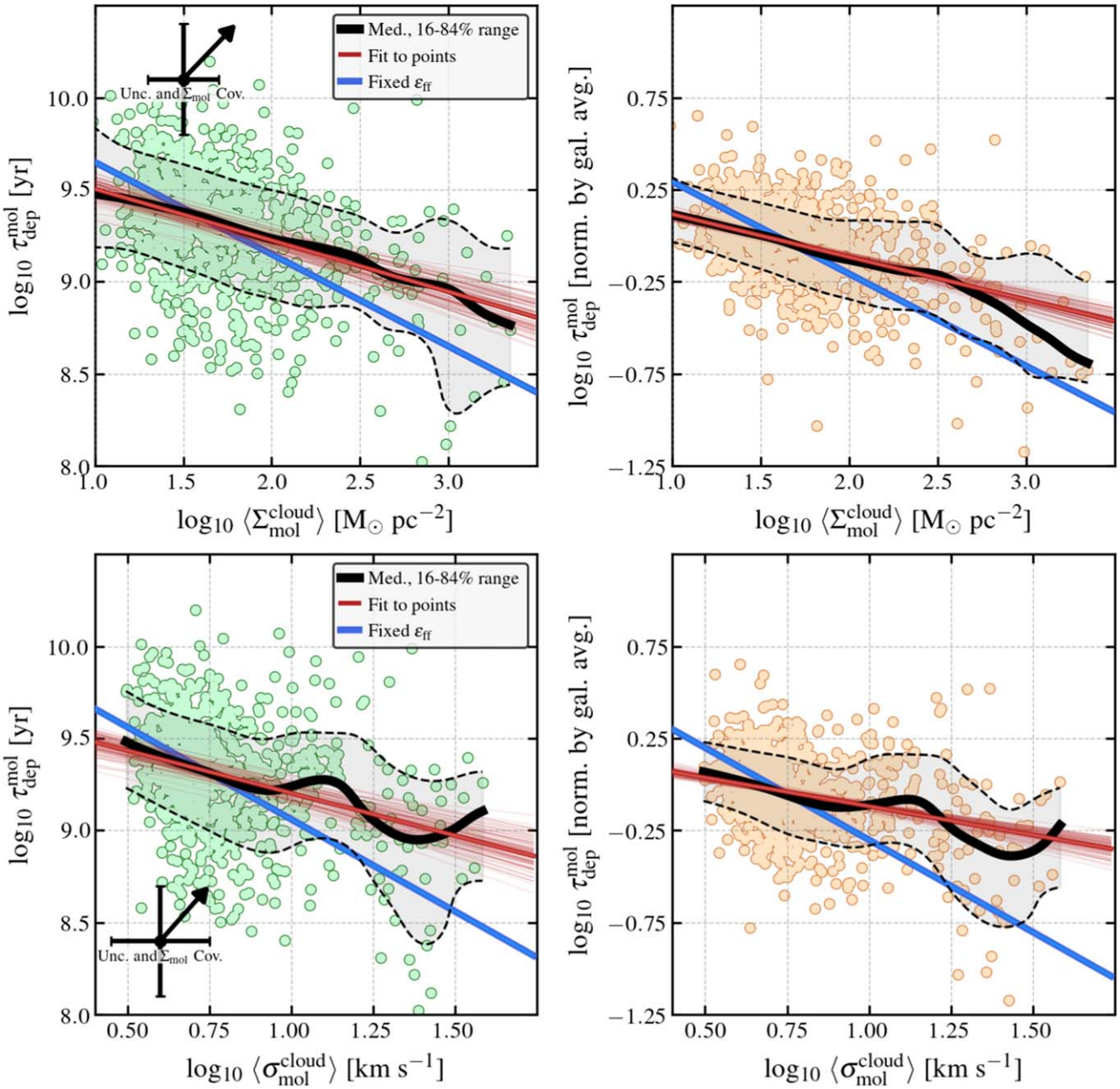

Figure 6. τ_{dep}^{mol} as a function of region-averaged cloud-scale surface density (top panels) and line width (bottom panels). As in Figure 4, the left panels show the measurements of τ_{dep}^{mol}, while in the right panels, measurements are normalized by the galaxy-average τ_{dep}^{mol}, which removes galaxy-to-galaxy scatter in τ_{dep}^{mol}(see Figure 5). Other markings showing the median trend and 16th–84th percentile range, best fit, and expectation for fixed ϵ_{ff}^{mol}, are as in Figure 4. τ_{dep}^{mol} anticorrelates with both $\langle \Sigma_{mol}^{cloud} \rangle$ and $\langle \sigma_{mol}^{cloud} \rangle$(see Table 3), showing a slope shallower than expected for fixed ϵ_{ff}^{mol}. Given the underlying relation among $\langle \Sigma_{mol}^{cloud} \rangle$, $\langle \sigma_{mol}^{cloud} \rangle$, and $\langle \tau_{ff}^{cloud} \rangle$, these and the plots in Figure 4 all express highly related trends. We highlight the $\tau_{dep}^{mol} - \langle \sigma_{mol}^{cloud} \rangle$ relation, shown in the bottom row, because it depends less on α_{CO} and potentially resolution compared to other measurements.

clouds (Equation (8)). This first-order expectation does not involve any turbulence physics, it simply reflects that the gas velocity dispersion traces the underlying gravitational potential of the clouds.

This τ_{dep}^{mol} versus $\langle \sigma_{mol}^{cloud} \rangle$ relationship is particularly intriguing because α_{CO} only affects the vertical axis,[40] so that these plots have less built-in covariance between the axes than most of the other relationships we consider (though see below). Moreover, $\langle \sigma_{mol}^{cloud} \rangle$ may not depend as sensitively on resolution as $\langle \Sigma_{mol}^{cloud} \rangle$. In the limit of an isolated, low-mass, unresolved cloud, ALMA might still measure an accurate CO line width given enough sensitivity, whereas in this situation $\langle \Sigma_{mol}^{cloud} \rangle$ will be strongly affected by beam dilution.

We note that near galaxy centers, the blending of multiple clouds along the line of sight can be a concern, especially at our resolution (E. Rosolowsky et al. 2021, J. Henshaw et al. 2025, in preparation). When estimating the CO line width using moment methods, this can lead the moment-based line width to reflect the inter-cloud dispersion rather than the line width of any individual component (S. M. R. Jeffreson et al. 2022;

[40] However, note that there could be a subtle second-order effect due to variations in α_{CO} within a region, which might affect the weighted averaging scheme.

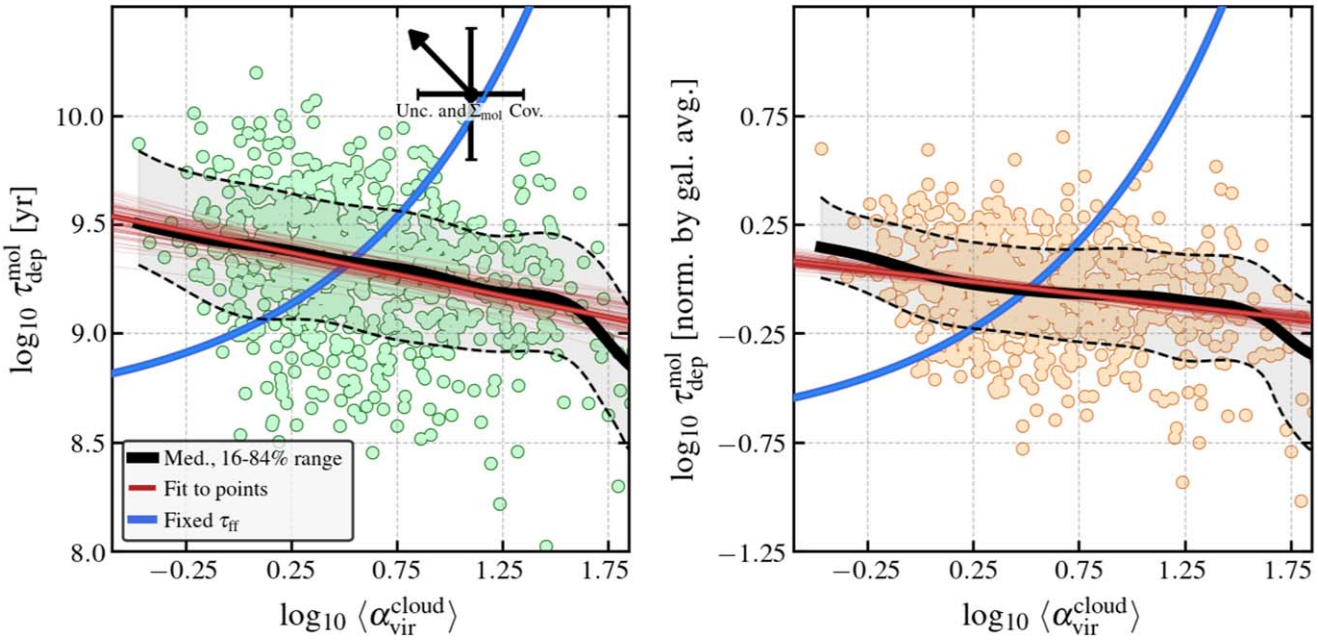

Figure 7. τ_{dep}^{mol} as a function of region-averaged cloud-scale virial parameter, $\langle\alpha_{vir}^{cloud}\rangle$. The contents follow Figures 4 and 6. As in those plots, the left panel shows τ_{dep}^{mol} without any normalization, while in the right panel, measurements are first normalized by the galaxy-average τ_{dep}^{mol}. The blue line here shows expectations for fixed τ_{ff}^{cloud} and varying α_{vir}^{cloud} following P. Padoan et al. (2012). The data show an anticorrelation between τ_{dep}^{mol} and $\langle\alpha_{vir}^{cloud}\rangle$. This has the opposite sense compared to the physical expectation that gas more bound by self-gravity (lower α_{vir}) should form stars more effectively. The anticorrelation likely reflects that gas in high surface density, inner regions of galaxies is significantly affected by the stellar potential.

J. Henshaw et al. 2025, in preparation). Our line-width measurements are not second moments but "effective widths" (M. H. Heyer et al. 2001; A. K. Leroy et al. 2016; J. Sun et al. 2022) derived from the ratio of the line integral to the peak, $\sigma \equiv I_{CO}/\sqrt{2\pi}I_{pk}$. This has less sensitivity to any inter-cloud dispersion but will still be biased high in the case of multivelocity components. It will be interesting to explore how different line-width measures correlate with τ_{dep}^{mol} and are important to match methodology when comparing to our measurements.

3.3. Molecular Gas Depletion Time as a Function of Cloud-scale Virial Parameter

Figure 7 shows τ_{dep}^{mol} as a function of $\langle\alpha_{vir}^{cloud}\rangle$, the region-mean cloud-scale virial parameter. Theoretical models of star formation in turbulent clouds make a clear prediction that, all other things being equal, τ_{dep}^{mol} should correlate with $\langle\alpha_{vir}^{cloud}\rangle$. This reflects that more gravitationally bound gas should form stars more effectively. In Figure 7, the dashed line shows the expected relationship from P. Padoan et al. (2012) for fixed $\langle\tau_{ff}^{cloud}\rangle$; similar predictions would arise from, e.g., M. R. Krumholz & C. F. McKee (2005) or C. Federrath & R. S. Klessen (2012, 2013). Our observations do not show the predicted correlation. In fact, we observe a significant anticorrelation between τ_{dep}^{mol} and $\langle\alpha_{vir}^{cloud}\rangle$, such that gas less bound by self-gravity appears to form stars more efficiently. We find a best-fit slope of $m = -0.29$, though this drops to $m = -0.12$ after we normalize each galaxy by its mean τ_{dep}^{mol}.

Though contradictory at first glance, this observation fits well with our current understanding of gas properties in the context of galaxy structure. We see that short τ_{dep}^{mol} regions often correspond to galaxy centers, which also show high $\langle\alpha_{vir}^{cloud}\rangle$ (J. Sun et al. 2020b, 2022). This high $\langle\alpha_{vir}^{cloud}\rangle$ can be at least partially attributed to the importance of stellar gravity to molecular gas dynamics in the inner parts of galaxies. Observations suggest that the high stellar and gas mass densities lead to high gas pressures in the inner parts of massive galaxies. This pressure then turns the overwhelming bulk of gas molecular (e.g., T. Wong & L. Blitz 2002; L. Blitz & E. Rosolowsky 2006; A. K. Leroy et al. 2008; C. Eibensteiner et al. 2024). This can lead to the emergence of a "diffuse," high-velocity dispersion medium, in which the gas is bound by the larger-scale galactic potential. This large-scale potential is dominated by stellar gravity, not by its own self-gravity. The high stellar densities in the inner regions of galaxies can rival the gas density even within molecular complexes, playing an important role in force balance (e.g., S. E. Meidt et al. 2018; J. Sun et al. 2020a; L. Liu et al. 2021). Moreover, observations suggest that stellar density correlates with molecular gas morphology, additional support to the view that stellar gravity exerts an important dynamical effect (L. Liu et al. 2021; T. A. Davis et al. 2022).

The denser, inner regions of galaxies show high α_{vir} because, following standard practice for molecular cloud studies, our $\langle\alpha_{vir}^{cloud}\rangle$ only accounts for gas self-gravity. In cases where the stellar gravity dominates, $\langle\alpha_{vir}^{cloud}\rangle$ will not capture the true dynamical state of the gas. The expectations mentioned in Sections 1 and 2, including the blue line from P. Padoan et al. (2012) in Figure 7, emerge from theories of turbulent gas-only clouds, and do not typically account for a realistic galactic potential or conditions typical of dense inner galaxies.

Our result has the opposite sense of the trend measured in M51 by A. K. Leroy et al. (2017a), where the expected correlation between τ_{dep}^{mol} and $\langle\alpha_{vir}^{cloud}\rangle$ was present. Our results (that find no overall correlation between ϵ_{ff}^{mol} and $\langle\alpha_{vir}^{cloud}\rangle$ below) do agree with their results in M51 and those of A. Schruba et al. (2019) studying molecular cloud populations

in eight galaxies. M51 may be relatively rare in that the highest $\langle\alpha_{\rm vir}^{\rm cloud}\rangle$ are driven by streaming motions along the spiral arms, which correspond to regions of suppressed star formation (S. E. Meidt et al. 2013). This may represent a distinct physical case from the high $\langle\alpha_{\rm vir}^{\rm cloud}\rangle$ seen in the centers of late type galaxies, which are not generally associated with suppressed star formation. The high $\alpha_{\rm vir}^{\rm cloud}$ found in early-type galaxies, which are associated with suppressed star formation may represent yet a third regime (T. G. Williams et al. 2023; A. Lu et al. 2024)

A related effect where $\langle\alpha_{\rm vir}^{\rm cloud}\rangle$ misses the full picture has been discussed in the context of H I-dominated, low surface density parts of galaxies by J. Sun et al. (2018, 2020b) and A. Schruba et al. (2019), following G. B. Field et al. (2011). There, atomic gas may make significant contributions to the cloud mass, or molecular gas may simply represent the dense subset of a larger turbulent neutral medium. Our selection largely excludes such regions (see Sections 2.3 and 3.4), because PHANGS–ALMA lacks the surface brightness sensitivity to achieve high flux completeness at high resolution in such environments. This represents an area for future investigation, and likely relates to why we find results with the opposite direction from the Milky Way work by N. J. Evans et al. (2022). Their analysis pivots on the behavior of gas at relatively large galactocentric radii and low $\Sigma_{\rm SFR}$ compared to what we study here and, as they discuss, depends sensitively on the metallicity dependence of $\alpha_{\rm CO}$.

3.4. $\tau_{\rm dep}^{\rm mol}$, Gas Properties, and Galactocentric Radius

As a general rule, high $\Sigma_{\rm mol}^{\rm kpc}$ can be found in the inner regions of galaxies, with the highest values at galaxy centers (e.g., J. S. Young & N. Z. Scoville 1991; J. S. Young et al. 1995; M. W. Regan et al. 2001; N. Kuno et al. 2007; M. Querejeta et al. 2021). The same is true for $\Sigma_{\rm mol}^{\rm cloud}$ and $\sigma_{\rm mol}^{\rm cloud}$ (e.g., S. Jogee et al. 2005; J. Sun et al. 2020b, 2022; J. D. Henshaw et al. 2023). Figure 8 shows the cloud-scale gas properties and $\tau_{\rm dep}^{\rm mol}$ as functions of galactocentric radius in our data set.

All of these properties of interest show clear radial trends. The innermost 1.5 kpc hexes show high $\langle\Sigma_{\rm mol}^{\rm cloud}\rangle$, high $\langle\sigma_{\rm mol}^{\rm cloud}\rangle$, high $\langle\alpha_{\rm vir}^{\rm cloud}\rangle$, and low $\tau_{\rm dep}^{\rm mol}$. Even outside the centers, $\langle\Sigma_{\rm mol}^{\rm cloud}\rangle$ and $\langle\sigma_{\rm mol}^{\rm cloud}\rangle$ decline with radius, though the properties vary more weakly outside $\approx$4 kpc. The region-averaged $\langle\alpha_{\rm vir}^{\rm cloud}\rangle$, determined by the ratio of $(\sigma_{\rm mol}^{\rm cloud})^2/\Sigma_{\rm mol}^{\rm cloud}$, shows a strong radial trend, declining with increasing radius out to radius >4 kpc (something already clear in the beamwise analysis of J. Sun et al. 2020b; also see A. Hughes et al. 2025, in preparation). In Sections 3.2 and 3.3, we noted that stellar gravity likely plays an important role in the behavior of $\langle\alpha_{\rm vir}^{\rm cloud}\rangle$. Unresolved streaming or bulk motions may also affect $\langle\alpha_{\rm vir}^{\rm cloud}\rangle$ (S. E. Meidt et al. 2013, 2018), though beam smearing is not expected to exert a large impact at the resolution of PHANGS–ALMA (P. Lang et al. 2020; J. Sun et al. 2020b).

$\tau_{\rm dep}^{\rm mol}$ also shows a radial trend with lower values in galaxy centers. After normalization by the galaxy mean $\tau_{\rm dep}^{\rm mol}$, the strongest effect is lower central $\tau_{\rm dep}^{\rm mol}$ compared to the disk average. This radial trend in normalized $\tau_{\rm dep}^{\rm mol}$, which appears relatively flat with a moderate central depression and large scatter, is consistent with similar measurements for the HERACLES sample by A. K. Leroy et al. (2013) and analysis of the COMING survey by K. Muraoka et al. (2019). The low central $\tau_{\rm dep}^{\rm mol}$ in PHANGS–ALMA has previously been shown by Y.-H. Teng et al. (2024), who also demonstrated that this result depends critically on the treatment of $\alpha_{\rm CO}$ (see also A. K. Leroy et al. 2013; J. S. den Brok et al. 2023). We expand on this in Section 3.5.

The regularity of the trends in Figure 8 reinforce that the cloud-scale gas properties couple to the overall disk structure. Over the last decade, observations have shown that the ∼50–150 pc resolution properties of molecular gas, including $\Sigma_{\rm mol}^{\rm cloud}$ and $P_{\rm int}^{\rm cloud} \propto \Sigma_{\rm mol}\,\sigma_{\rm mol}^2$, correlate with the large-scale properties of the galaxy disk (A. Hughes et al. 2013; A. Schruba et al. 2019; J. Sun et al. 2018; J. Sun et al. 2020a, 2020b, 2022; E. Schinnerer & A. K. Leroy 2024). J. Sun et al. (2022), in particular, provided an extensive series of scaling relations that link cloud-scale gas properties, measured using pixel statistics and cloud-finding methods, to the local kiloparsec-scale conditions in the gas disk (reviewed in E. Schinnerer & A. K. Leroy 2024).

This regularity in the variation of gas properties in disks means that the correlations between $\tau_{\rm dep}^{\rm mol}$ (or $\epsilon_{\rm ff}^{\rm mol}$) and any cloud-scale gas properties almost always have hidden variables related to galactic structure. To show this, Figure 9 shows $\tau_{\rm dep}^{\rm mol}$ as a function of $\langle\tau_{\rm ff}^{\rm cloud}\rangle$ again (as Figure 4), but now coloring the points as a function of galactocentric radius. A clear radial trend is visible in the plot, demonstrating that because of the link between gas properties and ∼kpc scale environment in real galaxies, this plot focused on small-scale conditions in the gas cannot be easily separated from the rest of galactic structure. We return to this in Section 4.3.

Figures 8 and 9 also highlight that the inner regions of galaxies are critical to achieve dynamic range in both $\tau_{\rm dep}^{\rm mol}$ and the cloud-scale gas properties. These are the source of our high $\langle\Sigma_{\rm mol}^{\rm cloud}\rangle$, high $\langle\sigma_{\rm mol}^{\rm cloud}\rangle$, high $\langle\alpha_{\rm vir}^{\rm cloud}\rangle$, low $\langle\tau_{\rm ff}^{\rm cloud}\rangle$, low $\tau_{\rm dep}^{\rm mol}$ points. As noted above, extreme conditions in inner galaxies are well established. In high-mass, barred galaxies, the central regions often represent distinct dynamical environments with high surface and volume densities and deep stellar potential wells (e.g., J. Kormendy & R. C. J. Kennicutt 2004; S. E. Meidt et al. 2018; M. Querejeta et al. 2021; T. A. Davis et al. 2022; E. Schinnerer & A. K. Leroy 2024). These regions also show enhanced CO emissivity (e.g., K. M. Sandstrom et al. 2013; Y.-H. Teng et al. 2022, 2023; J. S. den Brok et al. 2023; I.-D. Chiang et al. 2024), which manifest as variations in $\alpha_{\rm CO}$. The nature of our sampling scheme, in which each region covers equal area in the galaxy disk, means that these key environments are covered by relatively few data points. It is worth keeping the importance of these scarcer low $\tau_{\rm dep}^{\rm mol}$, high $\langle\Sigma_{\rm mol}^{\rm cloud}\rangle$, high $\langle\sigma_{\rm mol}^{\rm cloud}\rangle$ points in mind when examining the plots.

Note that the enhanced densities and shorter $\tau_{\rm dep}^{\rm mol}$ conditions observed in galaxy centers refer to the gas, which is often concentrated into bar-fed central molecular zones. Viewed more broadly, massive galaxies often show depressed specific star formation rates, SFR/$M_\star$, in their inner regions (F. Belfiore et al. 2018; S. L. Ellison et al. 2018). In massive galaxies with bulges, this can reflect the presence of gas-free regions with low $\Sigma_{\rm SFR}$. In follow-up work, H.-A. Pan et al. (2024) suggested a longer $\tau_{\rm dep}^{\rm mol}$ in the central regions of main-sequence galaxies compared to their disks (both L. Lin et al. 2022; H.-A. Pan et al. 2022 and T. A. Davis et al. 2014 also noted longer $\tau_{\rm dep}^{\rm mol}$ in the inner parts of green valley galaxies, but these are not our focus). As discussed in Section 3.5 and Y.-H. Teng et al. (2024) and A. K. Leroy et al. (2013), the treatment of $\alpha_{\rm CO}$ has a

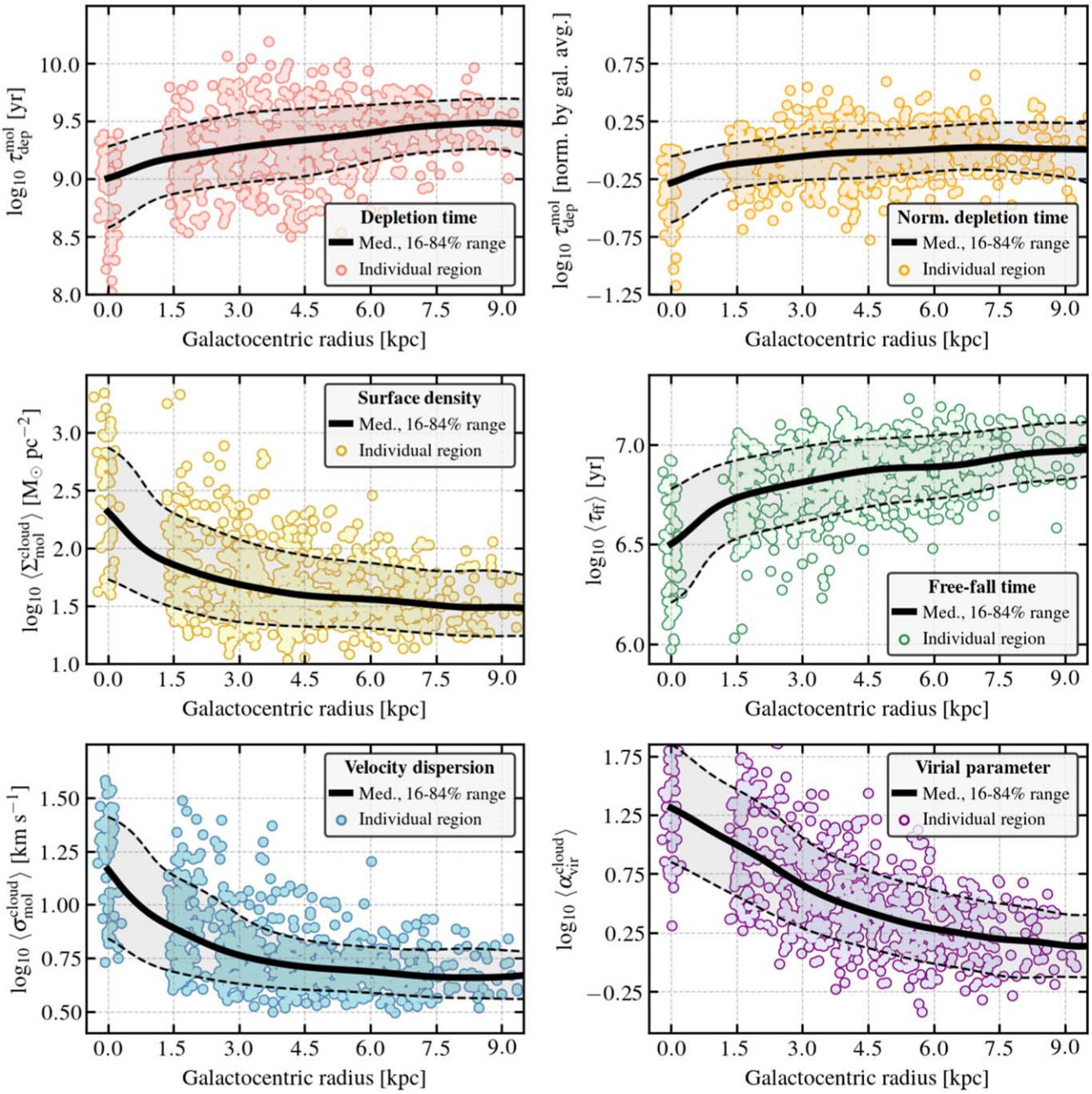

Figure 8. Depletion time and mass-weighted mean gas properties as a function of galactocentric radius. Individual points show measurements and central galactocentric radius for individual 1.5 kpc diameter regions (a small amount of scatter has been added to the galactocentric radius for display purposes). The black lines show the median and 16th–84th percentile range as a function of galactocentric radius. Top-left panel: $\tau_{\rm dep}^{\rm mol}$ appears depressed near galaxy centers and shows a modest radial trend, though this appears weaker in the top-right panel when $\tau_{\rm dep}^{\rm mol}$ is first normalized by the galaxy average. Middle-left panel: the cloud-scale surface density declines as galactocentric radius increases, with the highest values found in galaxy centers and a shallower decline with radius at large radii (consistent with J. Sun et al. 2018, 2020b; E. Rosolowsky et al. 2021; J. Sun et al. 2022). The middle-right panel implies corresponding shorter $\langle \tau_{\rm ff}^{\rm cloud} \rangle$. Bottom-left panel: the cloud-scale line width, $\langle \sigma_{\rm mol}^{\rm cloud} \rangle$, is also highest at galaxy centers and then declines with galactocentric radius. Comparing $\langle \Sigma_{\rm mol}^{\rm cloud} \rangle$ and $\langle \sigma_{\rm mol}^{\rm cloud} \rangle$, the bottom-right panel shows that $\langle \alpha_{\rm vir}^{\rm cloud} \rangle$ is significantly enhanced in galaxy centers and shows a strong gradient as a function of galactocentric radius (see J. Sun et al. 2020b).

large impact on inferred $\tau_{\rm dep}^{\rm mol}$ for galactic centers, and we consider the evidence for low $\alpha_{\rm CO}$ in central molecular zones strong. Still, reconciling these measurements will be an area worth future investigation.

3.5. The Key Role of the CO-to-H_2 Conversion Factor

As described in Section 2, we repeat our analysis using a fixed $\alpha_{\rm CO}$ instead of our best estimate. Figure 10 shows these results for the $\tau_{\rm dep}^{\rm mol} - \langle \tau_{\rm ff}^{\rm cloud} \rangle$ relation, and Table 4 reports results of the correlation analysis between $\tau_{\rm dep}^{\rm mol}$ and all quantities for fixed $\alpha_{\rm CO}$. The fixed $\alpha_{\rm CO}$ leads to a nearly constant $\tau_{\rm dep}^{\rm mol}$, in contrast to the fiducial results with our best estimate $\alpha_{\rm CO}$. This, in turn, leads to almost no correlation or even an anticorrelation between $\tau_{\rm dep}^{\rm mol}$ and $\langle \tau_{\rm ff}^{\rm cloud} \rangle$. Contrasting this with Table 3, all relationships show weaker correlations and slopes closer to 0.0 at fixed $\alpha_{\rm CO}$. Moreover, the actual sense of the correlation changes in most cases. With fixed $\alpha_{\rm CO}$, $\tau_{\rm dep}^{\rm mol}$ appears longer for high $\langle \Sigma_{\rm mol}^{\rm cloud} \rangle$ and high $\langle \sigma_{\rm mol}^{\rm cloud} \rangle$. The

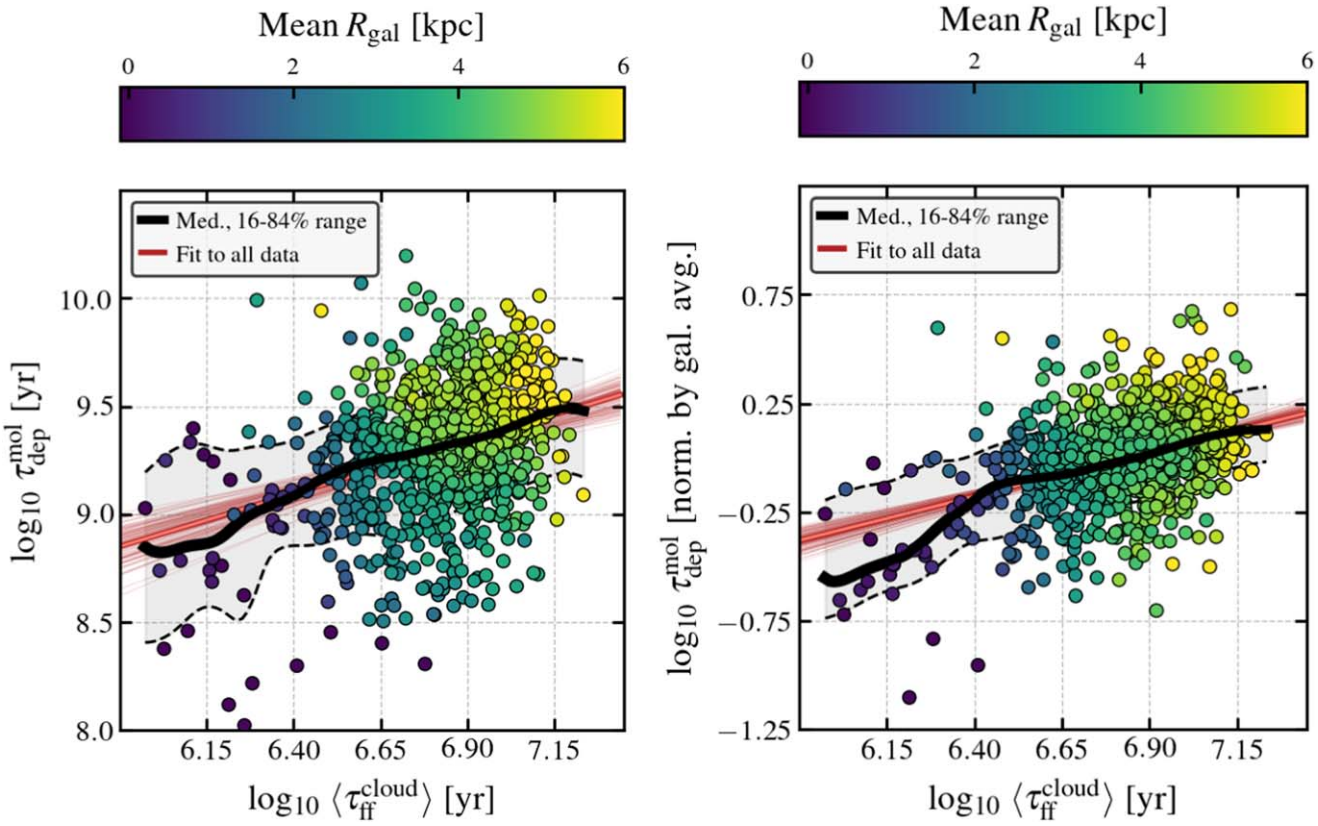

Figure 9. The same as Figure 4 but indicating the galactocentric radius of data. Each point is colored by the local mean radius among data at similar $\langle \tau_{ff}^{cloud} \rangle$ and τ_{dep}^{mol}. Long $\langle \tau_{ff}^{cloud} \rangle$ and long τ_{dep}^{mol} both arise preferentially from regions at high galactocentric radius, while denser gas with short depletion times and gravitational freefall times arises from the central regions. This is particularly clear in the plot with normalized τ_{dep}^{mol} in the right panel. Colors span from galactocentric radius $R_{gal} = 0$–6 kpc.

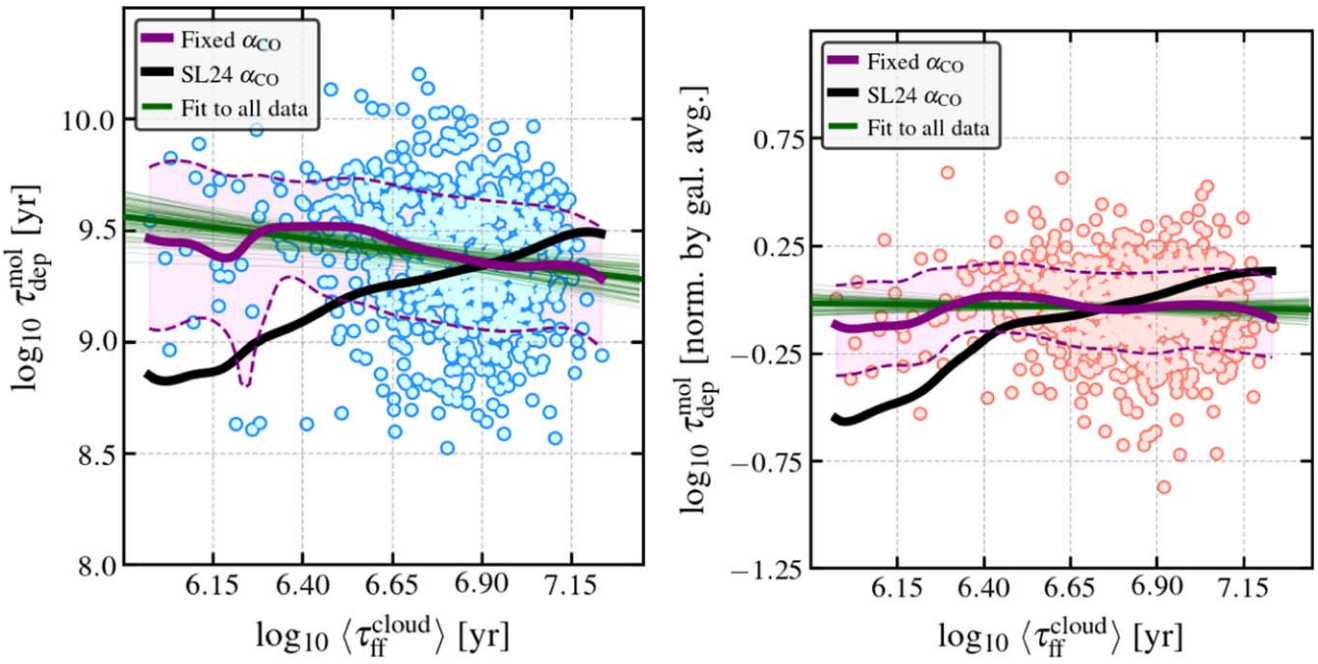

Figure 10. The same as Figure 4 but now showing τ_{dep}^{mol} and $\langle \tau_{ff}^{cloud} \rangle$ calculated assuming a fixed CO-to-H_2 conversion factor, α_{CO}. Similar to Figure 4, the points show individual regions, the purple lines and shaded region show the median and 16th–84th percentile range, and the green line shows the best fit. For comparison, the black line shows the median trend using the variable α_{CO} from Figure 4. Adopting a fixed α_{CO} removes any overall correlation between τ_{dep}^{mol} and $\langle \tau_{ff} \rangle$, and even leads to a slight anticorrelation in the left panel. Note that α_{CO} affects both τ_{dep}^{mol} ($\propto \alpha_{CO}$) and $\langle \tau_{ff}^{cloud} \rangle$ ($\propto \alpha_{CO}^{-0.5}$), but the effect on τ_{dep}^{mol} is stronger.

sense of the $\langle\alpha_{\rm vir}^{\rm cloud}\rangle$ trend also reverses compared to our fiducial case, with higher $\langle\alpha_{\rm vir}^{\rm cloud}\rangle$ corresponding to higher $\tau_{\rm dep}^{\rm mol}$, meaning less efficient star formation. All of these trends are weak, however, especially when considering the $\tau_{\rm dep}^{\rm mol}$ normalized by the galaxy average.

Our fiducial $\alpha_{\rm CO}$ treatment, adopted from E. Schinnerer & A. K. Leroy (2024), accounts for variations in excitation and emissivity (sometimes referred to as the "starburst" term) and metallicity (the "CO-dark" term), similar to A. D. Bolatto et al. (2013). For the present work, the excitation and emissivity variations represent the key terms. In our prescription, $\alpha_{\rm CO}^{1-0} \propto \Sigma_{\star}^{-0.25}$ where $\Sigma_{\star} > 100\,M_{\odot}\,{\rm pc}^{-2}$ (based on I.-D. Chiang et al. 2024), reflecting emissivity variations, and $\alpha_{\rm CO}^{2-1}$ also $\propto\Sigma_{\rm SFR}^{-0.125}$ (based on A. K. Leroy et al. 2022; J. S. den Brok et al. 2021; Y. Yajima et al. 2021; and in good agreement with R. P. Keenan et al. 2025), reflecting excitation variations affecting the CO (2–1)/CO (1–0) line ratio R_{21}. Because our selection focuses on the high surface density parts of galaxies (e.g., Figure 3), these terms together significantly affect the estimated molecular gas mass across our sample. The metallicity term, which is critical to integrated galaxy measurements, has a weaker effect here that primarily affects the galaxy-to-galaxy scatter (e.g., Figure 5).

The impact of $\alpha_{\rm CO}$ on $\tau_{\rm dep}^{\rm mol}$ in galaxy centers has been noted before (A. K. Leroy et al. 2013; J. S. den Brok et al. 2023; Y.-H. Teng et al. 2023). In particular, in PHANGS–ALMA, Y.-H. Teng et al. (2024) showed that accounting for the emissivity terms in $\alpha_{\rm CO}$ lead to much shorter $\tau_{\rm dep}^{\rm mol}$ in galaxy centers, and a much steeper, even multivalued $\Sigma_{\rm SFR} - \Sigma_{\rm mol}$ relationship. J. Sun et al. (2023) showed a similar effect when applying the A. D. Bolatto et al. (2013) $\alpha_{\rm CO}$ prescription (which includes an emissivity term) to PHANGS–ALMA. They showed that including this term steepens the molecular Kennicutt–Schmidt relation from $\Sigma_{\rm SFR} \propto \Sigma_{\rm mol}^{1.0}$ to $\Sigma_{\rm SFR} \propto \Sigma_{\rm mol}^{1.2}$.

It is worth emphasizing the strong evidence for a variable $\alpha_{\rm CO}$, and specifically for emissivity and excitation variations. Both independent dust-based $\alpha_{\rm CO}$ estimates (K. M. Sandstrom et al. 2013; I.-D. Chiang et al. 2024) and multitransition, multispecies spectral line modeling (F. P. Israel 2020; Y.-H. Teng et al. 2022, 2023; R. P. Keenan et al. 2025) agree that the CO emission per unit molecular gas mass is higher in inner galaxies. Similarly, numerous observations agree that high $\Sigma_{\rm SFR}$, inner regions of galaxies show enhanced CO excitation (A. K. Leroy et al. 2009, 2013, 2022; J. S. den Brok et al. 2021, 2023; Y. Yajima et al. 2021). All of this matches physical expectations, and the sense of variations inferred for merging galaxies with similar or even more extreme conditions (see summary in A. D. Bolatto et al. 2013).

3.6. Correlation of $\epsilon_{\rm ff}^{\rm mol}$ with Cloud-scale Gas Properties

We plot our estimated $\epsilon_{\rm ff}^{\rm mol}$ as functions of cloud-scale gas properties in Figures 11 and 12 and report results of our correlation analysis in Table 5. P. Padoan et al. (2012), C. Federrath & R. S. Klessen (2012, 2013), B. Burkhart (2018), and others all made predictions about how $\epsilon_{\rm ff}^{\rm mol}$ should depend on cloud-scale gas properties for star formation in turbulent gas clouds.

Figure 11 and Table 5 show almost no relationship between $\epsilon_{\rm ff}^{\rm mol}$ and either $\langle\Sigma_{\rm mol}^{\rm cloud}\rangle$ or $\langle\sigma_{\rm mol}^{\rm cloud}\rangle$, with rank correlation coefficients and slopes both showing very small values. Put in another way, within any reasonable level of uncertainty, a fixed $\epsilon_{\rm ff}^{\rm mol}$ with ±0.3 dex (Table 5) scatter appears to be a sufficient description of our present data set. As with the $\tau_{\rm dep}^{\rm mol}$ results, this statement depends on our treatment of $\alpha_{\rm CO}$ and data selection, but Figure 11 and Table 5 represent our current best estimates. For reference, the median $\epsilon_{\rm ff}^{\rm mol}$ in Table 5 corresponds to 0.34% of gas formed into stars per freefall time, and we measure ±0.29 dex or a factor of 2 scatter across the sample. This agrees well with earlier work on PHANGS–ALMA by D. Utomo et al. (2018) and J. Sun et al. (2023). Indeed, this is almost, though not exactly, the same measurement made in J. Sun et al. (2023).

The dependence of $\epsilon_{\rm ff}^{\rm mol}$ on $\langle\alpha_{\rm vir}^{\rm cloud}\rangle$ has been of interest in the theoretical works mentioned above. These works predict an anticorrelation, such that high $\langle\alpha_{\rm vir}^{\rm cloud}\rangle$ leads to low $\epsilon_{\rm ff}^{\rm mol}$. Figure 12 shows this relationship for our data set, with the curved dashed line indicating a simple expectation from P. Padoan et al. (2012) for the case of fixed $\langle\tau_{\rm ff}^{\rm cloud}\rangle$. As with $\tau_{\rm dep}^{\rm mol}$ and $\langle\alpha_{\rm vir}^{\rm cloud}\rangle$ (Figure 7), we do not find the predicted theoretical relationship. The data instead appear consistent with a nearly fixed $\epsilon_{\rm ff}^{\rm mol}$ over a relatively wide range of $\langle\alpha_{\rm vir}^{\rm cloud}\rangle$, or perhaps even a mild positive correlation between $\epsilon_{\rm ff}^{\rm mol}$ and $\langle\alpha_{\rm vir}^{\rm cloud}\rangle$. As discussed in Sections 3.3, 3.4, and 4.5, this likely reflects that our measured $\langle\alpha_{\rm vir}^{\rm cloud}\rangle$, which only accounts for gas self-gravity, does not capture the true dynamical state of the gas because it neglects stellar gravity.

Finally, we note that though theoretically convenient, treating $\epsilon_{\rm ff}^{\rm mol}$ as the dependent variable can be problematic from an observational perspective. This leads to correlated axes, with cloud-scale density or a closely related quantity now entering both axes. And the requirement to detect gas at cloud scales to estimate $\tau_{\rm ff}^{\rm mol}$ (required to calculate $\epsilon_{\rm ff}^{\rm mol}$) means any completeness or surface density cuts will introduce selection effects that affect both the x- and y-axes, as opposed to mostly only affecting the x-axes when considering $\tau_{\rm dep}^{\rm mol}$. Given that the same physics will manifest in analyses comparing cloud-scale gas properties to $\tau_{\rm dep}^{\rm mol}$, which already suffer from moderately correlated axes, we recommend those measurements as a cleaner point of comparison.

These correlated axes, along with our fairly narrow dynamic range in cloud properties and selection, explain why the $\tau_{\rm dep}^{\rm mol}$ versus gas property measurements in Table 3 do not trivially transform into the $\epsilon_{\rm ff}^{\rm mol}$ versus gas property measurements in Table 5. That is, we find almost flat $\epsilon_{\rm ff}^{\rm mol}$ versus $\langle\Sigma_{\rm mol}^{\rm cloud}\rangle$ but the slope of the $\tau_{\rm dep}^{\rm mol} - \langle\Sigma_{\rm mol}^{\rm cloud}\rangle$ relation is shallower than the $m = 0.5$ expected for fixed $\epsilon_{\rm ff}^{\rm mol}$ (and similar for $\langle\sigma_{\rm mol}^{\rm cloud}\rangle$). Again, we recommend focusing on the cleanly reproducible $\tau_{\rm dep}^{\rm mol}$ results when comparing to our data (see Appendix A).

4. Discussion

4.1. What This Measurement Is

We present a correlation analysis relating cloud-scale gas properties to the molecular gas depletion time across PHANGS–ALMA. We apply a simple selection criteria and use a reproducible methodology that aggregates high-resolution gas properties using a mass-weighting scheme. This yields measurements that average over large enough areas, such that we expect to sample star-forming clouds in all evolutionary stages and access the time-averaged molecular gas depletion time. PHANGS–ALMA does a good job of sampling the massive end of the $z = 0$ star-forming main sequence (A. K. Leroy et al. 2021), so our measurements should represent a definitive view of region-by-region correlations

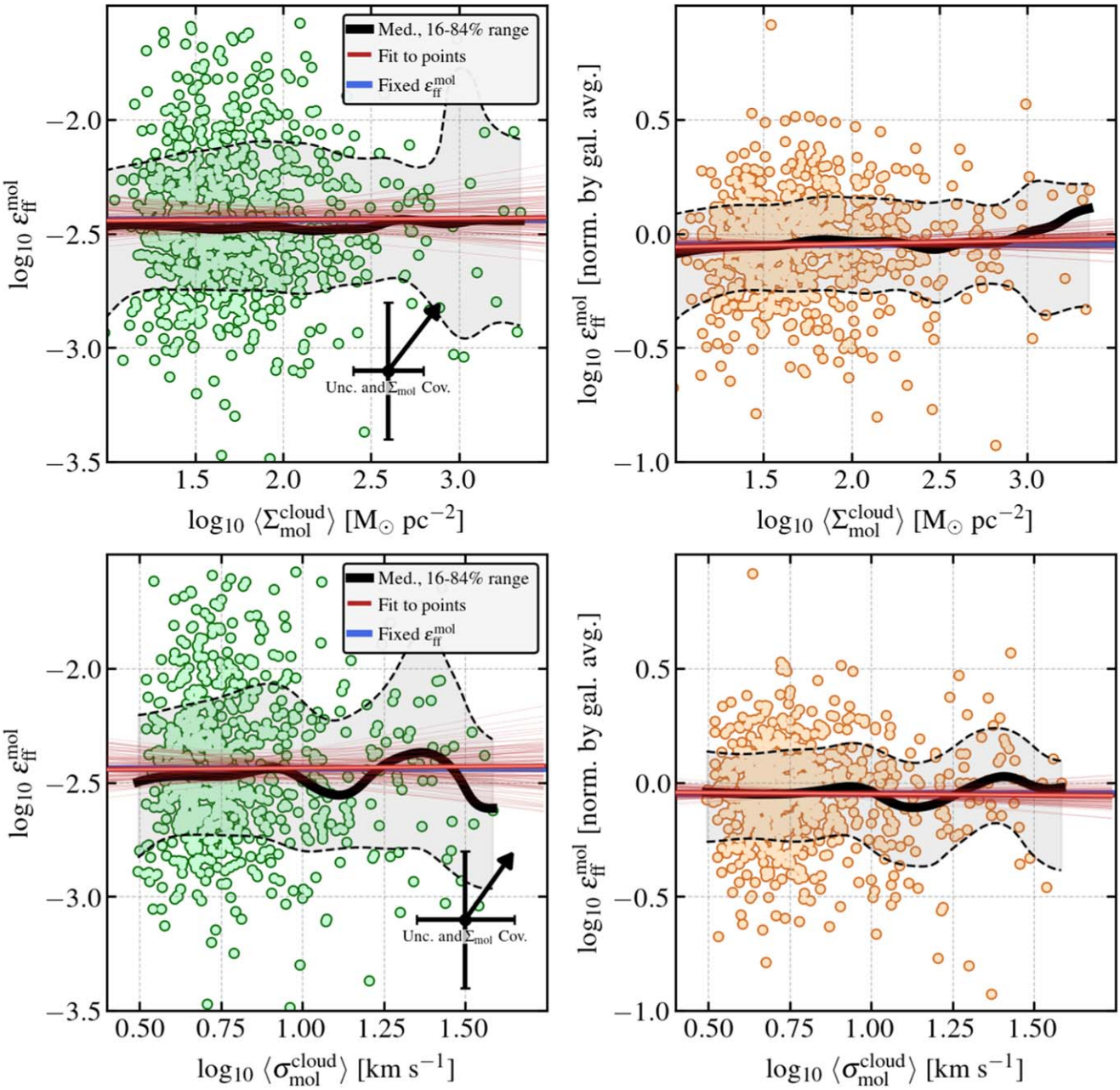

Figure 11. Star formation efficiency per freefall time, ϵ_{ff}^{mol} (Equation (2)), as a function of cloud-scale gas properties, (top row) surface density, $\langle \Sigma_{mol}^{cloud} \rangle$, and (bottom row) line width, $\langle \sigma_{mol}^{cloud} \rangle$. The points and symbols follow Figures 4, 6, and 7. Note that by construction, the axes here are anticorrelated because $\langle \tau_{ff}^{cloud} \rangle$ is derived from $\langle \Sigma_{mol}^{cloud} \rangle$ and is an input to ϵ_{ff}^{mol}. The correlations between ϵ_{ff}^{mol} and cloud-scale gas properties appear weak or absent (Table 5).

between τ_{dep}^{mol} and cloud properties for the molecular gas-dominated regions of $z = 0$ massive star-forming disk galaxies.

We highlight our measurements of τ_{dep}^{mol} as a function of $\langle \Sigma_{mol}^{cloud} \rangle$ and $\langle \sigma_{mol}^{cloud} \rangle$, as these are closest to the empirical data and also capture the key trends. While we provide power-law fits (Tables 3 and 5), we encourage direct comparisons to our full measurement set (Table 2 and Appendix B) as a more robust approach.

These measurements should be easy to reproduce from observations of other samples of galaxies or numerical simulations. It seems useful to apply this method to numerical simulations that track the time evolution and resolve the small-scale structure of the ISM (e.g., K. Grisdale et al. 2018; O. Agertz et al. 2021; F. Renaud et al. 2021; S. M. R. Jeffreson et al. 2022; C.-G. Kim et al. 2023; S. M. R. Jeffreson et al. 2024). On the one hand, our measurements offer a chance to benchmark such simulations against real disk galaxies. On the other hand, the higher physical detail and access to the time dimension and three-dimensional geometry in simulations allow for both a clearer physical interpretation of this type of measurement and the chance to test how different physical prescriptions (e.g., different true ϵ_{ff}^{mol}, dependence on $\langle \alpha_{vir}^{cloud} \rangle$, dependence on other phases or processes like cloud collisions) would manifest (or not) in our measurements.

4.2. What This Measurement Is Not

We do not measure the initial conditions and final outcomes for individual clouds. Our cloud-scale measurements are

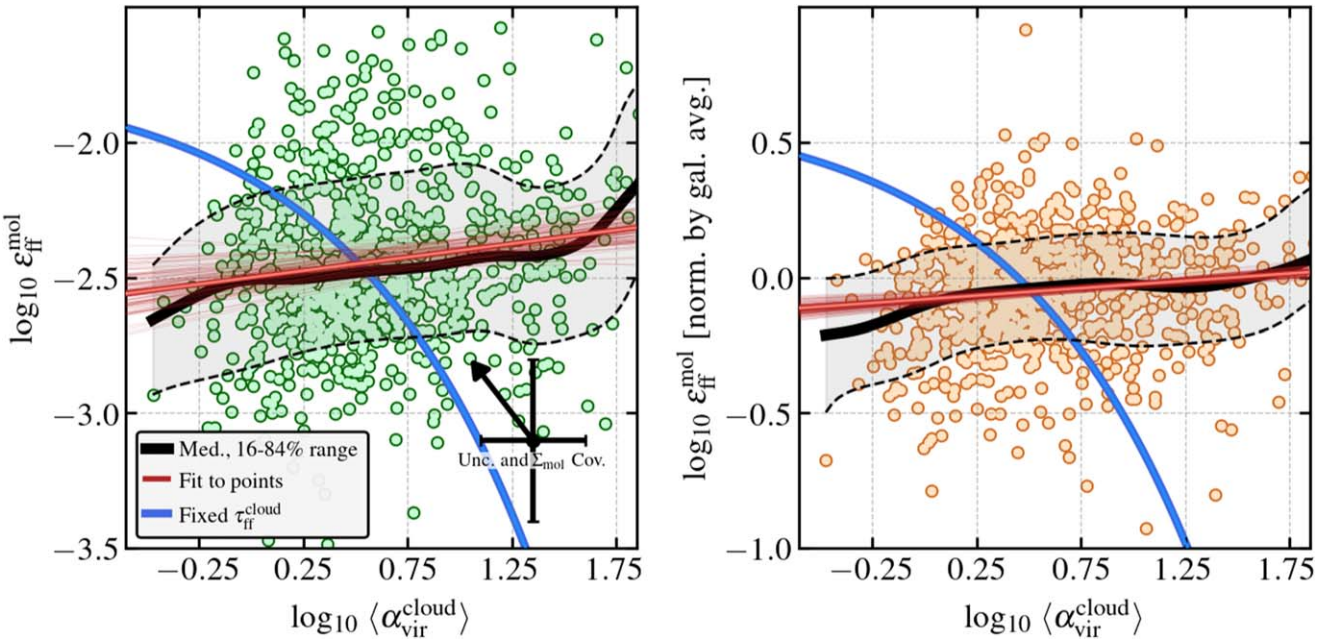

Figure 12. Star formation efficiency per freefall time, $\epsilon_{\rm ff}^{\rm mol}$ (Equation (2)), as a function of region-averaged cloud-scale virial parameter $\langle\alpha_{\rm vir}^{\rm cloud}\rangle$. Points and symbols are the same as in Figures 4, 6, and 7. In both panels, we observe $\epsilon_{\rm ff}^{\rm mol}$ to weakly correlate with $\langle\alpha_{\rm vir}^{\rm cloud}\rangle$, which goes opposite to the theoretical expectation that more bound gas will form stars more effectively (the curved dashed line shows expectations for fixed $\langle\tau_{\rm ff}^{\rm cloud}\rangle$ in a simulation of turbulent gas following P. Padoan et al. 2012). As in Figure 11, the axes are correlated by construction via the dependence of both $\epsilon_{\rm ff}^{\rm mol}$ and $\langle\alpha_{\rm vir}^{\rm cloud}\rangle$ on $\langle\Sigma_{\rm mol}^{\rm cloud}\rangle$. The simplest explanation for the observations is that the observed $\langle\alpha_{\rm vir}^{\rm cloud}\rangle$ reflects motions in the galactic potential rather than probing the fraction of dense, gravitationally bound gas (see S. E. Meidt et al. 2018).

population averages. These aggregate high-resolution measurements from PHANGS–ALMA but do not distinguish between clouds at different evolutionary stages. Most turbulence-regulated theories of star formation consider how the initial properties of clouds affect the mass of gravitationally bound, collapsing gas (M. R. Krumholz & C. F. McKee 2005; P. Padoan et al. 2012; C. Federrath & R. S. Klessen 2012, 2013). Using high-resolution simulations, J.-G. Kim et al. (2021) highlighted that feedback from star formation alters the properties of a clouds, including the $\langle\alpha_{\rm vir}^{\rm cloud}\rangle$. Without accounting for the full cloud life cycle, one should not expect the turbulence-regulated models, or any other model focused on initial conditions, to apply rigorously to our measurements.

Indeed, Á. Segovia Otero et al. (2025) demonstrated, using cosmological simulations of galaxy formation, that the underlying "input" $\epsilon_{\rm ff}^{\rm mol}$ (in their work, the P. Padoan et al. 2012 star formation model was adopted) is challenging to infer observationally. They argued that a mix of cloud evolutionary stages (see also K. Grisdale et al. 2019), as well as the time lag from the onset of star formation to the resulting tracers of star formation, can wash out correlations with parameters such as $\langle\alpha_{\rm vir}^{\rm cloud}\rangle$ (see their Figure 4).

Despite this caveat, we emphasize that our presented relationships, their normalization, and their levels of scatter should still be viewed as benchmarks that numerical simulations should be able to reproduce when our simple methodology is adopted. Additionally, studies of the distribution functions of cloud-scale gas properties in PHANGS, including the gas column distribution function (D. Pathak et al. 2024) and beam-by-beam surface density and velocity dispersion measurements (J. Sun et al. 2018, 2020b), have found relatively narrow (rms ∼0.3–0.4 dex), often lognormal distributions of gas properties in each region. Systematic variations in the mean of these distributions appear mostly correlated with large-scale environment in coherent ways (J. Sun et al. 2022; and see Section 3.4 and Figures 8 and 9 herein). Given this, we expect that region-to-region variations in the mean cloud-scale gas properties do map fairly directly to variations in the initial conditions for star formation. The impact of feedback seems more likely to represent a correction factor than to completely scramble our results. This would be an excellent topic to investigate further with simulations.

4.3. Surface Density, Physical Density, and Resolution

We consider $\langle\Sigma_{\rm mol}^{\rm cloud}\rangle$ an observational indicator of the gas volume density and use it to estimate $\langle\tau_{\rm ff}^{\rm cloud}\rangle$. For a weakly varying molecular gas scale height (which is the case for the Milky Way; M. Heyer & T. M. Dame 2015), $\langle\Sigma_{\rm mol}^{\rm cloud}\rangle$ measures the mean density within the beam. It could be possible that this mean density estimated at 150 pc scales does not indicate the physical density within clouds or the density measured at smaller scales. For example, this could be the case if the molecular ISM consists of otherwise identical small clouds that vary in space density across galaxies (a weak version of this "universal cloud" view has been popular; e.g., L. Blitz et al. 2007; Y. Fukui & A. Kawamura 2010).

Though our common resolution is 150 pc, PHANGS–ALMA also represents the largest 120, 90, and 60 pc resolution survey of CO emission from nearby galaxies. In Appendix B, we repeat the analysis comparing $\tau_{\rm dep}^{\rm mol}$ to $\langle\Sigma_{\rm mol}^{\rm cloud}\rangle$ and $\langle\sigma_{\rm mol}^{\rm cloud}\rangle$ at each of these higher resolutions. Though the numbers of galaxies covered are smaller for these sharper resolutions, they show trends that are consistent with those we observe at 150 pc resolution data (Appendix B).

Figure 13 and Table 6 directly compare $\langle\Sigma_{\rm mol}^{\rm cloud}\rangle$ measured at different resolutions in our target regions. The figure shows that

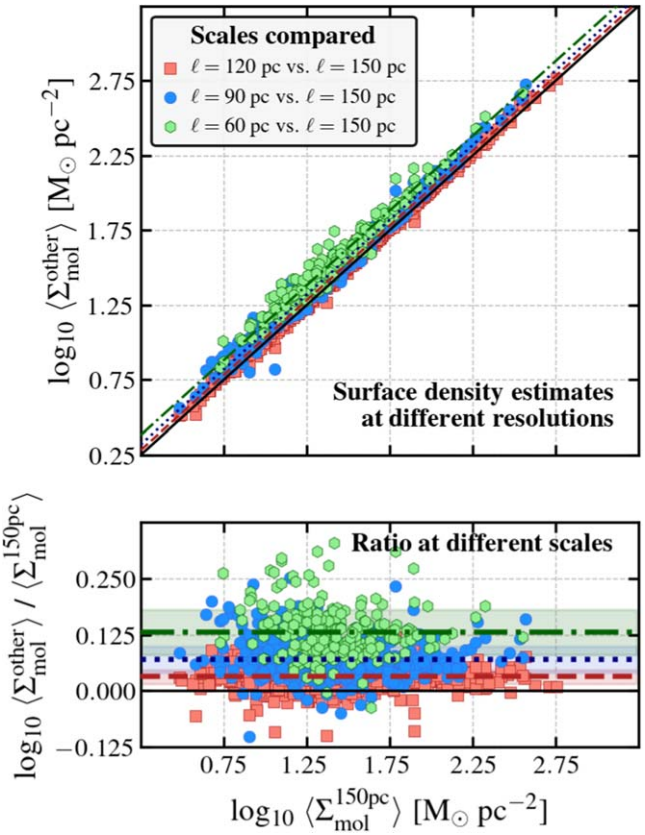

Figure 13. Surface density measured at $\ell = 120$, 90, and 60 pc resolution compared to our fiducial $\ell = 150$ pc resolution (see also Table 6). Mass-weighted region-averaged surface densities measured at all four resolutions correlate with one another extremely well, showing high correlation coefficients and little scatter among the ratio of $\langle \Sigma_{\rm mol}^{\rm cloud} \rangle$ measured at different scales. As expected, high-resolution measurements yield modestly higher surface densities, indicating the presence of beam dilution. But overall, the comparison shows no evidence for a preferred scale, and supports that our $\ell = 150$ pc measurements are reasonable indicators of the physical density. Appendix B also shows that the $\tau_{\rm dep}^{\rm mol}$ vs. gas properties trends observed at high resolution match our fiducial results.

the physical resolution has a mild effect on the mass-weighted surface densities, with slightly higher $\langle \Sigma_{\rm mol}^{\rm cloud} \rangle$ at higher resolution. This indicates some beam dilution or clumping, which is expected. Beyond the ratio, $\langle \Sigma_{\rm mol}^{\rm cloud} \rangle$ at 150 pc correlates stunningly well with $\langle \Sigma_{\rm mol}^{\rm cloud} \rangle$ at 120 pc, 90 pc, and even 60 pc resolution. Although many millimeter astronomers hold strongly felt opinions about the true size of a molecular cloud, as far as we are aware, there is no clear evidence for a specific scale where the surface density traces physical density. Instead, our $\ell = 150$ pc data provide an outstanding predictor of the $\ell = 60$ pc $\langle \Sigma_{\rm mol}^{\rm cloud} \rangle$ despite 6× difference in beam area. This is in good agreement with previous work examining the scale dependence of $\Sigma_{\rm mol}$ by A. K. Leroy et al. (2016), J. Sun et al. (2018), and J. Sun et al. (2020b).

An important line of evidence reinforcing this view comes from millimeter-wave spectroscopic tracers of physical density. M. J. Gallagher et al. (2018), L. Neumann et al. (2023), and A. Garcìa-Rodrìguez et al. (2023) showed that the HCN/CO ratio measured at ∼ kpc scales correlates with $\langle \Sigma_{\rm mol}^{\rm cloud} \rangle$ (see also M. Tafalla et al. 2023). Though the precise density of gas traced by HCN emission is debated, the HCN/CO ratio should be sensitive to physical density (M. R. Krumholz & T. A. Thompson 2007; A. K. Leroy et al. 2017b), and represents one of the most accessible density-sensitive millimeter-wave line ratios. Reinforcing this view, M. J. Jiménez-Donaire et al. (2023) and S. K. Stuber et al. (2023) both showed that HCN/CO correlates well with the N_2H^+/CO line ratio, which is widely considered a gold standard tracer of the dense gas fraction in Milky Way studies. We refer the reader to E. Schinnerer & A. K. Leroy (2024) for more discussion.

Table 6
$\langle \Sigma_{\rm mol}^{\rm cloud} \rangle$ and Resolution

Comparison (versus $\ell = 150$ pc)	Rank. Corr.	Med. $\log_{10}$ Ratio (dex)	Scatter (dex)
$\ell = 120$ pc	0.998	0.031	0.016
$\ell = 90$ pc	0.99	0.069	0.029
$\ell = 60$ pc	0.97	0.13	0.050

Note. Correlation between $\langle \Sigma_{\rm mol}^{\rm cloud} \rangle$ measured at our fiducial scale, $\ell = 150$ pc resolution (treated as the x-variable), and measurements using higher-resolution CO (2–1) data (treated as the y-variable) for regions that meet our selection criteria (Figure 2) Columns report: the nonparameteric rank correlation coefficient between $\langle \Sigma_{\rm mol}^{\rm cloud} \rangle$ at the two scales; the median $\log_{10} y/x$ ratio, which captures the amount of beam dilution present; and the scatter in the $\log_{10}$ ratio. See also Figure 13.

Together, the consistency of $\langle \Sigma_{\rm mol}^{\rm cloud} \rangle$-based results across scale and the link between spectroscopic and imaging-based tracers of density give us confidence that $\langle \Sigma_{\rm mol}^{\rm cloud} \rangle$ does trace the physical gas density distribution in the beam. The fidelity of the tracer and the correct sub-beam geometry to assume certainly need more study, and these represent important areas for follow-up work at higher resolution and simulation-based tests.

We also re-emphasize the point made in Section 3.4. As demonstrated in J. Sun et al. (2022), the cloud-scale gas properties vary in a regular way as a function of $\Sigma_{\rm mol}^{\rm kpc}$, $\Sigma_{\rm SFR}^{\rm kpc}$, the rotation curve, and more. Here we observe relationships between $\tau_{\rm dep}^{\rm mol}$, $\langle \Sigma_{\rm mol}^{\rm cloud} \rangle$, $\langle \sigma_{\rm mol}^{\rm cloud} \rangle$, and $\langle \alpha_{\rm vir}^{\rm cloud} \rangle$, which all then correlate with one another and with these larger-scale conditions. Purely from a data perspective, there is high covariance between these and many other relevant quantities (stellar surface density, the dynamical equilibrium pressure, etc.). $\tau_{\rm dep}^{\rm mol}$ should depend on the small-scale gas properties, so we expect that the causal relationship likely flows (at least partially) from small to large scales. But a host of hidden variables lurk behind all of these plots.

This also means that as $\Sigma_{\rm mol}^{\rm kpc}$, galactocentric radius, or even global galaxy properties vary, these cloud-scale gas properties will also vary. To illustrate this in a parameter space of broad interest, Figure 14 shows the $\Sigma_{\rm SFR}^{\rm mol} - \Sigma_{\rm mol}^{\rm kpc}$ molecular Kennicutt–Schmidt relation for our target regions (as Figure 3) but now coloring by the cloud-scale gas properties. These vary in regular ways across this space, particularly as a function of $\Sigma_{\rm mol}^{\rm kpc}$.

4.4. The $\tau_{\rm dep}^{\rm mol}$–$\langle \sigma_{\rm mol}^{\rm cloud} \rangle$ Anticorrelation

The anticorrelation between $\tau_{\rm dep}^{\rm mol}$ and $\langle \sigma_{\rm mol}^{\rm cloud} \rangle$ mirrors the one relating $\tau_{\rm dep}^{\rm mol}$ to $\langle \Sigma_{\rm mol}^{\rm cloud} \rangle$. As discussed in Section 3.2, this anticorrelation would be expected if (1) there is an underlying anticorrelation between density and $\tau_{\rm dep}^{\rm mol}$ and (2) clouds show

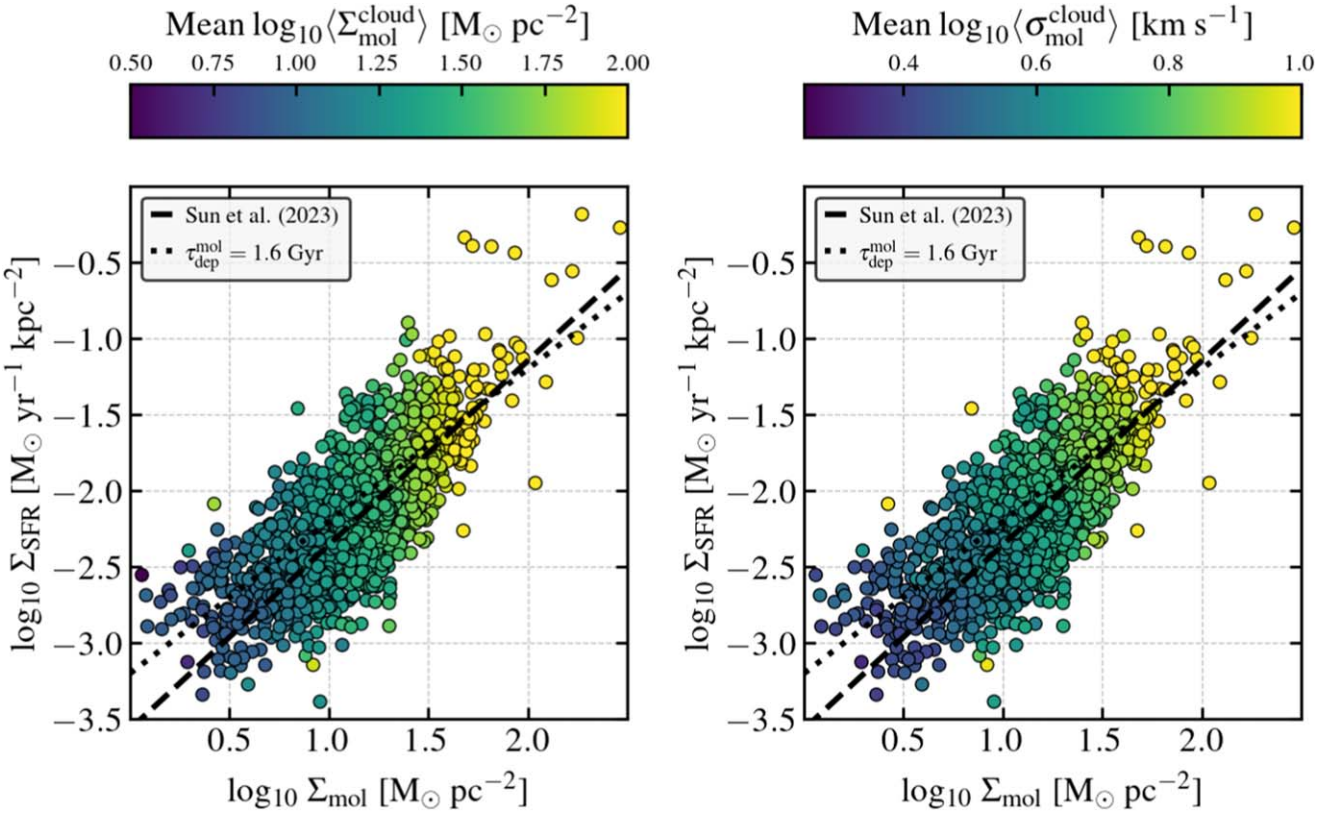

Figure 14. The molecular Kennicutt–Schmidt relation from Figure 3 showing only points used in the analysis. Here we color each point by the mean $\langle\Sigma_{\rm mol}^{\rm cloud}\rangle$ (left panel) or $\langle\sigma_{\rm mol}^{\rm cloud}\rangle$ (right panel) of all points within ±0.1 dex. The cloud-scale gas properties change in regular ways across $\Sigma_{\rm SFR}^{\rm kpc}$ − $\Sigma_{\rm mol}^{\rm kpc}$ space.

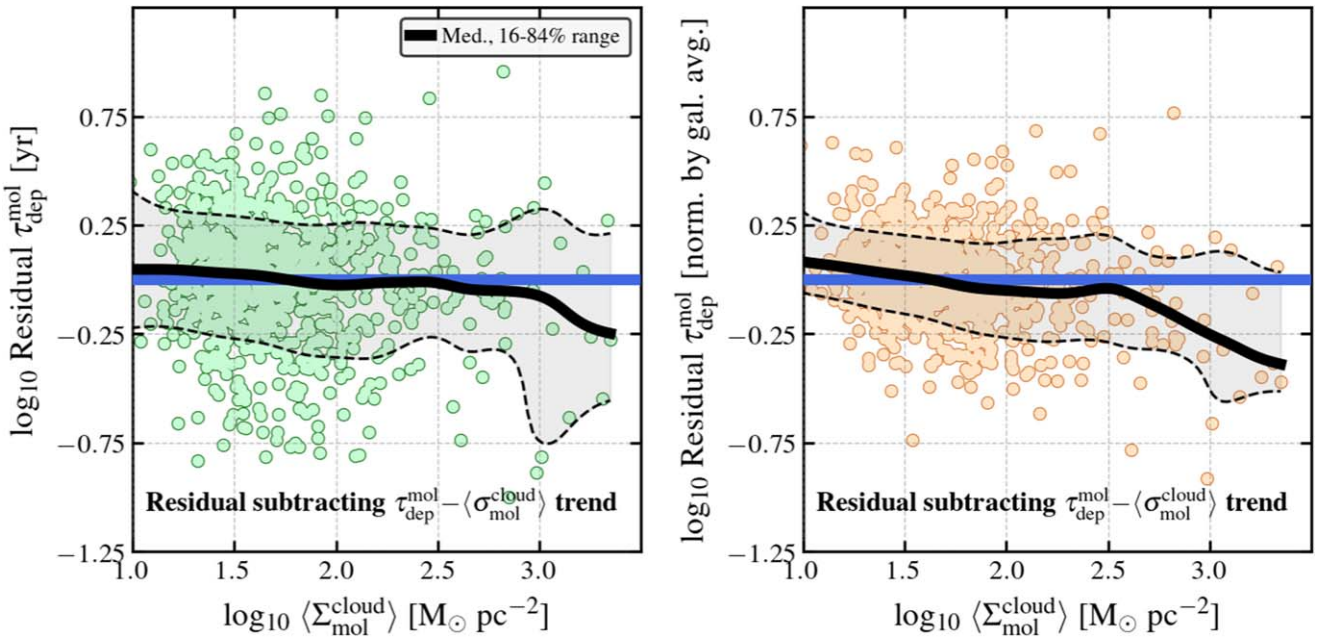

Figure 15. Residual molecular gas depletion time, $\tau_{\rm dep}^{\rm mol}$, as a function of cloud-scale surface density, $\langle\Sigma_{\rm mol}^{\rm cloud}\rangle$. We calculate the residual by first predicting $\tau_{\rm dep}^{\rm mol}$ from $\langle\sigma_{\rm mol}^{\rm cloud}\rangle$. Subtracting (in log space) the trend fit based on line width substantially removes any systematic trend from $\tau_{\rm dep}^{\rm mol}$ as a function of surface density. The blue lines indicate a residual of 0, i.e., no trend. This would be expected if the $\tau_{\rm dep}^{\rm mol}$ vs. $\langle\sigma_{\rm mol}^{\rm cloud}\rangle$ trend expresses the same trend seen for $\tau_{\rm dep}^{\rm mol}$ vs. $\langle\Sigma_{\rm mol}^{\rm cloud}\rangle$.

approximately fixed dynamical state. In that case, the line width reflects the potential and, thus, the density of the molecular gas. Then, the $\tau_{\rm dep}^{\rm mol}$–$\langle\Sigma_{\rm mol}^{\rm cloud}\rangle$ and $\tau_{\rm dep}^{\rm mol}$–$\langle\sigma_{\rm mol}^{\rm cloud}\rangle$ relations are manifestations of the same underlying physical correlation. To test this view, Figure 15 shows the residual $\tau_{\rm dep}^{\rm mol}$ model as a function of $\langle\Sigma_{\rm mol}^{\rm cloud}\rangle$ after subtracting our best-fit $\tau_{\rm dep}^{\rm mol}$–$\langle\sigma_{\rm mol}^{\rm cloud}\rangle$ relation (Table 3). Except at the very highest $\langle\Sigma_{\rm mol}^{\rm cloud}\rangle$, most of the $\tau_{\rm dep}^{\rm mol}$–$\langle\Sigma_{\rm mol}^{\rm cloud}\rangle$ trend is removed by subtracting the $\tau_{\rm dep}^{\rm mol}$–$\langle\sigma_{\rm mol}^{\rm cloud}\rangle$ trend.

This $\tau_{\rm dep}^{\rm mol}$–$\langle\sigma_{\rm mol}^{\rm cloud}\rangle$ relation is worth more investigation. $\langle\sigma_{\rm mol}^{\rm cloud}\rangle$ has only a weak dependence on $\alpha_{\rm CO}$ (via the weighted average) and may depend less sensitively on resolution than $\langle\Sigma_{\rm mol}^{\rm cloud}\rangle$. The line-width measurement certainly has its own complexities, however. As shown by J. Henshaw et al. (2025, in preparation) studying PHANGS–ALMA, the inner parts of galaxies, which show low $\tau_{\rm dep}^{\rm mol}$ also tend to show complex spectral profiles. Our line-width measurement (effective width) is sensitive to the integrated width of all components, and it will be interesting to explore whether other methods (e.g., second moment, Gaussian model fit) show more or less anticorrelation with $\tau_{\rm dep}^{\rm mol}$. Extending the analysis to well-resolved interacting galaxies, which also tend to show significant spectral complexity (e.g., N. Brunetti et al. 2021, 2024) will provide another interesting counterpoint. Because the gas velocity dispersion may be sensitive to physical conditions even in small, unresolved clouds, this also might offer an interesting direction to study the fainter, smaller clouds in outer galaxy disks.

We have emphasized that the $\langle\sigma_{\rm mol}^{\rm cloud}\rangle$ should trace the gravitational potential and produce the sort of anticorrelation that we see, but the velocity dispersion is often physically interpreted in other ways that may be related to star formation. In the context of turbulence-regulated star formation, the velocity dispersion is often related to the Mach number, which plays an important role in setting the density distribution (P. Padoan & Å. Nordlund 2002; M. R. Krumholz & C. F. McKee 2005; C. Federrath & R. S. Klessen 2012, 2013). A variety of bulk motions that should influence the line width have also been invoked to explain enhanced or suppressed star formation efficiencies. These include suppression by streaming motions along spiral arms or bars (e.g., S. E. Meidt et al. 2013), star formation induced by cloud collisions (e.g., Y. Fukui et al. 2021), and star formation induced by spiral shocks (see extensive discussion in M. Querejeta et al. 2024).

Perhaps most importantly, Y.-H. Teng et al. (2024) showed that the observed CO line width also anticorrelates with $\alpha_{\rm CO}$. They use the I.-D. Chiang et al. (2024) $\alpha_{\rm CO}$ estimates, which also underpin the emissivity term in the $\alpha_{\rm CO}$ prescription that we use here. Y.-H. Teng et al. (2024) argued that the line width serves as a proxy for the inverse of the opacity, and that opacity variations drive a large fraction of the $\alpha_{\rm CO}$ emissivity variations. This agrees well with the spectral line modeling of Y.-H. Teng et al. (2022), Y.-H. Teng et al. (2023), and J. den Brok et al. (2025). Since the $\tau_{\rm dep}^{\rm mol}$ variations that we observe depend on our adopted $\alpha_{\rm CO}$ (Section 3.5, Figure 10), our measured $\tau_{\rm dep}^{\rm mol} - \langle\sigma_{\rm mol}^{\rm cloud}\rangle$ correlation is formally related to the $\alpha_{\rm CO} - \langle\sigma_{\rm mol}^{\rm cloud}\rangle$ correlation of Y.-H. Teng et al. (2024). It is entirely possible that the line width both traces the gas density (or another physical parameter related to the depletion) *and* drives variations in $\alpha_{\rm CO}$. But at a minimum, the results of Y.-H. Teng et al. (2024) are important to bear in mind because they imply a hidden correlation between the $\tau_{\rm dep}^{\rm mol}$ and $\langle\sigma_{\rm mol}^{\rm cloud}\rangle$ axes.

4.5. The Lack of a $\tau_{\rm dep}^{\rm mol}$–$\langle\alpha_{\rm vir}^{\rm cloud}\rangle$ Correlation

Our results disfavor the interpretation that $\langle\alpha_{\rm vir}^{\rm cloud}\rangle$, considering only self-gravity and measured at 60–150 pc scales, indicates the amount of self-gravitating, likely star-forming gas. Instead, the regions that show low $\tau_{\rm dep}^{\rm mol}$ also show high $\langle\alpha_{\rm vir}^{\rm cloud}\rangle$ and tend to occur in the inner parts of galaxies. This agrees with recent results arguing that the broader galactic potential, including significant contribution from stellar gravity, can contribute to the dynamical state of molecular clouds (S. E. Meidt et al. 2018; L. Liu et al. 2021).

In numerical modeling, V. A. Semenov et al. (2017, 2018, 2021) found that accounting for the dynamical state of individual parcels of gas is key to reproduce observed $\tau_{\rm dep}^{\rm mol}$ and the decorrelation observed between CO and Hα at high resolution. N. J. Evans et al. (2022) made a similar argument for Milky Way clouds. It is tempting to ask whether $\langle\alpha_{\rm vir}^{\rm cloud}\rangle$ can be salvaged by a more sophisticated formulation that includes information, e.g., on the stellar distribution, rotation curve, or other gas phases. L. Liu et al. (2021) argued that modeling the large-scale potential, combined with high-resolution ($\lesssim$10 pc) CO imaging may offer a chance to assess the dynamical state on scales that better access the presence of self-gravitating gas. Similarly, S. E. Meidt et al. (2018) argued that extragalactic velocity dispersion measurements can be explained by models that includes the full galactic potential. A. Schruba et al. (2019) made a similar argument. This may offer a way forward, but lies beyond the scope of this work.

We also note that the $\tau_{\rm dep}^{\rm mol} - \langle\alpha_{\rm vir}^{\rm cloud}\rangle$ trend almost disappears when the $\tau_{\rm dep}^{\rm mol} - \langle\sigma_{\rm mol}^{\rm cloud}\rangle$ or $\tau_{\rm dep}^{\rm mol} - \langle\Sigma_{\rm mol}^{\rm cloud}\rangle$ trends are subtracted from the data, similar to Figure 15. Given this, an explanation or simulation that matches the other two observed trends will likely capture the impact of dynamical state.

4.6. Next Steps

As we emphasized above, we consider comparison to numerical simulation a critical next step. PHANGS–ALMA has now measured cloud-scale gas properties across the local galaxy population and found regular patterns and links to $\tau_{\rm dep}^{\rm mol}$. We have adopted a deliberately simple methodology and tracked completeness, resolution, and other elements needed to make a fair comparison. An ideal next step will be to see how well numerical simulations match the basic distributions in J. Sun et al. (2018, 2020b; and soon new dust-based results; e.g., D. Pathak et al. 2024), the correlations with environment in J. Sun et al. (2022), and the link to $\tau_{\rm dep}^{\rm mol}$ seen here. C. L. Dobbs et al. (2019) showed promising results in this direction, finding an excellent match between the cloud-scale gas properties that were measured their dwarf spiral simulation and the observations of M33 in J. Sun et al. (2018). We are eager to see future works comparing more simulations with more representative observational results.

From an observational perspective, ALMA is capable of pushing similar analysis down to $\lesssim$10 pc resolution over whole galaxies, but this will require a significant commitment. Still, this seems like the qualitative leap in resolution needed to address any ambiguity in the interpretation of $\langle\sigma_{\rm mol}^{\rm cloud}\rangle$ and $\langle\alpha_{\rm vir}^{\rm cloud}\rangle$. Figure 13 and Appendix B suggest that simply increasing the resolution to $\ell \approx 60$ pc is unlikely to yield qualitatively different results. Meanwhile, improving the star formation rate tracer also represents an important next step. We use the best available option for all of PHANGs–ALMA, which is a combination of Hα and mid-IR data following F. Belfiore et al. (2023). But this limits the scales over which we can measure $\tau_{\rm dep}^{\rm mol}$ and still does not match the quality of an IFU-based Hα+Hβ estimate (F. Belfiore et al. 2023). Coverage of the full sample, e.g., by VLT/MUSE would reduce a lingering source of uncertainty and allow us to average the data in much

finer ways, e.g., by constructing averages along likely gas flow lines (e.g., S. E. Meidt et al. 2015; J. Koda 2021) in more sharply defined distinct dynamical environments (M. Querejeta et al. 2021, 2024), and so on. They would also allow us to examine statistical distributions of matched resolution SFR and gas tracers rather than relying on region averages for $\tau_{\rm dep}^{\rm mol}$.

Finally, improved knowledge of $\alpha_{\rm CO}$ remains the single largest uncertainty. The field has made excellent observational and theoretical progress in this area, improving PDR models, building simulations with realistic chemistry and radiative transfer, and constraining line ratio variations, opacity, and expanding estimates based on independent gas tracers, like dust. But the uncertainty on $\alpha_{\rm CO}$ in any given environment still dominates the error budget for this entire field.

5. Summary

Using PHANGS–ALMA, we have measured how the molecular gas depletion time, $\tau_{\rm dep}^{\rm mol}$, and the star formation efficiency per freefall time, $\epsilon_{\rm ff}^{\rm mol}$, correlate with cloud-scale gas properties. Following J. Sun et al. (2022), we break galaxies into 1.5 kpc diameter hexagonal regions, calculate the region-mean $\tau_{\rm dep}^{\rm mol}$ and $\epsilon_{\rm ff}^{\rm mol}$, and compare these to the mass-weighted mean molecular gas surface density ($\langle\Sigma_{\rm mol}^{\rm cloud}\rangle$), velocity dispersion ($\langle\sigma_{\rm mol}^{\rm cloud}\rangle$), gravitational freefall time ($\langle\tau_{\rm ff}^{\rm cloud}\rangle$), and virial parameter ($\langle\alpha_{\rm vir}^{\rm cloud}\rangle$; see Table 1). We measure 150 pc cloud-scale gas properties, $\tau_{\rm dep}^{\rm mol}$ and $\epsilon_{\rm ff}^{\rm mol}$ for 841 independent regions in 67 galaxies. In Appendix B we also construct higher-resolution data sets where we measure the gas properties at 120, 90, and 60 pc resolution. We find substantially similar results varying the resolution, and emphasize that spectroscopic results also indicate that the 150 pc surface density tracks physical density variations across galaxies (Section 4.3).

In constructing these measurements, the completeness of the CO data entering the gas property analysis represents an important consideration. We work only with regions where >50% of the CO flux is captured by the high-resolution CO map. For PHANGS–ALMA, this corresponds approximately to regions with $\langle\Sigma_{\rm mol}^{\rm cloud}\rangle > 20\ M_{\odot}\ {\rm pc}^{-2}$ (Figure 2). This selection yields a set of regions that show good dynamic range in large-scale $\Sigma_{\rm mol}^{\rm kpc}$, $\Sigma_{\rm SFR}^{\rm kpc}$, and cloud-scale gas properties (Figure 3). As expected, these regions obey the same large-scale $\Sigma_{\rm SFR} - \Sigma_{\rm mol}$ (molecular "Kennicutt–Schmidt") and cloud-scale $\langle\sigma_{\rm mol}^{\rm cloud}\rangle - \langle\Sigma_{\rm mol}^{\rm cloud}\rangle$ ("Heyer–Keto") scalings measured for the overall PHANGS–ALMA data set (J. Sun et al. 2020b, 2022, 2023).

Analyzing these data, we reach the following main conclusions:

1. We observe a positive correlation between $\tau_{\rm dep}^{\rm mol}$ and τff (Section 3.1, Figure 4, Table 3) as expected if density plays an important role in setting the rate at which gas forms stars. This correlation appears stronger after accounting for galaxy-to-galaxy variations in $\tau_{\rm dep}^{\rm mol}$ (Figures 4 and 5). Our best-fit line is shallower than the $\tau_{\rm dep}^{\rm mol} \propto \langle\tau_{\rm ff}^{\rm cloud}\rangle$ relation expected for a fixed efficiency per freefall time, though we emphasize that the fit parameters depend on the adopted methodology. Though $\epsilon_{\rm ff}^{\rm mol}$ has been estimated for PHANGS–ALMA before (D. Utomo et al. 2018; J. Sun et al. 2022, 2023; E. Schinnerer & A. K. Leroy 2024), this result represents the most direct evidence for an actual correlation between $\langle\tau_{\rm ff}^{\rm cloud}\rangle$ and $\tau_{\rm dep}^{\rm mol}$ in our data set.
2. We also observe significant anticorrelations between $\tau_{\rm dep}^{\rm mol}$ and $\langle\Sigma_{\rm mol}^{\rm cloud}\rangle$ and between $\tau_{\rm dep}^{\rm mol}$ and $\langle\sigma_{\rm mol}^{\rm cloud}\rangle$ (Figure 6, Table 3). Because $\langle\tau_{\rm ff}^{\rm cloud}\rangle \propto \langle(\Sigma_{\rm mol}^{\rm cloud})^{-0.5}\rangle$ and $\langle\sigma_{\rm mol}^{\rm cloud}\rangle \propto \langle\Sigma_{\rm mol}^{\rm cloud}\rangle^{0.5}$ for clouds with fixed dynamical state (as per Figure 3), correlations with this sense could all be expected from a single underlying dependence of $\tau_{\rm dep}^{\rm mol}$ on gas volume density. As with $\tau_{\rm dep}^{\rm mol}$ and $\langle\tau_{\rm ff}^{\rm cloud}\rangle$, the best-fit slopes that we find show shallower slopes than expected for $\tau_{\rm dep}^{\rm mol} \propto \langle\tau_{\rm ff}^{\rm cloud}\rangle$ and self-gravitating gas. We consider these measurements more empirically robust and the best points for direct comparisons with other observations or simulations.
3. The anticorrelation between $\tau_{\rm dep}^{\rm mol}$ and $\langle\sigma_{\rm mol}^{\rm cloud}\rangle$ (Figure 11, Table 3, Section 3.2, 4.4) appears interesting because the x-axis does not rely on $\alpha_{\rm CO}$ for the measurement of the cloud-scale gas properties and may be less sensitive to resolution than $\langle\Sigma_{\rm mol}^{\rm cloud}\rangle$. This may remove some of the built-in correlation present in other scaling relations. We emphasize that this anticorrelation between $\tau_{\rm dep}^{\rm mol}$ and $\langle\sigma_{\rm mol}^{\rm cloud}\rangle$ will emerge from clouds with relatively uniform dynamical state with fixed $\epsilon_{\rm ff}^{\rm mol}$ regardless of any details related to interstellar turbulence. An important complication is that $\langle\sigma_{\rm mol}^{\rm cloud}\rangle$ may also have a significant impact on $\alpha_{\rm CO}$ (Y.-H. Teng et al. 2024), which also affects $\tau_{\rm dep}^{\rm mol}$.
4. We also observe an anticorrelation between $\tau_{\rm dep}^{\rm mol}$ and $\langle\alpha_{\rm vir}^{\rm cloud}\rangle$, and the latter should capture the balance of kinetic and self-gravitational potential energy for the gas (Figure 7, Table 6). In our measurements, gas that appears less bound by self-gravity forms stars more efficiently, which does not match naive physical expectations. Practically, this reflects that regions with high mean $\langle\alpha_{\rm vir}^{\rm cloud}\rangle$ often occur in the inner parts of galaxies, where a diffuse, bright molecular medium bound partially by stellar gravity appears common. These regions also appear efficient at forming stars. Both results have significant support from previous studies.
5. Our results depend significantly on the adopted treatment of the CO-to-H_2 conversion factor, $\alpha_{\rm CO}$ (Figure 10, Table 4, Section 3.5). Specifically, the inclusion or omission of a term that accounts for enhanced CO emissivity and excitation in the inner, high surface density parts of galaxies has a large effect on our measurements. When such a term is included, the correlations between $\tau_{\rm dep}^{\rm mol}$, $\langle\tau_{\rm ff}^{\rm cloud}\rangle$, $\langle\Sigma_{\rm mol}^{\rm cloud}\rangle$, and $\langle\sigma_{\rm mol}^{\rm cloud}\rangle$ discussed above become apparent. When omitting the term, we measure correlations with almost the opposite sense. Including this term represents our best estimate, as these corrections appear necessary based on extensive observational and theoretical work. Despite this previous good work, precise knowledge of $\alpha_{\rm CO}$ almost certainly remains the main obstacle to progress in this field.
6. Recasting our results to consider $\epsilon_{\rm ff}^{\rm mol}$ as a function of cloud-scale gas properties, we see almost no correlation between $\epsilon_{\rm ff}^{\rm mol}$ and $\langle\Sigma_{\rm mol}^{\rm cloud}\rangle$ or $\epsilon_{\rm ff}^{\rm mol}$ and $\langle\sigma_{\rm mol}^{\rm cloud}\rangle$ (Figure 11, Table 5). Meanwhile, they appear consistent with a nearly fixed $\epsilon_{\rm ff}^{\rm mol}$ over a relatively wide range of $\langle\alpha_{\rm vir}^{\rm cloud}\rangle$, or perhaps even a mild positive correlation between $\epsilon_{\rm ff}^{\rm mol}$ and $\langle\alpha_{\rm vir}^{\rm cloud}\rangle$, in contrast to the theoretically expected

anticorrelation for a turbulent cloud of pure gas. Given that these relations induce correlated axes without adding significant information, we suggest the reader view the measurements comparing $\tau_{\rm dep}^{\rm mol}$ to cloud-scale gas properties as a more empirically grounded point of comparison.

7. We present quantitative measurements for each region that should be easy to compare to simulations or other samples of galaxies with matched methodology (Table 2). We implore the community conducting detailed physical simulations of galaxies to attempt such measurements. Applying these methods to cases with well-understood geometry and prescriptions for star formation and stellar feedback represents an important step that will allow us to chart next directions for the field. Appendix A suggests a simple procedure to construct such comparisons.

These results largely agree with those seen in work on individual galaxies or small samples by A. K. Leroy et al. (2017a), A. Schruba et al. (2019), and M. Querejeta et al. (2023), but employing a much larger sample.

Finally, a general conclusion from our analysis is that the links between cloud-scale gas properties and $\tau_{\rm dep}^{\rm mol}$ fit naturally into the broader picture expected from simple scaling relations and our knowledge of galaxy structure (Figures 9, 14, Appendix B). After accounting for $\alpha_{\rm CO}$ variations, $\tau_{\rm dep}^{\rm mol}$ tends to be shorter in high surface density inner regions of galaxies (A. K. Leroy et al. 2013; Y.-H. Teng et al. 2024; J. Sun et al. 2023). The cloud-scale $\langle\Sigma_{\rm mol}^{\rm cloud}\rangle$ and $\langle\sigma_{\rm mol}^{\rm cloud}\rangle$ and $\langle\alpha_{\rm vir}^{\rm cloud}\rangle$ also all tend to be higher in these regions, with $\langle\Sigma_{\rm mol}^{\rm cloud}\rangle$ and $\langle\sigma_{\rm mol}^{\rm cloud}\rangle$ generally correlating with one another (J. Sun et al. 2018, 2020b; E. Rosolowsky et al. 2021) and the large-scale surface density in the galaxy disk (J. Sun et al. 2020a; J. Sun et al. 2022). We thus observe a set of predictable, self-consistent relationships among $\tau_{\rm dep}^{\rm mol}$, $\langle\Sigma_{\rm mol}^{\rm cloud}\rangle$, $\langle\sigma_{\rm mol}^{\rm cloud}\rangle$, and $\langle\tau_{\rm ff}^{\rm cloud}\rangle$.

Acknowledgments

We thank the anonymous referee for providing a constructive, timely report.

This work was carried out as part of the PHANGS collaboration.

A.K.L., S.S., and R.C. gratefully acknowledge support from NSF AST AWD 2205628, JWST-GO-02107.009-A, and JWST-GO-03707.001-A. A.K.L. also gratefully acknowledges support by a Humboldt Research Award.

J.S. acknowledges support by the National Aeronautics and Space Administration (NASA) through the NASA Hubble Fellowship grant HST-HF2-51544 awarded by the Space Telescope Science Institute (STScI), which is operated by the Association of Universities for Research in Astronomy, Inc., under contract NAS 5-26555.

M.C. gratefully acknowledges funding from the DFG through an Emmy Noether Research Group (grant No CH2137/1-1). COOL Research DAO is a Decentralized Autonomous Organization supporting research in astrophysics aimed at uncovering our cosmic origins.

J.G. gratefully acknowledges funding via STFC grant ST/Y001133/1 and financial support from the Swiss National Science Foundation (grant No. CRSII5_193826).

H.A.P. acknowledges support from the National Science and Technology Council of Taiwan under grant 110-2112-M-032-020-MY3.

S.C.O.G. acknowledges support from the European Research Council via the ERC Synergy Grant "ECOGAL" (project ID 855130) and from the German Excellence Strategy via the Heidelberg Cluster of Excellence (EXC 2181—390900948) "STRUCTURES."

O.A. acknowledges support from the Knut and Alice Wallenberg Foundation, the Swedish Research Council (grant 2019-04659), and the Swedish National Space Agency (SNSA Dnr 2023-00164).

This paper makes use of the following ALMA data, which have been processed as part of the PHANGS–ALMA CO (2–1) survey: ADS/JAO.ALMA#2012.1.00650.S, ADS/JAO.ALMA#2013.1.00803.S, ADS/JAO.ALMA#2013.1.01161.S, ADS/JAO.ALMA#2015.1.00121.S, ADS/JAO.ALMA#2015.1.00782.S, ADS/JAO.ALMA#2015.1.00925.S, ADS/JAO.ALMA#2015.1.00956.S, ADS/JAO.ALMA#2016.1.00386.S, ADS/JAO.ALMA#2017.1.00392.S, ADS/JAO.ALMA#2017.1.00766.S, ADS/JAO.ALMA#2017.1.00886.L, ADS/JAO.ALMA#2018.1.01321.S, ADS/JAO.ALMA#2018.1.01651.S, ADS/JAO.ALMA#2018.A.00062.S, ADS/JAO.ALMA#2019.1.01235.S, ADS/JAO.ALMA#2019.2.00129.S; ALMA is a partnership of ESO (representing its member states), NSF (USA), and NINS (Japan), together with NRC (Canada), NSC and ASIAA (Taiwan), and KASI (Republic of Korea), in cooperation with the Republic of Chile. The Joint ALMA Observatory is operated by ESO, AUI/NRAO, and NAOJ. The National Radio Astronomy Observatory is a facility of the National Science Foundation operated under cooperative agreement by Associated Universities, Inc.

Appendix A
Procedure to Replicate These Measurements for Comparison to Numerical Simulations or Other Observations

We adopt a measurement scheme that can be easily implemented to allow rigorous, "apples to apples" comparison between PHANGS–ALMA and either numerical simulations or observations of other samples of galaxies.

1. When working with CO data, we first apply a local best estimate $\alpha_{\rm CO}$ to convert the data into units of molecular gas mass. In a simulation estimate, the mass in the CO-bright molecular gas phase is likely to enter our analysis. CO-bright emission visible to PHANGS–ALMA at 150 pc would be defined as $>0.6\,{\rm K\,km\,s^{-1}}$, or about $3\times$ the typical rms integrated intensity noise.
2. Next, we convolved the CO or simulated molecular gas data to have a resolution of 150 pc (FWHM). We estimated the surface density, $\Sigma_{\rm mol}$ and line width, $\sigma_{\rm mol}$ along each line of sight. We then applied inclination corrections as in J. Sun et al. (2022) to calculate face-on values of each quantity. In our framework, the line width is the "effective width" line width as defined in J. Sun et al. (2022), and references therein. From $\Sigma_{\rm mol}^{\rm cloud}$, $\sigma_{\rm mol}^{\rm cloud}$, and $R_{\rm pix}$ ($\equiv(\ell^2 H_{\rm mol}/(8\cos i))^{1/3}$ with $H_{\rm mol}=100$ pc and ℓ the resolution, here 150 pc), we calculated $\alpha_{\rm vir}$ and $\tau_{\rm ff}^{\rm mol}$.
3. Then we divided the target region or galaxy into hexagonal apertures with diameter 1.5 kpc. Within each aperture, we calculated the mass-weighted expectation value of $\Sigma_{\rm mol}^{\rm cloud}$, $\sigma_{\rm mol}^{\rm cloud}$, and $\alpha_{\rm vir}^{\rm cloud}$. To do this, we select all of the sight lines in the region and then for quantity X calculated $\langle X\rangle = \sum\Sigma_{\rm mol}^{\rm cloud} X/\sum\Sigma_{\rm mol}^{\rm cloud}$. In the case of $\tau_{\rm ff}^{\rm mol}$, we calculated the average via $\langle\tau_{\rm ff}^{\rm cloud}\rangle = (\sum\Sigma_{\rm mol}(\tau_{\rm ff}^{\rm cloud})^{-1}/\sum\Sigma_{\rm mol})^{-1}$ so that

for a fixed efficiency per freefall time, $\Sigma_{\rm SFR} = \epsilon_{\rm ff}^{\rm mol} \langle \tau_{\rm ff}^{\rm cloud} \rangle \Sigma_{\rm mol}$.

4. We estimated the molecular gas depletion time by convolving the $\Sigma_{\rm SFR}$ and $\Sigma_{\rm mol}$ maps to 1.5 kpc (FWHM) resolution. Next, we divided them to estimate $\tau_{\rm dep}^{\rm mol}$ and sample the map at the center of each region to obtain the local $\tau_{\rm dep}^{\rm mol}$.
5. Then we divided $\langle \tau_{\rm ff}^{\rm cloud} \rangle / \tau_{\rm dep}^{\rm mol}$ to estimate the mean star formation efficiency per freefall time, $\epsilon_{\rm ff}^{\rm mol}$, in the region.
6. Finally, we selected regions with mass-weighted average molecular gas surface density $\langle \Sigma_{\rm mol}^{\rm cloud} \rangle > 20\ M_\odot\ {\rm pc}^{-2}$ to match our completeness cut.

Appendix B
PHANGS–ALMA at Higher Resolution

In the main text, we present results at $\ell = 150$ pc resolution. PHANGS–ALMA also represents the largest survey of CO from galaxies at 120 pc, 90 pc, and 60 pc resolution, though we have fewer galaxies at these higher resolutions. Tables 7, 8, and 9 report results that measure cloud-scale properties at these higher resolutions. We apply the same completeness and surface density cuts, but work with 1 kpc diameter hexagonal regions rather than the 1.5 kpc diameter used for the main results. This is possible because the galaxies with higher physical resolution are also closer, meaning that our $\Sigma_{\rm SFR}$ estimates (which use lower-resolution WISE data) can reach 1 kpc resolution. Given this, our sample at $\ell = 120$ pc consists of 966 1 kpc regions in 41 galaxies. At $\ell = 90$ pc we have 552 regions in 28 galaxies, and at $\ell = 60$ pc we have 170 regions in nine galaxies. Figure 16 shows $\tau_{\rm dep}^{\rm mol}$ as a function of $\langle \Sigma_{\rm mol}^{\rm cloud} \rangle$ and $\langle \sigma_{\rm mol}^{\rm cloud} \rangle$ for each of these resolutions, with our fiducial results overplotted as a black line. Overall, all three resolutions show consistent results, though the number of galaxies' centers with extreme conditions is lower for the smaller samples at higher linear resolution. Because radial variations in gas properties drive our dynamic range (Section 3.4), especially extreme conditions at galaxy centers, the trends are noisier for these high-resolution data sets.

Table 7
Measurements for Individual Regions at $\ell = 120$ pc in 1.0 kpc Diameter Regions

Galaxy	Radius	$\tau_{\rm dep}^{\rm mol}$	$\frac{\tau_{\rm dep}^{\rm mol}}{\langle\tau_{\rm dep}^{\rm mol}\rangle_{\rm gal}}$	$\alpha_{\rm CO}^{2-1}$	i	$\log_{10} M_\star$	$\log_{10}$SFR	$\langle\Sigma_{\rm mol}^{\rm cloud}\rangle$	$\langle\tau_{ff}^{\rm cloud}\rangle$	$\langle\sigma_{\rm mol}^{\rm cloud}\rangle$	$\langle\alpha_{\rm vir}^{\rm cloud}\rangle$	$\epsilon_{\rm ff}^{\rm mol}$	$\frac{\epsilon_{\rm ff}^{\rm mol}}{\langle\epsilon_{\rm ff}^{\rm mol}\rangle_{\rm gal}}$
	(kpc)	(Gyr)	(norm.)	$(\frac{M_\odot\ {\rm pc}^{-2}}{{\rm K\ km\ s}^{-1}})$	(°)	$(M_\odot)$	$(M_\odot\ {\rm yr}^{-1})$	$(M_\odot\ {\rm pc}^{-2})$	(Myr)	(km s^{-1})			(norm.)
IC1954	0.0	0.7	0.51	4.36	57.1	9.7	−0.4	33.0	8.03	6.9	4.11	0.0115	1.66
IC1954	1.22	1.44	1.06	6.57	57.1	9.7	−0.4	26.0	9.08	4.9	2.37	0.0063	0.91
IC1954	1.22	1.27	0.94	6.8	57.1	9.7	−0.4	37.0	7.82	5.3	2.35	0.0062	0.89
IC1954	1.31	1.61	1.18	7.05	57.1	9.7	−0.4	35.0	7.95	5.2	2.41	0.0049	0.71
IC1954	1.31	1.55	1.14	7.1	57.1	9.7	−0.4	30.0	8.69	4.9	2.54	0.0056	0.81
IC1954	1.74	1.97	1.45	8.23	57.1	9.7	−0.4	21.0	10.13	4.1	2.07	0.0051	0.74
IC1954	1.84	1.33	0.98	7.63	57.1	9.7	−0.4	26.0	9.35	4.6	2.63	0.0071	1.02
IC1954	2.95	1.23	0.91	9.53	57.1	9.7	−0.4	23.0	9.61	4.4	2.08	0.0078	1.13
IC5273	0.0	0.38	0.51	3.87	52.0	9.7	−0.3	62.0	6.66	7.6	4.0	0.0177	1.1

Note. This is a stub. The full table is available as part of a machine-readable table. Columns: (1) galaxy name, (2) galactocentric radius, (3) molecular gas depletion time, (4) molecular gas depletion time normalized to galaxy average, (5) CO (2–1) to H_2 conversion factor, (6) galaxy inclination, (7) galaxy integrated stellar mass, (8) galaxy integrated star formation rate, region-averaged mass-weighted molecular gas: (9) surface density, (10) gravitational freefall time, (11) line width, and (12) virial parameter, (13) star formation efficiency per freefall time, and (14) star formation efficiency per freefall time normalized to galaxy average.

(This table is available in its entirety in machine-readable form in the online article.)

Table 8
Measurements for Individual Regions at $\ell = 90$ pc in 1.0 kpc Diameter Regions

Galaxy	Radius	$\tau_{\rm dep}^{\rm mol}$	$\frac{\tau_{\rm dep}^{\rm mol}}{\langle\tau_{\rm dep}^{\rm mol}\rangle_{\rm gal}}$	$\alpha_{\rm CO}^{2-1}$	i	$\log_{10} M_\star$	$\log_{10}$SFR	$\langle\Sigma_{\rm mol}^{\rm cloud}\rangle$	$\langle\tau_{ff}^{\rm cloud}\rangle$	$\langle\sigma_{\rm mol}^{\rm cloud}\rangle$	$\langle\alpha_{\rm vir}^{\rm cloud}\rangle$	$\epsilon_{\rm ff}^{\rm mol}$	$\frac{\epsilon_{\rm ff}^{\rm mol}}{\langle\epsilon_{\rm ff}^{\rm mol}\rangle_{\rm gal}}$
	(kpc)	(Gyr)	(norm.)	$(\frac{M_\odot\ {\rm pc}^{-2}}{{\rm K\ km\ s}^{-1}})$	(°)	$(M_\odot)$	$(M_\odot\ {\rm yr}^{-1})$	$(M_\odot\ {\rm pc}^{-2})$	(Myr)	(km s^{-1})			(norm.)
IC1954	0.0	0.7	0.51	4.36	57.1	9.7	−0.4	35.0	7.04	6.2	3.82	0.0101	1.66
IC1954	1.22	1.44	1.06	6.57	57.1	9.7	−0.4	28.0	7.94	4.5	2.3	0.0055	0.91
IC1954	1.22	1.27	0.94	6.8	57.1	9.7	−0.4	38.0	6.92	5.0	2.31	0.0054	0.9
IC1954	1.31	1.61	1.18	7.05	57.1	9.7	−0.4	37.0	7.02	4.9	2.37	0.0044	0.72
IC1954	1.31	1.55	1.14	7.1	57.1	9.7	−0.4	31.0	7.66	4.6	2.39	0.005	0.82
IC1954	1.74	1.97	1.45	8.23	57.1	9.7	−0.4	22.0	8.97	3.7	1.99	0.0046	0.75
IC1954	1.84	1.33	0.98	7.63	57.1	9.7	−0.4	30.0	7.94	4.2	2.4	0.006	0.99
IC1954	2.95	1.23	0.91	9.53	57.1	9.7	−0.4	25.0	8.41	4.0	1.94	0.0068	1.13
NGC0628	0.0	1.53	0.56	2.63	8.9	10.3	0.2	22.0	11.62	4.6	6.65	0.0076	1.82

Note. This is a stub. The full table is available as part of a machine-readable table. Columns: (1) galaxy name, (2) galactocentric radius, (3) molecular gas depletion time, (4) molecular gas depletion time normalized to galaxy average, (5) CO (2–1) to H_2 conversion factor, (6) galaxy inclination, (7) galaxy integrated stellar mass, (8) galaxy integrated star formation rate, region-averaged mass-weighted molecular gas: (9) surface density, (10) gravitational freefall time, (11) line width, and (12) virial parameter, (13) star formation efficiency per freefall time, and (14) star formation efficiency per freefall time normalized to galaxy average.

(This table is available in its entirety in machine-readable form in the online article.)

Table 9
Measurements for Individual Regions at $\ell = 60$ pc in 1.0 kpc Diameter Regions

Galaxy	Radius	$\tau_{\rm dep}^{\rm mol}$	$\frac{\tau_{\rm dep}^{\rm mol}}{\langle\tau_{\rm dep}^{\rm mol}\rangle_{\rm gal}}$	$\alpha_{\rm CO}^{2-1}$	i	$\log_{10} M_\star$	$\log_{10}$SFR	$\langle\Sigma_{\rm mol}^{\rm cloud}\rangle$	$\langle\tau_{ff}^{\rm cloud}\rangle$	$\langle\sigma_{\rm mol}^{\rm cloud}\rangle$	$\langle\alpha_{vir}^{\rm cloud}\rangle$	$\epsilon_{\rm ff}^{\rm mol}$	$\frac{\epsilon_{\rm ff}^{\rm mol}}{\langle\epsilon_{\rm ff}^{\rm mol}\rangle_{\rm gal}}$
	(kpc)	(Gyr)	(norm.)	$(\frac{M_\odot\ {\rm pc}^{-2}}{{\rm K\ km\ s}^{-1}})$	(°)	$(M_\odot)$	$(M_\odot\ {\rm yr}^{-1})$	$(M_\odot\ {\rm pc}^{-2})$	(Myr)	(km s^{-1})			(norm.)
NGC0628	0.0	1.53	0.55	2.63	8.9	10.3	0.2	24.0	9.07	4.2	7.21	0.0059	1.95
NGC0628	1.0	2.79	1.0	3.61	8.9	10.3	0.2	28.0	8.5	3.8	4.68	0.0031	1.0
NGC0628	1.0	2.09	0.75	3.51	8.9	10.3	0.2	24.0	8.98	4.0	5.7	0.0043	1.41
NGC0628	1.01	2.18	0.78	3.51	8.9	10.3	0.2	35.0	7.75	4.6	5.55	0.0036	1.17
NGC0628	1.01	2.31	0.83	3.61	8.9	10.3	0.2	27.0	8.66	4.3	5.26	0.0038	1.23
NGC0628	1.01	2.95	1.06	3.71	8.9	10.3	0.2	21.0	9.94	3.5	5.02	0.0034	1.11
NGC0628	1.01	2.24	0.8	3.72	8.9	10.3	0.2	30.0	8.48	4.4	5.19	0.0038	1.24
NGC0628	1.74	2.67	0.96	4.64	8.9	10.3	0.2	20.0	10.02	3.3	3.77	0.0038	1.23
NGC0628	1.74	2.47	0.88	4.67	8.9	10.3	0.2	22.0	9.47	3.2	4.28	0.0038	1.26

Note. This is a stub. The full table is available as part of a machine-readable table. Columns: (1) galaxy name, (2) galactocentric radius, (3) molecular gas depletion time, (4) molecular gas depletion time normalized to galaxy average, (5) CO (2–1) to H_2 conversion factor, (6) galaxy inclination, (7) galaxy integrated stellar mass, (8) galaxy integrated star formation rate, region-averaged mass-weighted molecular gas: (9) surface density, (10) gravitational freefall time, (11) line width, and (12) virial parameter, (13) star formation efficiency per freefall time, and (14) star formation efficiency per freefall time normalized to galaxy average.

(This table is available in its entirety in machine-readable form in the online article.)

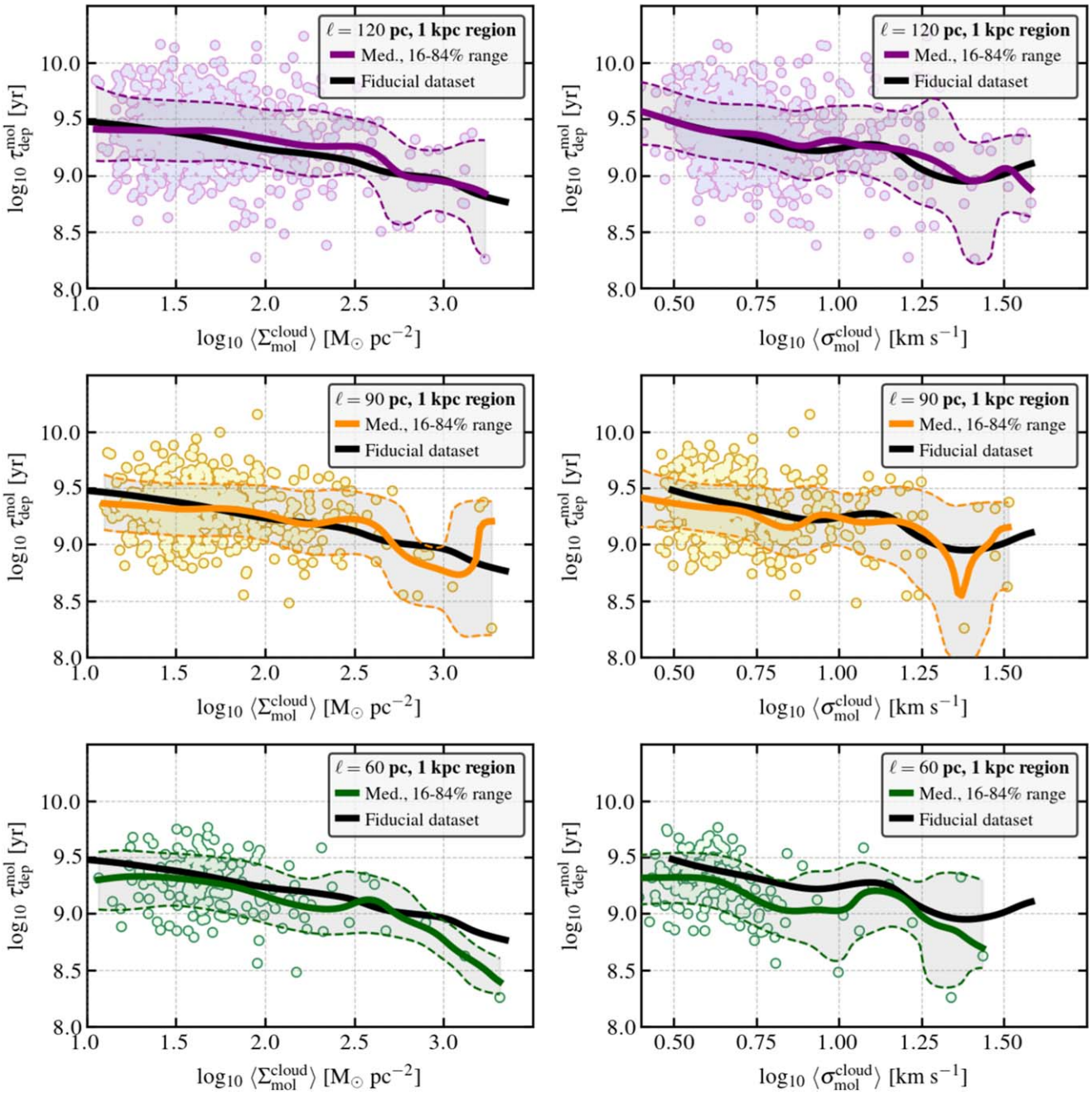

Figure 16. Molecular gas depletion time as a function of cloud-scale mean (left panel) surface density and (right panel) line width measured for sharper cloud-scale resolutions than the $\ell = 150$ pc used in the main text, top to bottom $\ell = 120$ pc, $\ell = 90$, $\ell = 60$ pc. We show the running median and 16th–84th percentile range for each quantity in each panel and plot the median trend for the data set used in the main paper ($\ell = 150$ pc over 1.5 kpc regions) in black. The sample of galaxies that reach a given resolution varies, but overall the same trends are evident at all four resolutions. We provide these higher-resolution, lower sample-size data sets as additional data products.

ORCID iDs

Adam K. Leroy https://orcid.org/0000-0002-2545-1700
Jiayi Sun (孙嘉懿) https://orcid.org/0000-0003-0378-4667
Sharon Meidt https://orcid.org/0000-0002-6118-4048
Oscar Agertz https://orcid.org/0000-0002-4287-1088
I-Da Chiang (江宜達) https://orcid.org/0000-0003-2551-7148
Jindra Gensior https://orcid.org/0000-0001-6119-9883
Simon C. O. Glover https://orcid.org/0000-0001-6708-1317
Oleg Y. Gnedin https://orcid.org/0000-0001-9852-9954
Annie Hughes https://orcid.org/0000-0002-9181-1161
Eva Schinnerer https://orcid.org/0000-0002-3933-7677
Ashley T. Barnes https://orcid.org/0000-0003-0410-4504
Frank Bigiel https://orcid.org/0000-0003-0166-9745
Alberto D. Bolatto https://orcid.org/0000-0002-5480-5686
Dario Colombo https://orcid.org/0000-0001-6498-2945
Jakob den Brok https://orcid.org/0000-0002-8760-6157
Mélanie Chevance https://orcid.org/0000-0002-5635-5180
Ryan Chown https://orcid.org/0000-0001-8241-7704
Cosima Eibensteiner https://orcid.org/0000-0002-1185-2810
Damian R. Gleis https://orcid.org/0009-0001-8660-9962
Kathryn Grasha https://orcid.org/0000-0002-3247-5321
Jonathan D. Henshaw https://orcid.org/0000-0001-9656-7682
Ralf S. Klessen https://orcid.org/0000-0002-0560-3172

Eric W. Koch https://orcid.org/0000-0001-9605-780X
Elias K. Oakes https://orcid.org/0000-0002-0119-1115
Hsi-An Pan https://orcid.org/0000-0002-1370-6964
Miguel Querejeta https://orcid.org/0000-0002-0472-1011
Erik Rosolowsky https://orcid.org/0000-0002-5204-2259
Karin Sandstrom https://orcid.org/0000-0002-4378-8534
Sumit K. Sarbadhicary https://orcid.org/0000-0002-4781-7291
Yu-Hsuan Teng https://orcid.org/0000-0003-4209-1599
Antonio Usero https://orcid.org/0000-0003-1242-505X
Thomas G. Williams https://orcid.org/0000-0002-0012-2142

References

Accurso, G., Saintonge, A., Catinella, B., et al. 2017, MNRAS, 470, 4750
Agertz, O., Renaud, F., Feltzing, S., et al. 2021, MNRAS, 503, 5826
Anand, G. S., Lee, J. C., Van Dyk, S. D., et al. 2021, MNRAS, 501, 3621
Ballesteros-Paredes, J. 2006, MNRAS, 372, 443
Belfiore, F., Leroy, A. K., Sun, J., et al. 2023, A&A, 670, A67
Belfiore, F., Maiolino, R., Bundy, K., et al. 2018, MNRAS, 477, 3014
Bertoldi, F., & McKee, C. F. 1992, ApJ, 395, 140
Bigiel, F., Leroy, A., Walter, F., et al. 2008, AJ, 136, 2846
Blitz, L., Fukui, Y., Kawamura, A., et al. 2007, in Protostars and Planets V, ed. B. Reipurth, D. Jewitt, & K. Keil (Tucson, AZ: Univ. Arizona Press), 81
Blitz, L., & Rosolowsky, E. 2006, ApJ, 650, 933
Bolatto, A. D., Wolfire, M., & Leroy, A. K. 2013, ARA&A, 51, 207
Brunetti, N., Wilson, C. D., He, H., et al. 2024, MNRAS, 530, 597
Brunetti, N., Wilson, C. D., Sliwa, K., et al. 2021, MNRAS, 500, 4730
Burkhart, B. 2018, ApJ, 863, 118
Chevance, M., Kruijssen, J. M. D., Hygate, A. P. S., et al. 2020, MNRAS, 493, 2872
Chiang, I.-D., Sandstrom, K. M., Chastenet, J., et al. 2024, ApJ, 964, 18
Davis, T. A., Gensior, J., Bureau, M., et al. 2022, MNRAS, 512, 1522
Davis, T. A., Young, L. M., Crocker, A. F., et al. 2014, MNRAS, 444, 3427
den Brok, J., Jiménez-Donaire, M. J., Leroy, A., et al. 2025, AJ, 169, 18
den Brok, J. S., Bigiel, F., Chastenet, J., et al. 2023, A&A, 676, A93
den Brok, J. S., Chatzigiannakis, D., Bigiel, F., et al. 2021, MNRAS, 504, 3221
Dobbs, C. L., Rosolowsky, E., Pettitt, A. R., et al. 2019, MNRAS, 485, 4997
Eibensteiner, C., Sun, J., Bigiel, F., et al. 2024, A&A, 691, A163
Ellison, S. L., Sánchez, S. F., Ibarra-Medel, H., et al. 2018, MNRAS, 474, 2039
Evans, N. J. I., Heiderman, A., & Vutisalchavakul, N. 2014, ApJ, 782, 114
Evans, N. J., Jeong-Gyu, K., & Ostriker, E. C. 2022, ApJL, 929, L18
Federrath, C., & Klessen, R. S. 2012, ApJ, 761, 156
Federrath, C., & Klessen, R. S. 2013, ApJ, 763, 51
Field, G. B., Blackman, E. G., & Keto, E. R. 2011, MNRAS, 416, 710
Fukui, Y., Habe, A., Inoue, T., Enokiya, R., & Tachihara, K. 2021, PASJ, 73, S1
Fukui, Y., & Kawamura, A. 2010, ARA&A, 48, 547
Gallagher, M. J., Leroy, A. K., Bigiel, F., et al. 2018, ApJL, 868, L38
Gao, Y., & Solomon, P. M. 2004, ApJ, 606, 271
Garcìa-Burillo, S., Usero, A., Alonso-Herrero, A., et al. 2012, A&A, 539, A8
Garcìa-Rodrìguez, A., Usero, A., Leroy, A. K., et al. 2023, A&A, 672, A96
Gong, M., Ostriker, E. C., Kim, C.-G., & Kim, J.-G. 2020, ApJ, 903, 142
Grisdale, K., Agertz, O., Renaud, F., & Romeo, A. B. 2018, MNRAS, 479, 3167
Grisdale, K., Agertz, O., Renaud, F., et al. 2019, MNRAS, 486, 5482
Henshaw, J. D., Barnes, A. T., Battersby, C., et al. 2023, in ASP Conf. Ser. 534, Protostars and Planets VII, ed. S. Inutsuka et al. (San Francisco, CA: ASP), 83
Henshaw, J. D., Kruijssen, J. M. D., Longmore, S. N., et al. 2020, NatAs, 4, 1064
Henshaw, J. D., Longmore, S. N., Kruijssen, J. M. D., et al. 2016, MNRAS, 457, 2675
Heyer, M., & Dame, T. M. 2015, ARA&A, 53, 583
Heyer, M., Krawczyk, C., Duval, J., & Jackson, J. M. 2009, ApJ, 699, 1092
Heyer, M. H., Carpenter, J. M., & Snell, R. L. 2001, ApJ, 551, 852
Hirota, A., Egusa, F., Baba, J., et al. 2018, PASJ, 70, 73
Hopkins, P. F., Quataert, E., & Murray, N. 2011, MNRAS, 417, 950
Hu, C.-Y., Schruba, A., Sternberg, A., & van Dishoeck, E. F. 2022, ApJ, 931, 28
Hughes, A., Meidt, S. E., Colombo, D., et al. 2013, ApJ, 779, 46
Ibáñez-Mejìa, J. C., Mac Low, M.-M., Klessen, R. S., & Baczynski, C. 2016, ApJ, 824, 41
Israel, F. P. 2020, A&A, 635, A131
Jeffreson, S. M. R., Semenov, V. A., & Krumholz, M. R. 2024, MNRAS, 527, 7093
Jeffreson, S. M. R., Sun, J., & Wilson, C. D. 2022, MNRAS, 515, 1663
Jiménez-Donaire, M. J., Bigiel, F., Leroy, A. K., et al. 2019, ApJ, 880, 127
Jiménez-Donaire, M. J., Usero, A., Bešlić, I., et al. 2023, A&A, 676, L11
Jogee, S., Scoville, N., & Kenney, J. D. P. 2005, ApJ, 630, 837
Kainulainen, J., Beuther, H., Henning, T., & Plume, R. 2009, A&A, 508, L35
Katz, N. 1992, ApJ, 391, 502
Keenan, R. P., Marrone, D. P., & Keating, G. K. 2025, ApJ, 979, 228
Kennicutt, R. C., & Evans, N. J. 2012, ARA&A, 50, 531
Kim, C.-G., Kim, J.-G., Gong, M., & Ostriker, E. C. 2023, ApJ, 946, 3
Kim, J., Chevance, M., Kruijssen, J. M. D., et al. 2022, MNRAS, 516, 3006
Kim, J.-G., Ostriker, E. C., & Filippova, N. 2021, ApJ, 911, 128
Kim, J.-h., Abel, T., Agertz, O., et al. 2014, ApJS, 210, 14
Koch, E., Rosolowsky, E., & Leroy, A. K. 2018, RNAAS, 2, 220
Koda, J. 2021, RNAAS, 5, 222
Kormendy, J., & Kennicutt, R. C. J. 2004, ARA&A, 42, 603
Kruijssen, J. M. D., Schruba, A., Chevance, M., et al. 2019, Natur, 569, 519
Krumholz, M. R. 2014, PhR, 539, 49
Krumholz, M. R., & McKee, C. F. 2005, ApJ, 630, 250
Krumholz, M. R., & Thompson, T. A. 2007, ApJ, 669, 289
Kuno, N., Sato, N., Nakanishi, H., et al. 2007, PASJ, 59, 117
Lada, C. J., Forbrich, J., Lombardi, M., & Alves, J. F. 2012, ApJ, 745, 190
Lada, C. J., Lombardi, M., & Alves, J. F. 2010, ApJ, 724, 687
Lang, P., Meidt, S. E., Rosolowsky, E., et al. 2020, ApJ, 897, 122
Leroy, A. K., Hughes, A., Schruba, A., et al. 2016, ApJ, 831, 16
Leroy, A. K., Sandstrom, K. M., Lang, D., et al. 2019, ApJS, 244, 24
Leroy, A. K., Schinnerer, E., Hughes, A., et al. 2017a, ApJ, 846, 71
Leroy, A. K., Schinnerer, E., Hughes, A., et al. 2021, ApJS, 257, 43
Leroy, A. K., Rosolowsky, E., Usero, A., et al. 2022, ApJ, 927, 149
Leroy, A. K., Usero, A., Schruba, A., et al. 2017b, ApJ, 835, 217
Leroy, A. K., Walter, F., Brinks, E., et al. 2008, AJ, 136, 2782
Leroy, A. K., Walter, F., Bigiel, F., et al. 2009, AJ, 137, 4670
Leroy, A. K., Walter, F., Sandstrom, K., et al. 2013, AJ, 146, 19
Liu, L., Bureau, M., Blitz, L., et al. 2021, MNRAS, 505, 4048
Lin, L., Ellison, S. L., Pan, H.-A., et al. 2022, ApJ, 926, 175
Lu, A., Haggard, D., Bureau, M., et al. 2024, MNRAS, 531, 3888
Mac Low, M.-M., & Klessen, R. S. 2004, RvMP, 76, 125
Maiolino, R., & Mannucci, F. 2019, A&ARv, 27, 3
Martin, D. C., Fanson, J., Schiminovich, D., et al. 2005, ApJL, 619, L1
McKee, C. F., & Ostriker, E. C. 2007, ARA&A, 45, 565
McKee, C. F., & Zweibel, E. G. 1992, ApJ, 399, 551
Meidt, S. E., Hughes, A., Dobbs, C. L., et al. 2015, ApJ, 806, 72
Meidt, S. E., Leroy, A. K., Rosolowsky, E., et al. 2018, ApJ, 854, 100
Meidt, S. E., Schinnerer, E., Garcìa-Burillo, S., et al. 2013, ApJ, 779, 45
Muraoka, K., Sorai, K., Miyamoto, Y., et al. 2019, PASJ, 71, S15
Neumann, L., Gallagher, M. J., Bigiel, F., et al. 2023, MNRAS, 521, 3348
Padoan, P., Haugbølle, T., & Nordlund, Å. 2012, ApJL, 759, L27
Padoan, P., & Nordlund, Å. 2002, ApJ, 576, 870
Padoan, P., & Nordlund, Å. 2011, ApJ, 730, 40
Pan, H.-A., Lin, L., Ellison, S. L., et al. 2024, ApJ, 964, 120
Pan, H.-A., Schinnerer, E., Hughes, A., et al. 2022, ApJ, 927, 9
Pathak, D., Leroy, A. K., Thompson, T. A., et al. 2024, AJ, 167, 39
Querejeta, M., Leroy, A. K., Meidt, S. E., et al. 2024, A&A, 687, A293
Querejeta, M., Pety, J., Schruba, A., et al. 2023, A&A, 680, A4
Querejeta, M., Schinnerer, E., Meidt, S., et al. 2021, A&A, 656, A133
Regan, M. W., Thornley, M. D., Helfer, T. T., et al. 2001, ApJ, 561, 218
Renaud, F., Romeo, A. B., & Agertz, O. 2021, MNRAS, 508, 352
Rosolowsky, E., Hughes, A., Leroy, A. K., et al. 2021, MNRAS, 502, 1218
Saintonge, A., & Catinella, B. 2022, ARA&A, 60, 319
Saintonge, A., Catinella, B., Tacconi, L. J., et al. 2017, ApJS, 233, 22
Saintonge, A., Kauffmann, G., Wang, J., et al. 2011, MNRAS, 415, 61
Salim, S., Lee, J. C., Janowiecki, S., et al. 2016, ApJS, 227, 2
Sandstrom, K. M., Leroy, A. K., Walter, F., et al. 2013, ApJ, 777, 5
Schinnerer, E., Hughes, A., Leroy, A., et al. 2019, ApJ, 887, 49
Schinnerer, E., & Leroy, A. K. 2024, ARA&A, 62, 369
Schruba, A., Kruijssen, J. M. D., & Leroy, A. K. 2019, ApJ, 883, 2
Schruba, A., Leroy, A. K., Walter, F., Sandstrom, K., & Rosolowsky, E. 2010, ApJ, 722, 1699
Schruba, A., Leroy, A. K., Walter, F., et al. 2011, AJ, 142, 37
Schruba, A., Leroy, A. K., Walter, F., et al. 2012, AJ, 143, 138
Segovia Otero, Á., Agertz, O., Renaud, F., et al. 2025, MNRAS, 538, 2646
Semenov, V. A., Kravtsov, A. V., & Gnedin, N. Y. 2017, ApJ, 845, 133
Semenov, V. A., Kravtsov, A. V., & Gnedin, N. Y. 2018, ApJ, 861, 4
Semenov, V. A., Kravtsov, A. V., & Gnedin, N. Y. 2021, ApJ, 918, 13
Sheth, K., Regan, M., Hinz, J. L., et al. 2010, PASP, 122, 1397

Stuber, S. K., Pety, J., Schinnerer, E., et al. 2023, A&A, 680, L20
Sun, J., Leroy, A. K., Ostriker, E. C., et al. 2020a, ApJ, 892, 148
Sun, J., Leroy, A. K., Ostriker, E. C., et al. 2023, ApJL, 945, L19
Sun, J., Leroy, A. K., Rosolowsky, E., et al. 2022, AJ, 164, 43
Sun, J., Leroy, A. K., Schruba, A., et al. 2018, ApJ, 860, 172
Sun, J., Leroy, A. K., Schinnerer, E., et al. 2020b, ApJL, 901, L8
Tacconi, L. J., Genzel, R., & Sternberg, A. 2020, ARA&A, 58, 157
Tafalla, M., Usero, A., & Hacar, A. 2023, A&A, 679, A112
Teng, Y.-H., Chiang, I.-D., Sandstrom, K. M., et al. 2024, ApJ, 961, 42
Teng, Y.-H., Sandstrom, K. M., Sun, J., et al. 2022, ApJ, 925, 72
Teng, Y.-H., Sandstrom, K. M., Sun, J., et al. 2023, ApJ, 950, 119
Utomo, D., Sun, J., Leroy, A. K., et al. 2018, ApJL, 861, L18
Vazquez-Semadeni, E. 1994, ApJ, 423, 681
Vázquez-Semadeni, E., Palau, A., Gómez, G. C., et al. 2024, arXiv:2408.10406
Williams, T. G., Bureau, M., Davis, T. A., et al. 2023, MNRAS, 525, 4270
Wong, T., & Blitz, L. 2002, ApJ, 569, 157
Wright, E. L., Eisenhardt, P. R. M., Mainzer, A. K., et al. 2010, AJ, 140, 1868
Yajima, Y., Sorai, K., Miyamoto, Y., et al. 2021, PASJ, 73, 257
Young, J. S., & Scoville, N. Z. 1991, ARA&A, 29, 581
Young, J. S., Xie, S., Tacconi, L., et al. 1995, ApJS, 98, 219